Investigation of the strain induced rafting of the gamma prime precipitates in single crystal nickel based superalloys.

Nicolas Ratel-Ramond

UNIVERSITÉ JOSEPH FOURIER

LABORATOIRE DE SPECTROMÉTRIE PHYSIQUE

THÈSE

PRÉSENTÉE PAR

Nicolas RATEL

POUR OBTENIR LE TITRE DE DOCTEUR
DE L'UNIVERSITÉ JOSEPH FOURIER – GRENOBLE I

SPECIALITÉ : **PHYSIQUE POUR L'INSTRUMENTATION**

ÉTUDE DE LA MISE EN RADEAUX DES PRÉCIPITÉS γ' PLASTIQUEMENT INDUITE DANS LES SUPERALLIAGES MONOCRISTALLINS À BASE DE NICKEL

INVESTIGATION OF THE STRAIN INDUCED RAFTING OF γ' PARTICLES IN SINGLE CRYSTALS NICKEL BASED SUPERALLOYS

Thèse dirigée par Pierre BASTIE / Bruno DEMÉ / Giovanni BRUNO

SOUTENUE LE 4 octobre 2007

DEVANT LA COMMISSION D'EXAMEN:

Pr. Y. Bréchet	**Président du jury**
Pr. H.A. Calderon	**Rapporteur**
Dr. A. Jacques	**Rapporteur**
Pr. T. Mori	**Examinateur**
J. Y. Guédou	**Examinateur**

Remerciements

Ces travaux de thèse ont été réalisés à l'Institut Laue Langevin au sein du groupe Large Scale Structures dirigé par Mr. Peter Timmins et en collaboration avec le Laboratoire de Spectrométrie Physique dirigé par Mr. Thierry Dombre. Je tiens à remercier ces deux personnes ainsi que Mr. Christian Vettier, directeur scientifique de l'ILL pour leur accueil au sein de leur laboratoire.

La supervision des travaux présentés dans ce mémoire a été prise en charge par Pierre Bastie du Laboratoire de Spectrométrie Physique, Giovanni Bruno et Bruno Demé de l'Institut Laue Langevin. Leurs précieux conseils, ainsi que les nombreuses discussions scientifiques et le partage de leur savoir faire ont été un apport inestimable pour la réalisation de cette thèse. Je tiens donc à leur exprimer toute ma reconnaissance et mes plus sincères remerciements pour le temps passé à encadrer ces travaux. Je remercie aussi vivement Mr. Jean-Yves Guédou, directeur scientifique de la SNECMA pour la fourniture des barreaux de superalliage utilisés pour la réalisation des expériences ainsi que pour son intérêt dans mes travaux.

Je remercie également messieurs Alain Jacques du Laboratoire de Physique des Matériaux de Nancy et Hector Calderon de l'Instituto Politecnico Nacional de Mexico pour avoir accepté de rapporter sur ce manuscrit de thèse. La pertinence de leurs remarques a sans nul doute fortement contribué à donner à ce manuscrit toute sa substance. Je tiens aussi à remercier les professeurs Yves Bréchet (SIMAP-Grenoble) et Tsutomu Mori (Manchester Materials Science Centre-Manchester) pour avoir accepté de participer au jury de cette thèse. Qu'ils trouvent ici l'expression de mes sincères remerciements.

Je tiens également à remercier sincèrement Pierre Caron de l'ONERA pour l'intérêt qu'il a montré sur ces travaux et les discussions scientifiques qui en ont découlé, ainsi que pour sa précieuse assistance lors de la déformation des échantillons de superalliage à haute température.

Une grosse partie des expériences présentées dans ce recueil n'aurait pas été réalisable sans la précieuse assistance de Paul Martin et Steffen Demas du labo four de l'ILL. Que ce soit pour la préparation des fours, la réparation à distance de pannes diverses ou pour la préparation d'échantillons, la disponibilité et le sérieux de cette équipe ont rendu le travail plus simple et plus agréable. De façon similaire, certaines expériences ont été réalisées avec un dispositif thermomécanique développé par le Laboratoire de Physique des Matériaux de l'Ecole des Mines de Nancy. Je tiens particulièrement à remercier Olivier Ferry, Thomas Schenk, Alain Jacques et Philippe Masschelein pour leur aide et leur soutien au cours de ces expériences, et aussi pour la préparation d'échantillons. Je salue aussi au passage Sylvie Migot et Alain Jacques pour leur soutien et leur assistance au cours des quinze jours passés à Nancy pour y faire les observations de microscopie électronique en transmission présentées dans cet ouvrage.

Certaines expériences réalisées sur de grands instruments ont été conduites à l'étranger. Je tiens à remercier Marie-Hélène Mathon et Alain Lapp du Laboratoire Léon Brillouin à Paris, Uwe Keiderling du Hahn Meitner Institut à Berlin, Martin Von Zimmermann, Uta Rut ainsi que Andreas Schoeps du Hasylab à Hambourg et Pavel Strunz du Nuclear Physics Institute à Prague, pour leurs précieux conseils, leur patience et leur disponibilité diurne et nocturne afin que les expériences soient réalisées dans les meilleures conditions.

Toute une partie des travaux présentés dans cet ouvrage n'aurait certainement pas été réalisable sans la patience et l'enseignement du professeur T. Mori, que je tiens à remercier chaleureusement pour l'intérêt qu'il a montré à cette étude et pour les nombreuses discussions scientifiques (ou non) qu'on a pu avoir ensemble au cours de nombreux dîners. Le partage de son savoir a sans aucun doute fortement contribué à la réalisation des travaux ici présentés. Je tiens aussi à remercier toute l'équipe de FaME38 : Darren Hughes, Benoît Malard, Peter Webster, Axel Steuwer, Mathew Peel, Neil James et Jens Altenkirch pour leurs commentaires constructifs suite à des présentations orales.

Finalement, je tiens à saluer tous mes amis, sans qui ces trois années n'auraient pas été si agréables : Jérôme, Edouard (quand tu veux dans les airs !),

Elodie, Fabien, Maud, Nadège, Benoît (compagnon de galère), Nicolas, Alain, Steffen, Gary, Mathew, Alex, Andrew, Quentin, Pierrot, sans oublier les amis musiciens : Simon, Christophe, Jacques, Antoine, Claude, Andrew, Lionel, Ludovic, Titi, Francis et tout le big band…

Enfin, je remercie sincèrement mes parents ainsi que mes frères et soeurs pour m'avoir encouragé et soutenu pendant toutes ces années. Toutes mes pensées se dirigent aussi vers celle qui m'accompagne au quotidien et qui m'a aidé pendant les derniers instants de ces travaux : Marlène.

Introduction

Les alliages de nickel monocristallins sont couramment utilisés dans la manufacture de composants aéronautiques pour leur excellente tenue mécanique à haute température. Ces propriétés proviennent de la coexistence de deux phases. La matrice γ est une solution solide désordonnée de structure cfc, dans laquelle précipite de façon cohérente une phase γ' ayant une structure chimiquement ordonnée de type $L1_2$. En plus du durcissement de solution solide dans la matrice γ, les précipités vont avoir un effet de durcissement structural au cours d'un essai mécanique. Les propriétés mécaniques de ces matériaux dépendent donc fortement de la morphologie des précipités γ' et donc de la microstructure de l'alliage. Récemment, l'ajout d'éléments réfractaires lourds, tels le rhénium et le ruthénium, dans la composition du superalliage MC-NG a conduit à une hausse de leurs propriétés mécaniques à très haute température par rapport à des alliages de première génération (AM1). Ceci se traduit par une tenue en fluage à très haute température plus longue (1100°C-100MPa), malgré un stade secondaire de fluage relativement court. L'objectif de cette étude est de déterminer la corrélation existant entre la déformation plastique et l'évolution microstructurale pouvant intervenir au cours d'un test de fluage, afin d'expliquer les différences de comportement expliquées. L'influence de la composition de l'alliage sur l'évolution de la microstructure sera aussi discutée.

I. Les superalliages monocristallins à base de nickel

D'un point de vue microstructural, la morphologie des précipités γ' dépend fortement de l'histoire thermomécanique de l'alliage. Après traitement thermique standard, la microstructure de l'alliage consiste en un arrangement quasi-périodique le long des directions <100> du monocristal de précipités γ' de forme cuboïdale dont les faces sont dans les plans de type <100> et dont les arêtes mesurent environ 350nm. Au cours de ce traitement thermique, il y a compétition entre l'énergie de surface liée à la tension de ligne aux interfaces γ/γ' qui contrôle la croissance des précipités et l'énergie élastique liée à l'anisotropie mécanique de ces matériaux qui contrôle la forme des précipités. Les précipités germent sous forme de particules sphériques cohérentes avec la matrice puis grossissent jusqu'à ce que l'énergie

élastique devienne dominante. Les particules γ' adoptent alors une forme cuboïdale et sont alignées de façon périodique le long des directions <100> du monocristal.

De par la structure cristallographique ordonnée $L1_2$ de la phase γ', le cisaillement des précipités γ' par des dislocations parfaites de matrice n'est pas un processus énergétiquement favorable, puisqu'il conduirait à la formation d'une paroi d'antiphase qui augmenterait de façon notable l'énergie totale du système. Dans ce cas, le processus de déformation dominant est la propagation de dislocations au sein de la matrice, accompagné d'un contournement des particules durcissantes de type Orowan.

Par ailleurs, il existe un désaccord de paramètre de maille entre les phases γ et γ', qui va exercer un champ de contraintes de cohérence sur les dislocations crées lors d'un test mécanique. Dans le cas d'un désaccord paramétrique négatif et d'une contrainte appliquée de traction, la propagation des dislocations sera ainsi favorisée dans les canaux de matrice γ perpendiculaires à l'axe de traction.

Au cours d'un essai de fluage à haute température (ex : 1050ºC), on peut distinguer trois stades, précédés ou non d'une période d'incubation, correspondant au développement de la plasticité dans la matrice. Au cours du stade de fluage primaire, les précipités γ' coalescent de façon orientée, aboutissant à la formation d'une structure lamellaire γ/γ'. Ce phénomène est appelé la mise en radeaux. La direction et la forme des précipités dépend alors, parmi d'autres paramètres, des signes du désaccord paramétrique entre les phases γ et γ' et de la contrainte appliquée. Le stade de fluage secondaire correspond à un taux de déformation stationnaire, au cours duquel la densité de dislocations mobiles est constante. Les interfaces γ/γ' se couvrent d'un réseau de dislocations se densifiant au cours du fluage. La hausse des contraintes d'interfaces associée aboutit au cisaillement des particules γ' et à un taux de déformation accéléré jusqu'à rupture. C'est le stade de fluage tertiaire. Par rapport à l'AM1, le MC-NG présente une période d'incubation, qui précède le stade primaire. Son stade secondaire est aussi relativement plus court. La période d'incubation retarde le développement de la plasticité et l'apparition du stade primaire. La cinétique de mise en radeaux pourrait aussi partiellement expliquer les différences de comportement en fluage.

Plusieurs théories ont déjà été proposées afin d'expliquer le phénomène de mise en radeaux ou le changement de forme d'une particule en présence d'une contrainte appliquée. Cependant, la mise en radeaux des précipités γ' peut aussi se produire en l'absence de contrainte appliquée, si un alliage est tout d'abord prédéformé puis ensuite recuit. Certains auteurs ont avancé comme principale explication la répartition anisotrope des dislocations de matrice sous l'effet des contraintes de cohérence lors de la prédéformation. Cela signifie que la mise en radeaux est tout d'abord causée par les contraintes résiduelles apportées lors de la déformation plastique de la matrice. Elles doivent avoir un effet similaire à celles créées au cours des premières heures d'un test de fluage. Ces contraintes résiduelles ainsi que l'énergie élastique associée peuvent ensuite relaxer au cours d'un recuit ultérieur à haute température par un changement de morphologie des particules γ'.

Dans cette étude, on se propose d'étudier par diffusion de neutrons aux petits angles (DNPA) les transformations microstructurales ayant lieu au cours d'un recuit à haute température (1100ºC) dans un échantillon prédéformé. On obtient ainsi des informations sur les transitions de morphologie des précipités γ' ainsi que sur la cinétique de ces transitions. En complément, des observations en microscopie électronique à balayage (MEB) sont présentées. D'autre part, il a été montré que des expériences in-situ de diffraction de rayonnement synchrotron permettent la mesure du désaccord paramétrique entre les phases γ et γ' et de caractériser l'état de contrainte interne de l'échantillon. On espère ainsi pouvoir observer pendant le recuit la relaxation des contraintes internes apportées par la prédéformation plastique avant le recuit. Pour finir, nous proposons une analyse élastique du système en prenant en compte, non pas la contrainte appliquée mais la déformation plastique dans la matrice γ. Une mise en relation avec le comportement en fluage des superalliages de nickel ainsi que l'influence de leur composition sont ensuite discutés.

2-Programme expérimental

Dans un premier temps, on se propose de caractériser la microstructure initiale de l'alliage MC-NG par les techniques de diffusion de neutrons aux petits angles

(DNPA) et de microscopie électronique à balayage. La DNPA consiste à irradier un échantillon présentant un contraste en termes de densité de longueur de diffusion par un faisceau de neutrons monochromatique et à étudier le signal diffusé aux petits angles. Ce signal contient à la fois des informations relatives à la taille, la forme et l'arrangement spatial des particules. Néanmoins, l'interprétation des résultats n'est pas toujours simple et des observations directes en microscopie électronique à balayage (MEB) peuvent la faciliter. Ces deux techniques complémentaires renseignent sur la taille et la forme des particules, ainsi que sur leur arrangement spatial.

D'autre part, la technique de DNPA permet d'observer la cinétique de mise en radeaux des précipités γ' au cours d'un recuit a haute température d'un échantillon dans lequel de la déformation plastique a préalablement été introduite. En comparant avec des études similaires conduites sur des alliages de composition différente, nous pourrons discuter l'influence de la composition chimique sur la cinétique de mise en radeaux. Des observations complémentaires au MEB permettent de caractériser la microstructure en fin de recuit.

Parallèlement, la technique de diffraction de rayonnement synchrotron à haute résolution va permettre de suivre l'évolution du désaccord paramétrique au cours de la mise en radeaux des précipités γ'. L'observation des structures de dislocations avant et après mise en radeaux par microscopie électronique en transmission permet l'identification des micromécanismes mis en jeu.

3. Résultats expérimentaux

D'un point de vue microstructural, la combinaison des observations MEB et des expérience de DNPA ont montré que les particules γ' adoptent une forme cuboïdale et forment un arrangement périodique de particules le long des axes <100> du monocristal après traitement thermique standard. Par ailleurs, en comparant avec les résultats obtenus sur l'AM1 (alliage de première génération), on voit que les précipités ont une forme se rapprochant plus de celle d'un cube dans le cas du MC-NG, et que leur taille moyenne est plus petite. Ces deux points peuvent être mis en

relation avec la présence de rhénium et de ruthénium dans la composition du MC-NG, correspondant à une hausse de l'énergie d'interface γ/γ'.

Les expériences *in-situ* de DNPA ont montré que la cinétique de mise en radeaux était similaire dans les deux alliages AM1 et MC-NG. Dans ce cas, les dislocations et/ou les lacunes introduites au cours de la déformation plastique servent de court circuit pour la diffusion des atomes au cours du recuit a très haute température. Néanmoins, la microstructure en radeaux obtenue en fin de recuit à haute température dans le cas du MC-NG est bien plus irrégulière que dans le cas de l'AM1. La taille des lamelles de phase γ' est, pour une durée de recuit comparable, plus petite dans le MC-NG que dans l'AM1. De plus, la température de recuit semble jouer un rôle prépondérant sur les mécanismes impliqués dans la mise en radeaux, puisque deux comportements différents sont observés à 1050°C et à 1100°C.

Par ailleurs, les expériences de diffraction haute résolution ont montré que la mise en radeaux est accompagnée d'une relaxation anisotrope du désaccord paramétrique apparent. Le misfit perpendiculaire à l'axe de déformation est relaxé tandis que celui parallèle à l'axe de déformation augmente. Cette relaxation anisotrope observée après analyse de l'évolution des profils de diffraction n'est cependant pas réelle et peut s'expliquer si on considère l'évolution microstructurale du matériau.

Des observations au microscope électronique en transmission ont montré qu'un réseau de dislocations se forme sur les interfaces γ/γ' perpendiculaires à l'axe de déformation. La densité de ce réseau de dislocations est intimement liée au montant de déformation plastique préalablement introduite dans le matériau. Une fois encore, la température du recuit semble influer sur les mécanismes mis en jeu. En effet, pour un recuit effectué à 1050°C, la relaxation du désaccord paramétrique perpendiculaire a lieu de façon lente et continue, tandis qu'elle peut être décomposée en deux étapes si le recuit est réalisé à 1100°C.

4. Analyse élastique

Les expériences décrites ci-dessus ont montré que la mise en radeaux des précipités γ' pouvait avoir lieu dans des échantillons prédéformés puis recuits à haute température. Pour une prédéformation plastique du type traction, les précipités initialement cuboïdaux adoptent pendant le recuit une forme de disque dont la normale est parallèle à l'axe de traction. Par ailleurs, une forte relaxation des contraintes internes accompagne les changements de morphologie des précipités γ'. Nous proposons un modèle basé sur la théorie des inclusions avec anisotropie d'élasticité afin de prédire la forme des particules γ' après la mise en radeaux. Ce modèle permet de reproduire de façon fidèle les résultats expérimentaux. Après extension, il peut aussi se corréler avec le comportement en fluage des superalliages de nickel monocristallins. L'utilisation de ce modèle a par ailleurs permis de quantifier l'influence du désaccord paramétrique et du champ de contraintes associé sur les mécanismes de déformation.

5. Conclusion

L'ensemble des résultats expérimentaux montre que la composition de l'alliage a peu d'influence sur la cinétique de mise en radeaux des précipités γ'. Ce phénomène surprenant peut s'expliquer si on considère les dislocations et les lacunes introduites lors de la déformation plastique comme des courts-circuits de diffusion. La mise en radeaux a donc lieu par interdiffusion des atomes constituant les phases γ et γ' a travers ces courts-circuits de diffusion. Néanmoins, la microstructure finale dépend fortement de la composition de l'alliage, en modifiant notamment l'énergie d'interface. Les travaux de modélisation ont de plus montré que plus la matrice est durcie d'un point de vue mécanique, plus la durée de vie de l'alliage en fluage est élevée.

Table of Contents

Chapter 3 Presentation and discussion of the experimental results

Chapter 4 Elasticity analysis

Chapter 5 General discussion

Introduction

The increase of the gas temperature at the turbine inlet in aircraft engines has led to extensive research projects for the improvement of the techniques used in the manufacture of these critical components. Turbine blades are subject to high mechanical solicitations at high temperature. The centrifugal forces are 50 to 100 thousand times the component weight at working temperature between 750°C and 1100°C [1], leading to creep and oligo-cyclic fatigue damaging the component. Increasingly complex internal cooling circuits were introduced in the design of turbine blades, in order to increase the working temperature in combustion chambers by keeping the metal temperature below that of the gas. The use of chemically complex nickel based superalloys in the design of blades has led to an increase of the working temperature to about 1100°C. At such temperatures, the material constituting the component must be resistive to corrosion and to the oxidant atmosphere made of combustion gases. The addition of chromium in the composition of superalloys has fulfilled this requirement. In addition, they must exhibit a good resistance to thermomechanical fatigue and excellent mechanical properties at temperatures higher than 750°C. As they exhibit a peak in yield stress around 830°C [2], nickel based superalloys were confirmed to be an adequate material in the design of turbine blades and other critical components.

The peculiar properties of these materials arise from the presence of two face centred cubic (fcc) phases. The γ matrix is a fcc solid solution of austenitic type mainly constituted of nickel and the γ' precipitates form the chemically ordered (Ni_3Al type) reinforcing phase. After homogenisation heat treatment, the microstructure consists of a periodic arrangement of cuboidal γ' particles along the {100} crystallographic directions [3]. The γ and γ' phases provide solid solution strengthening and structural hardening respectively.

The evolution from polycrystalline to directionally solidified alloys resulting in a columnar structure has led to an increase of the lifetime of these materials, aligning

grain boundaries in the blade axis. As grain boundaries were found to be a weak point in terms of fatigue and creep properties, engineers have considered the elaboration of single crystal alloys. They found that the absence of grain boundaries enabled to remove boundary strengthening elements such as carbon, boron and zirconium, thus increasing the solidus temperature. The next characteristic feature in the history of elaboration of superalloys was the increase of aluminium and titanium contents. These elements promote the precipitation of the γ' reinforcing phase [3]. In modern alloys, the optimum γ' volume fraction $f_{\gamma'}$ is close to 65% [4]. The evolution towards second generation alloys and subsequently third generation with an improved chemistry was carried out during the past twenty years by General Electrics (René N5 and N6), Pratt & Whitney (PWA 1484) and Cannon Muskegon Corp. (CMSX-4 and CMSX-10) through the introduction of rhenium in the composition of the alloys. They achieved an improvement in high temperature mechanical properties.

Recently, the French group ONERA (French aerospace laboratory) has designed a new alloy, denominated MC-NG, containing rhenium and ruthenium [5]. Recent investigations carried out on this alloy have shown that its high temperature creep behaviour was different from that of alloys from previous generations. The lifetime shown by MC-NG is higher than that shown the first generation alloy AM1 [5, 6]. In both cases, the γ' particles initially cuboidal directionally coarsen to finally adopt the form of platelets during the first stage of a creep test. This morphological transition, also called rafting of γ' particles, makes the development of plastic flow more difficult and leads to a constant creep rate. On the other hand, it was found that directional coarsening of γ' precipitates, similar to that observed during a creep test, occurs during ageing at high temperature (around 1100°C) in a superalloy that was formerly plastically deformed [7-9]. This phenomenon is also called strain induced rafting. It clearly appears from these observations that there is a strong correlation between plastic deformation, microstructure and alloy composition.

A possible explanation for the improved high temperature creep properties shown by the MC-NG alloy with respect to the AM1 could be a longer kinetics of rafting induced by the differences in chemical composition and therefore atomic diffusion

coefficients. In the present work, we aim at investigating the strain induced rafting phenomenon in the MC-NG alloy in order to confirm this hypothesis. After a review of the data found in the literature, the different techniques used in this investigation are presented. Small angle neutron scattering (SANS) gives access to the characterization of the bulk microstructure evolution that occurs during rafting of the γ' particles. If used in-situ, this technique provides information on the kinetics of rafting. It is found that the alloy composition does not strongly influence the kinetics of rafting. These results are completed with scanning electron microscopy (SEM) observations. Systematic comparison with a first generation alloy (AM1) allows the determination of the influence of the alloy composition on the kinetics of rafting and on the final microstructure. Moreover, the evolution of the internal strains during strain induced rafting is obtained by synchrotron diffraction. An anisotropic relaxation of the lattice parameter mismatch is observed. Combined with transmission electron microscopy (TEM) observations, the dislocation mechanisms involved in this morphological transformation are discussed. A model based on the inclusion theory of anisotropic elasticity is finally presented in order to discuss the role of plastic strain in rafting and to predict the morphology change of the γ' particles. It is found that precipitation misfit strain is required for rafting to occur and that plastic strain discriminates the final microstructure.

CHAPTER 1 Single crystal nickel based superalloys

I.1 Microstructure of single crystal superalloys

In this first section we describe the historical evolution of the single crystals superalloys composition. The effect of each addition element and its partitioning in the phases of the material will be described. A brief review of the elaboration processes of superalloys and the associated mechanisms is also presented. Finally, emphasis is laid on the mechanical properties of these materials.

I.1.1 Composition of single crystal Ni based superalloys

The composition of single crystal nickel based superalloys is classified in terms of generations. Alloys from the first generation are those which do not contain rhenium (Re). Below 3wt% of rhenium, the alloys belong to the second generation and above this limit to the third generation. Table 1.1 shows the composition of some single crystal superalloys [6]. The composition of the alloys from the first generation is derived from that of directionally solidified polycrystalline alloys, *i.e.* those showing a columnar grain structure. By suppressing the grain boundaries and the elements such as carbon, zirconium or boron (initially introduced to strengthen the grain boundaries), the mechanical performances of those superalloys were dramatically improved [10]. It was then found that refractory elements such as tungsten (W) and molybdenum (Mo) could be advantageously replaced with rhenium (Re) to improve the mechanical properties [11]. Nevertheless, rhenium is expensive and it increases the density of the material. Another alternative had to be found if industrial use of the alloy was to be considered. Recently, a new heavy refractory element appeared in the design of single crystal superalloys. The O.N.E.R.A and General Electrics have submitted a patent for the ruthenium element, as a partial replacement of rhenium. These patents claim that ruthenium has a hardening effect comparable to that of rhenium at high temperature. Moreover it is lighter and does not favour the precipitation of intermetallic phases. A new ruthenium containing alloy was then

designed and designated as MC-NG [5]. In this work, all experiments are carried out on this new alloy. We can deduce some information on the influence of the ruthenium addition by comparing the data with those obtained with a first generation generation, such as the AM1.

	ALLOY	Cr	Co	W	Mo	Re	Al	Ti	Ta	Hf	others	density g/cm^3
First Generation	AM1	7,8	6,5	5,7	2	-	5,2	1,1	7,9	-	-	8,6
	Nasair 100	9	-	10,5	1	-	5,75	1,2	3,3	-	-	8,54
	CMSX-2	8	4,6	7,9	0,6	-	5,6	1	6	-	-	8,6
	CMSX-3	8	4,6	7,9	0,6	-	5,6	1	6	0,1	-	8,6
	TMS-1	5,5	7,5	16,6	-	-	5,2	-	5,1	-	-	9,1
	PWA 1480	10	5	4	-	-	5	1,5	12	-	-	8,7
	René N4	9	8	6	2	-	3,7	4,2	4	-	0.5 Nb	8,56
	SRR 99	8	5	10	-	-	5,5	2,2	3	-	-	8,56
	RR 2000	10	15	-	3	-	5,5	4	-	-	1 V	7,87
	CMSX-6	8	4,6	7,9	0,6	-	5,6	1	6	0,1	-	7,98
	AM3	8	5,5	5,7	2	-	6	2	3,5	-	-	8,25
	MC2	8	5	8	2	-	5	1,5	6	-	-	8,63
Second Generation	CMSX-4	6,5	9	6	0,6	3	5,6	1	6,5	0,1	-	8,7
	PWA 1484	5	10	6	2	3	5,6	-	8,7	0,1	-	8,95
	René N5	7	8	5	2	3	6,2	-	7	0,2	-	8,7
Third Generation	CMSX-10	2	3	5	0,4	6	5,7	0,2	8	0,03	0.1 Nb	9,05
	René N6	4,2	12,5	5,4	1,4	5,4	5,75	-	7,2	0,15	0.05 C	8,97
	MC-NG	4	-	5	1	4	6	0,5	5	0,1	4 Ru	8,75

Table 1.1: Chemical composition of different superalloys (wt%). The Ni content balances the whole composition.

I.1.2 Influence and partitioning of the addition elements

The microstructure of single crystal nickel based superalloys consists of two phases. The γ austenitic matrix is a face centred cubic (fcc) solid solution mainly composed of nickel atoms and some substitution additional elements. In this solution, γ' precipitates are embedded, their structure is of $L1_2$ or $Ni_3(Al, Ti)$ type. It is shown in Figure 1.1. These γ' precipitates generally have a cuboidal shape and are regularly arranged in the matrix along the {100} crystallographic directions. Aluminium (Al), titanium (Ti), tantalum (Ta), niobium (Nb) and vanadium (V) are the γ' forming elements. Chromium (Cr), molybdenum (Mo), tungsten (W), rhenium (Re) and ruthenium (Ru) have a weak influence on the formation of the γ' precipitate phase and are therefore preferentially dissolved in the γ matrix. Table 1.2 shows the

partitioning of the addition elements in the γ and γ' phases. Cr and Al are the elements that protect the material from corrosion and oxidation by forming a Cr_2O_3 or Al_2O_3 oxide surface layer. In some alloys, the precipitation of intermetallic compounds or Topologically Closed Pack (TCP) phases may occur. The presence of these TCP phases is not desirable as they tend to deteriorate the mechanical properties [12]. The transition elements such as Cr, W, Mo and Re promote the formation of TCP phases [13, 14]. As mentioned before, this phenomenon can be compensated by the replacement of rhenium by ruthenium. Past investigations carried out on alloys containing both rhenium and ruthenium have shown that these two elements tend to increase the transition temperature between heterogeneous and homogeneous dislocation distribution during plastic deformation [15]. In such alloys, the deformation was shown to be very heterogeneous at temperatures below 750°C (see section I.2.3 for more details).

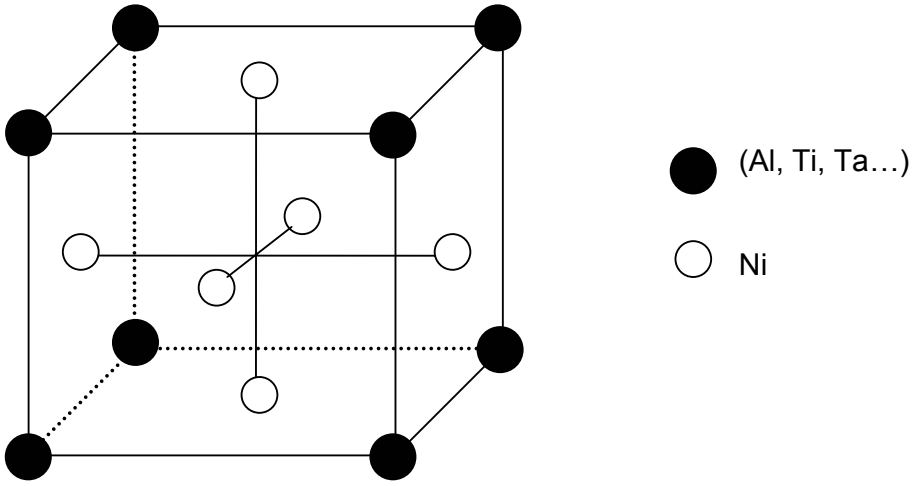

Figure 1.1: $L1_2$ unit cell. The nickel atoms are at the centre of each face of the cube.

Alloy	Cr	Co	W	Mo	Re	Al	Ti	Ta	Ru	Reference
AM1	12,4	5,3	1,2	3,6	-	0,2	0,19	0,19	-	[16]
MC2	14,4	2,6	1,3	4,7	-	0,15	0,1	0,14	-	[17]
CMSX-2	12	2,9	1	3	-	0,17	0,42	0,15	-	[18]
PWA 1480	15,7	3,6	1,3	-	-	0,18	0,06	0,12	-	[18]
CMSX-4	9,4	3,3	1,6	2,8	16	0,1	0,12	0,07	-	[19]
RR 3000	6	2,5	1,5	2	16	0,3	0,25	0,22	-	[20]
MC-NG 850°C	6,3	-	0,9	2,5	11,5	0,19	0,17	0,07	4	[6]
MC-NG 1050°C	4,1	-	1,2	2	8	0,45	0,38	0,23	2,2	[6]

Table 1.2: Partitioning coefficient $k_i = C_\gamma^i / C_{\gamma'}^i$ between γ and γ' phases for different addition elements.

On the other hand, the presence of γ and γ' phases in superalloys induces two hardening phenomena. Firstly, the γ matrix is at the origin of solid solution strengthening. The composition of the alloy plays in that respect an important role. Secondly, the γ' precipitates induce a structural hardening. As γ' is a chemically ordered phase, the shearing of the particles by a single dislocation is energetically unfavourable. The mechanism controlling deformation is the pseudo Orowan by-passing of the precipitates. Moreover, the difference in chemical composition between γ and γ' phases leads to the existence of a lattice parameter mismatch at γ/γ' interfaces. This point will be discussed in more details in section I.2.3.

I.1.3 Production processes and associated mechanisms

Single crystal nickel based superalloys are produced by directional solidification. The conditions of production, such as thermal gradient and speed of solidification front, lead to the growth of dendrites along the desired crystallographic direction. The natural growth direction of single crystal nickel superalloys is <001>. This orientation provides, among other things, the best equilibrium in terms of creep resistance, strength and fatigue properties [21]. Typically, in the as-cast conditions, the dendrites contain the γ matrix in which are embedded fine and uniform γ' particles. The interdendritics areas contain the γ/γ' eutectic and massive γ' particles at the dendrites boundaries [3]. The average spacing between dendrites strongly depends on the thermal gradient at the solidification front. However, it was shown that the choice of the production conditions (thermal gradient…) does not alter high temperature creep properties [22].

In order to homogenise the chemical segregations observed in the core of the dendrites and to suppress the γ / γ' eutectic, a homogenisation thermal treatment is usually carried out. It typically consists in an isothermal treatment at 1300°C for three hours followed by air cooling. The resulting dendrite structure is shown in Figure 1.2. At very high temperature (above 1300°C), the solutionising of γ' particles is complete. During cooling from the one phase field γ, there will be a critical temperature below which the γ' particles start to form.

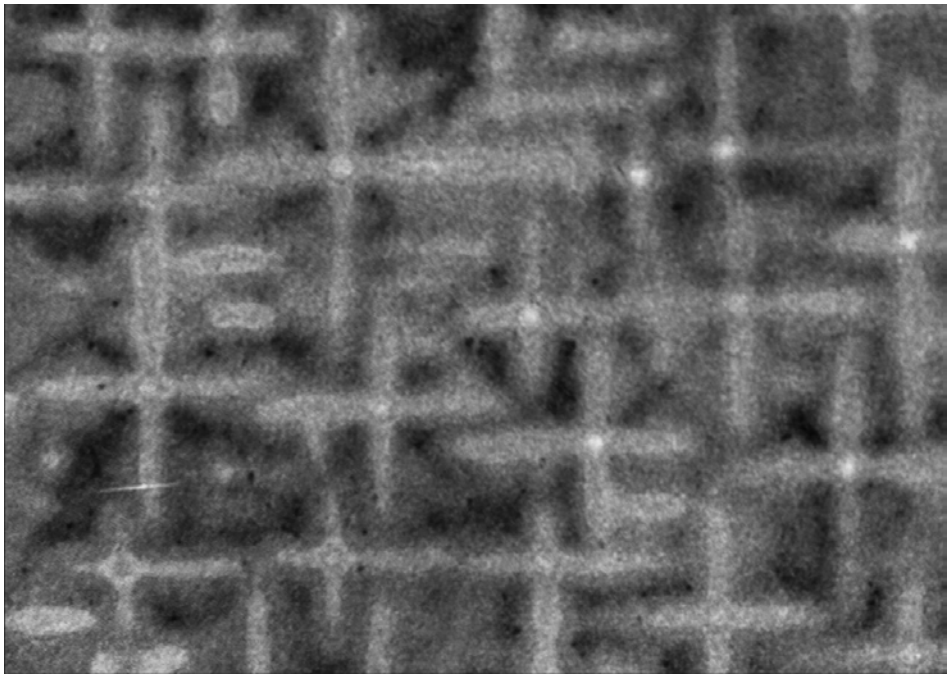

Figure 1.2: Dendrite structure obtained after homogeneisation thermal treatment in MC-NG.

There are three variables which drive the γ' precipitation reaction [23]:

-the difference of chemical energy of the phases per unit volume $\Delta g_{\gamma\gamma'}$

-the particle/matrix interfacial energy $f_{\gamma\gamma'}$

-the total elastic strain energy per unit volume of particle $W_{\gamma\gamma'}$ associated to the lattice mismatch between precipitates and matrix and including interactions between particles.

If $V_{\gamma'}$ is the volume occupied by the particles and $F_{\gamma'}$ the particle/matrix interfacial area, the variation of the Gibbs energy necessary for the formation of the γ' particles $\Delta G_{\gamma\gamma'}$ is given by [23]

$$\Delta G_{\gamma\gamma'} = -V_{\gamma'} \cdot \Delta g_{\gamma\gamma'} + F_{\gamma'} f_{\gamma\gamma'} + V_{\gamma'} W_{\gamma\gamma'} \qquad (1.1)$$

The prevalence of the interfacial energy over the elastic strain energy in equation (1.1) determines the character of the reaction (respectively diffusion or strain driven) as well as the morphology and the size of the γ' precipitates. Nucleation and growth of the precipitates take place at any temperature below the critical undercooling (about 30°C below the γ' solvus point) [24, 25]. Coarsening is described by Ostwald

ripening in the LSW model [26, 27]. A theoretical analysis was developed by Kachaturyan et al. to model morphological changes occurring during coarsening of cubic precipitates [28, 29]. Their model implies that, above a critical precipitate size; the elastic strain energy prevails over the particle/matrix interfacial energy. This leads to a morphological shape transition. The big particles split into smaller ones, leading to a decrease in total elastic energy. The following shape transitions were predicted: cube -> doublet -> octet, as shown on Figure 1.3. Nevertheless, these calculations are based on the final precipitates' arrangement and do not consider the transition states. Colin et al. [30] have shown that splitting is energetically favourable, although an 'activation' energy or a crack in the γ' particle is needed to start the splitting. However, no origin for this activation energy was proposed. Yamabe and Harada [31] explain the particle splitting in terms of chemical composition fluctuation from the equilibrium state. Recent experimental investigation of γ' precipitation and growth by means of small-angle neutron scattering [32] support the sequence of morphological changes predicted by Kachaturyan et al. Furthermore, the γ' precipitates first nucleate in the matrix under the form of small spherical particles that become cuboidal during growth under the effect of elastic anisotropy. In addition, it was found that the transition from spherical to cuboidal particles occurs at the temperature where the rate of misfit decrease (due to composition change) is maximum [33], thus confirming the role played by elastic energy in the precipitation of the γ' phase.

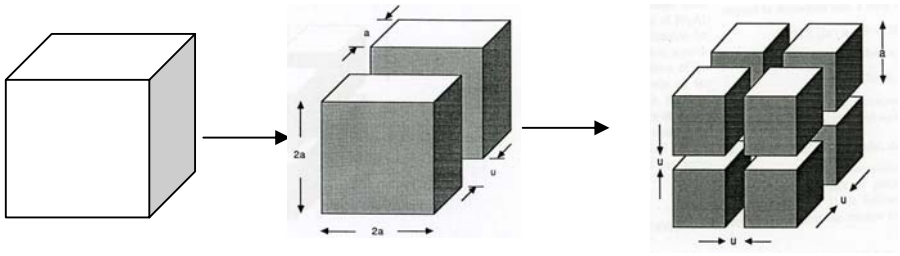

Figure 1.3: Morphological shape transitions of γ' precipitates during cooling as predicted by Kachaturyan et al.[28].

The microstructure resulting from the homogenisation thermal treatment consists in a regular arrangement of γ' precipitates aligned along the <100> crystallographic directions under the effect of elastic energy of interaction between particles [34]. This is shown in Figure 1.4. Nevertheless, the size and the arrangement of the γ' particles may not correspond to the optimum ones in terms of mechanical properties. Both features can be adjusted by further annealing at temperatures around 900°C. Figure

1.5 shows the microstructure of the CMSX-2 alloy obtained after two different annealing treatments that we will call T1 (980°C / 5h / air cooling + 850°C / 24h) and T2 (1050°C / 16h / air cooling + 850°C / 24h). We can see that after the T1 treatment, growth of γ' precipitates has occurred. The average size is then d=300nm. Nevertheless, the arrangement of the particles is rather irregular. After the T2 treatment, which shows an average particle size d=450nm, the γ' precipitates are aligned along the {100} crystallographic axes and tend to adopt a cubic morphology [6].

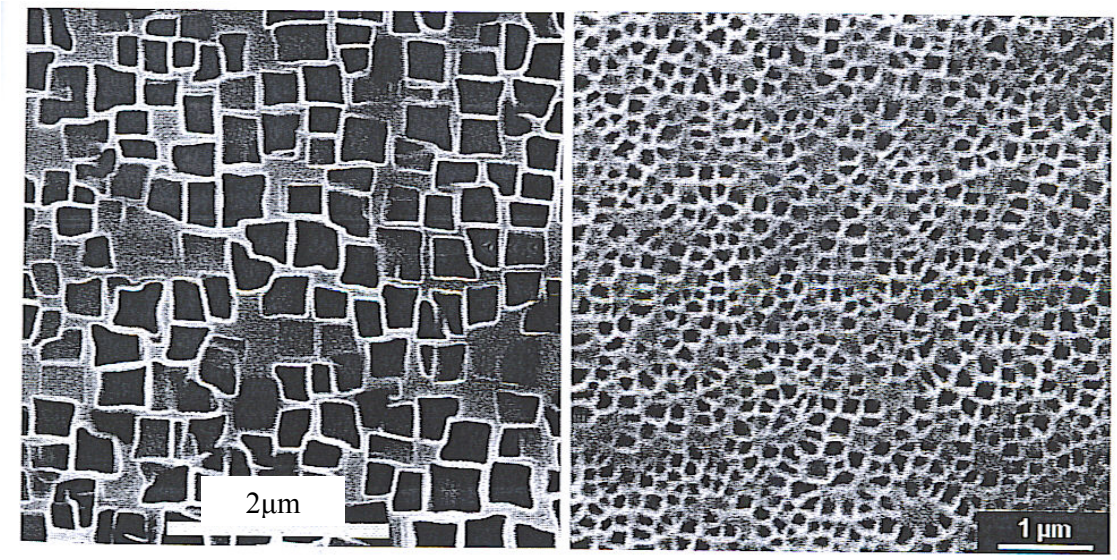

Figure 1.4: Microstructure of the AM1 (left) and MC NG (right) alloys after homogenisation thermal treatment.

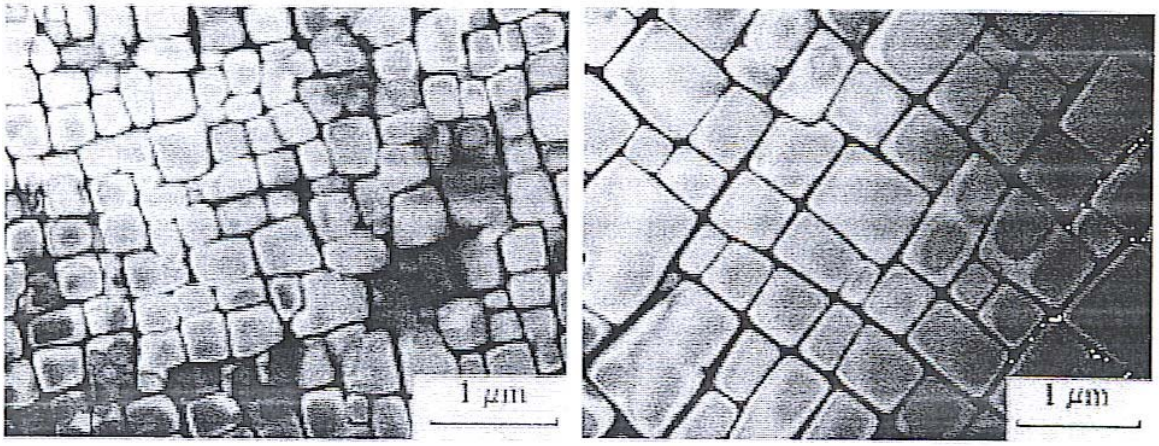

a) after T1 thermal treatment b) after T2 thermal treatment

Figure 1.5: CMSX-2 microstructures obtained after two different annealing treatments (white: γ', black: γ).

I.2. Deformation mechanisms

In this section, we will focus on the mechanical behaviour of nickel based single crystals superalloys. After a presentation of the deformation mechanisms reported in each phase, we will discuss the strengthening modes.

I.2.1 Influence of γ' volume fraction on creep properties

The mechanical behaviour of a single crystal nickel based superalloy strongly depends on the volume fraction of γ' precipitates. The γ' volume fraction is directly related to the content of γ' forming elements, such as Al, Ti, Ta and Nb. It is usually set around 65-70% at room temperature as this corresponds to the optimum value in terms of mechanical properties, as shown in Figure 1.6 [4]. During a temperature increase up to around 1050°C, the γ' phase starts to dissolve, leading to a decrease in its volume fraction. Different techniques such as scanning electron microscopy [35] or high energy X-ray diffraction [36] can be used to investigate the evolution of γ' volume fraction with temperature. It was found that the γ' phase starts to dissolve at temperatures above 1000°C in the MC-NG superalloy [6]. The evolution of the γ' volume fraction with temperature in the MC-NG alloy is shown in Figure 1.7.

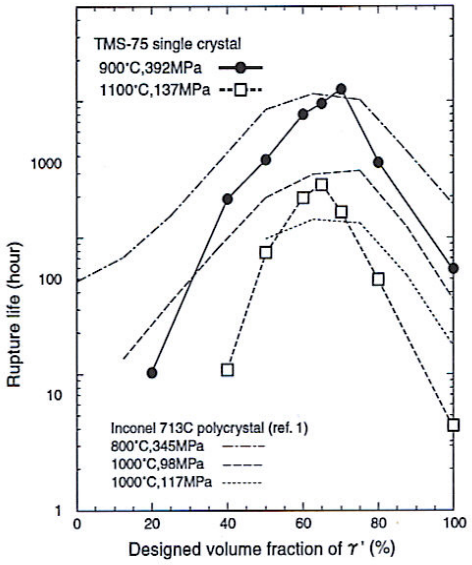

Figure 1.6: Influence of room temperature γ' volume fraction on the creep properties in Ni based superalloys [4].

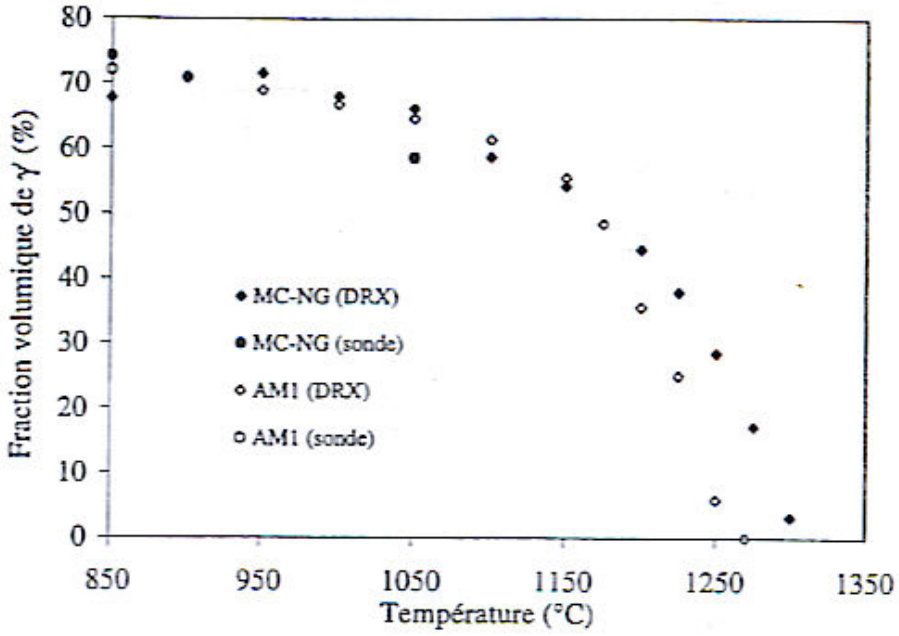

Figure 1.7: Evolution of the γ' volume fraction with temperature in the AM1 and MC-NG alloys determined with X-ray diffraction (DRX) and atomic microprobe spectroscopy (sonde) [6].

I.2.2 Deformation mechanisms of the γ phase

The plastic deformation usually initiates in the γ matrix, as it is generally the softer phase. Perfect dislocations of type $\frac{a}{2}\langle 011\rangle$ glide on the most packed planes $\{111\}$, as shown in Figure 1.8a. A perfect dislocation dissociates into two Shockley partials, as shown in Figure 1.8b. This decomposition process is accompanied with the creation of an intrinsic stacking fault (ISF). We can describe the dissociation reaction:

$$\frac{a}{2}\langle 110\rangle \Rightarrow \frac{a}{6}\langle 211\rangle + ISF + \frac{a}{6}\langle 12\bar{1}\rangle \qquad (1.2)$$

Such a reaction with creation of stacking faults was observed in the AM1 alloy by Décamps et al [37].

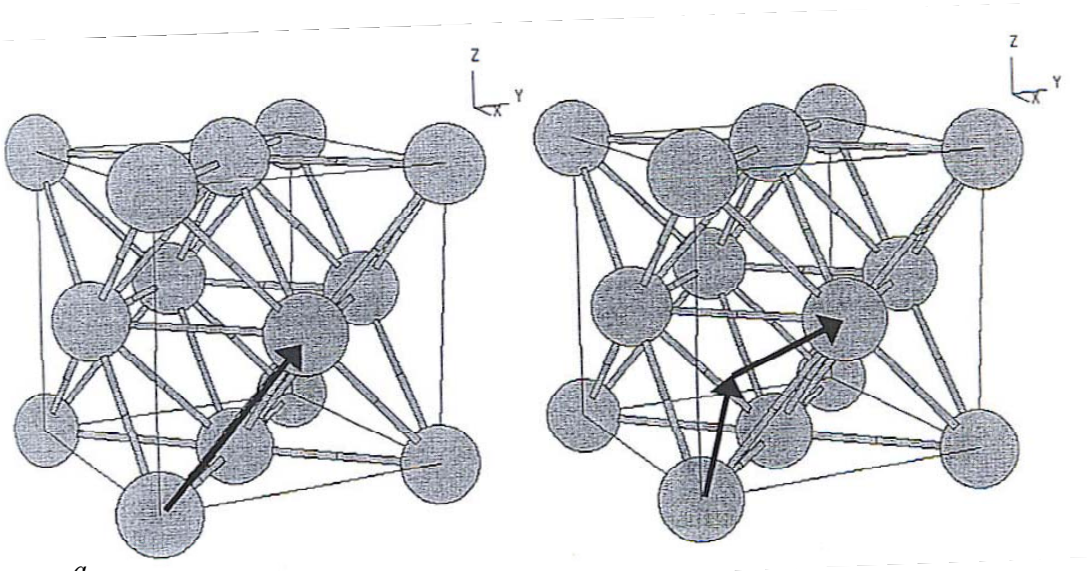

a) $\frac{a}{2}\langle 110\rangle$ perfect dislocation in a fcc structure

b) Dissociation of a perfect dislocation into two Shockley partials with creation of a stacking fault in a fcc structure

Figure 1.8: Dislocations in the γ matrix

I.2.3 Deformation mechanisms of the γ' phase

As γ' is an ordered phase, a perfect dislocation is no longer of $\frac{a}{2}\langle 011\rangle$ type but of $a\langle 011\rangle$ type. This dislocation usually dissociates into two partial dislocations, creating an anti phase boundary (APB), according to equation (1.3).

$$a\langle 011\rangle \Rightarrow \frac{a}{2}\langle 011\rangle + APB + \frac{a}{2}\langle 011\rangle \qquad (1.3)$$

The following shear mechanism is commonly observed in the γ' phase of superalloys after tensile testing at temperatures close to room temperature [38-40] or after a creep test at high temperature [41]. Two perfect matrix dislocations $\frac{a}{2}\langle 110\rangle$ shear the γ' precipitate with the creation of an APB.

Another shear mechanism of the γ' phase was also observed in the intermediate temperature range (around 760°C) [42-44]. Two perfect matrix dislocations combine at the γ/γ' interface and then dissociate into two Shockley superpartials. This

dissociation reaction is accompanied with the creation of super intrinsic/extrinsic stacking faults (SISF/SESF), according to equation (1.4).

$$\frac{a}{2}\langle 10\bar{1}\rangle + \frac{a}{2}\langle 1\bar{1}0\rangle \Rightarrow \frac{a}{3}\langle 2\bar{1}\bar{1}\rangle + SISF + \frac{a}{3}\langle 2\bar{1}\bar{1}\rangle + SESF + \frac{a}{3}\langle \bar{1}2\bar{1}\rangle \quad (1.4)$$

Another mechanism was more recently proposed by Décamps et al.[45]. The γ' particle is sheared by a single perfect matrix dislocation, leading to the creation of an APB. This APB is then transformed to a SISF or SESF by the germination of a Shockley partial, according to equation (1.5) [46, 47]. If a second dislocation shears the γ' particle, the dislocation structure becomes identical to that described in equation (1.4).

$$\frac{a}{2}\langle 0\bar{1}\bar{1}\rangle \Rightarrow \frac{a}{6}\langle \bar{2}11\rangle + SISF + \frac{a}{3}\langle \bar{1}2\bar{1}\rangle \qquad (1.5)$$

I.2.4 Strengthening effects in γ/γ' alloys

As previously mentioned, plastic deformation usually initiates in the γ matrix. The matrix can be decomposed in two types of domains, corresponding to the horizontal and vertical matrix channels with respect to the deformation axis. These channels or corridors are delimited by the γ' particles. The Orowan stress, that is the minimum stress to apply to bow out a dislocation in the γ corridors, is equal to

$$\sigma_{or} = \sqrt{\frac{2}{3}}\frac{\mu b}{h} \qquad (1.6)$$

where μ is the shear modulus, b the dislocation Burgers vector and h the width of the γ channel. As mentioned above, shearing of a γ' particle by a single perfect matrix dislocation leads to the creation of an APB that increases the total energy. This is due to the $L1_2$ chemical order of the γ' phase. Moreover, the energy associated with the APB depends on the composition of the γ' phase. The APB energy of the pure Ni_3Al compound was estimated to be around 180mJ/m^2 [48]. The replacement of 1 at% Al with 1 at% Ta increases this energy to 240mJ/ m^2 and that of 6 at% Al with 6 at% Ti to 250mJ/ m^2. We can conclude that Ti and Ta tend to increase the APB energy, what reduces the probability for a single matrix dislocation to shear a γ' particle. However, the influence of other addition elements on the APB energy is not

well established. They may decrease the APB energy as it is usually lower in γ' phases than in $Ni_3(Al, Ti)$, $Ni_3(Al, Ta)$ or Ni_3Al. On the other hand, the peak in yield stress around 850°C observed in most Ni based single crystal superalloys is attributed to the $L1_2$ structural order of the γ' phase. Kear and Wilsdorf [49] have shown that the cross-slip of dislocations from the {111} planes to the {100} planes leads to the creation of Kear Wilsdorf locks and jogs. These jogs will act as a barrier to dislocation gliding in the {111} planes, thus increasing the yield stress. The decrease in yield stress occurring at higher temperatures is attributed to the glide of dislocations in the {100} planes and to shear of the γ' particles.

On the other hand, the composition of γ and γ' phases may induce a solid solution hardening in γ/γ' alloys. The solid solution strengthening usually arises from the differences in atomic radii and elastic moduli. Therefore, it is strongly correlated to the solid solution composition. In the case of superalloys, the high number and variety of addition elements provide a non negligible hardening effect [15]. At low temperature and low concentrations in nickel, the γ' forming elements such as Ti, Ta, Nb induce an increase of the yield stress. However, these elements are absent or slightly dissolved in the γ matrix and therefore contribute to a very small extent to the γ solid solution hardening. As the deformation begins in the γ phase, it is of great interest to focus on that particular point. The influence of alloying elements in the γ matrix was investigated in model solid solutions [15]. Focus was made on the influence of tungsten, rhenium, and ruthenium on the yield stress in the temperature range between -200°C and 900°C. The outcome of the investigation is that no noticeable effect of those three elements was observed on the yield stress. This phenomenon was explained by the fact that the investigated matrices are close to saturation in terms of solute atoms such as W, Re and Ru [50]. Nevertheless, the γ phase is also characterized by a short range order (SRO) and/or $L1_2$ type long range order [51]. In these conditions, the movement of a dislocation is accompanied with a decrease in SRO, that increases the chemical energy of the solid solution. Thus, extra work is required for dislocation movement if compared with a solid solution without SRO. The deformation mechanism is the pile-up of dislocations with a formation of pairs of dislocations at the pile head [52]. This is explained by the existing SRO in the γ matrix.

According to equation (1.2), a perfect matrix dislocation usually dissociates into two Shockley partials with the creation of a stacking fault (SF) in between. The energy associated with the creation of the SF is an important microscopic parameter that directly influences the properties and propagation modes of dislocations, such as cross slip of screw segments, climb of edge dislocations along the interfaces and shearing of γ' particles [53].

The influence of the alloying elements on the stacking fault energy (SFE) was determined through the measurement of the dissociation widths of a perfect matrix dislocation by weak beam observations in transmission electron microscopy [54]. It was found that, at room temperature, the SFE is around 30 mJ/m^2 and tends to decrease when temperature is increasing. The Re containing matrix was the one showing the highest SFE. No major evolution of the SFE was observed when the content of Re, Ru and W was varied. However, Pettinari et al. emphasize that, due to the heterogeneous nature of the SRO, the deformation is heterogeneous when the temperature is below 750°C, and becomes homogeneous beyond this temperature value. They correlated this phenomenon with the decrease in SRO beyond 750°C [50]. These authors also pointed out that the higher the Re and Ru content, the higher the transition temperature between heterogeneous and homogeneous distribution of dislocations.

The presence of refractory elements in the composition of superalloys plays also an important role in diffusion processes. Elements such as W and Re are the ones having the smallest diffusion coefficient in Nickel [55]. For a given thermal treatment, the size of the γ' particles may differ depending on the content of refractory elements, as they slow down the particle coalescence process. Moreover, mechanisms such as cross-slip and climb of dislocations, which are thermally activated, are also retarded by the presence of W and Re. Nevertheless, the influence of these elements on these processes has not been quantified.

I.2.5 Misfit strain and coherency stress field

The two phases γ and γ' have slightly different lattice parameters a_γ and $a_{\gamma'}$. It is convenient to define the lattice parameter mismatch as

$$\delta = \frac{a_{\gamma'} - a_\gamma}{a_\gamma} \qquad (1.7)$$

The definition given above is valid for the stress free misfit strain, also called unconstrained misfit. The lattice parameters a_γ and $a_{\gamma'}$ are defined when both phases separately exist, *i.e.* without any deformation. In superalloys, this lattice misfit induces elastic deformation (elastic strain and stress) in both γ and γ' phases [56] and this internal stress field exerts a force on dislocations. In low external stress conditions, the stress induced hardening is therefore due to the interactions of dislocations with the stress field created in the matrix by the presence of the γ' particles. When the γ' volume fraction is large, the coherency stress field becomes important in the γ corridors.

A high number of finite element analyses were carried out in superalloys to estimate the coherency stress filed, using isotropic [57] or anisotropic [58-60] elasticity. All these works show that, in the case of a negative misfit, the precipitate is in tension and the matrix channels in compression. Figure 1.9 shows the equivalent Von Mises stress induced by a negative lattice parameter mismatch as estimated by Pollock and Argon [60]. The coherency stress field does not vary much between 850°C and 1050°C.

As γ and γ' phases do not have the same thermal expansion coefficient, the lattice parameter mismatch evolves with temperature. Moreover, at high temperatures, the γ' phase starts to dissolve, through the migration of γ' forming elements such as Al, Ti and Ta in the γ matrix. The evolution of the mismatch with temperature is given in Figure 1.10 [6]. The decrease of the mismatch between room temperature and 750°C is attributed to the difference in thermal expansion coefficients of the γ and γ' phases. In this temperature range, the γ' volume fraction remains constant. When the temperature increases, the γ' phase starts to dissolve in the γ matrix, leading to a

change in the γ and γ' lattice parameters. Beyond 950°C, the difference in thermal expansion coefficients is no longer significant. The evolution of the lattice parameter mismatch with temperature is strongly correlated to that of the γ' volume fraction.

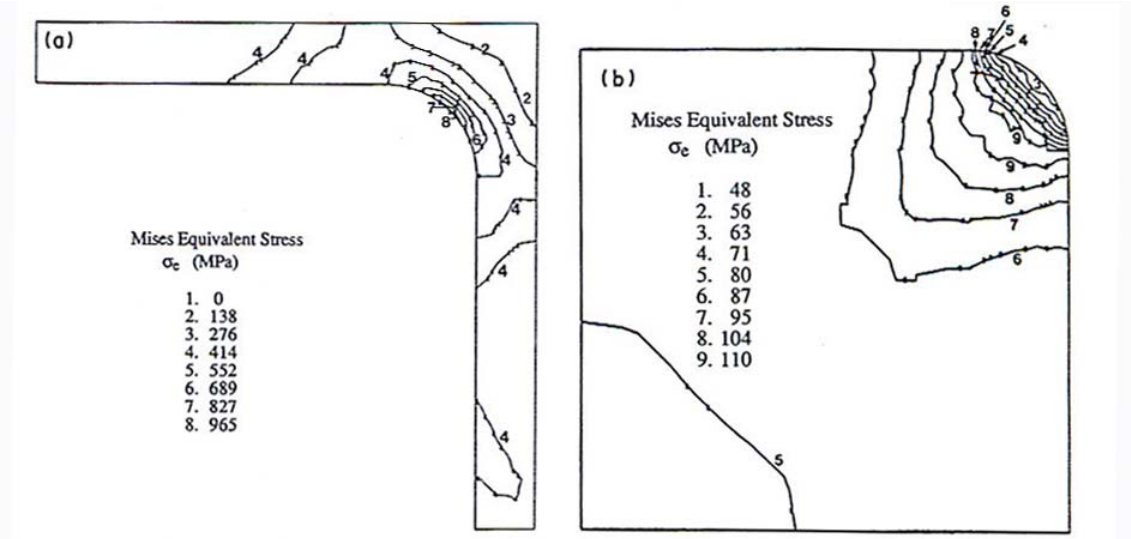

Figure 1.9: Equivalent Von Mises stress in the γ corridor (left) and in the precipitates (right) in the case of a negative lattice mismatch [60]. By symmetry, only one fourth of the representative volume is represented.

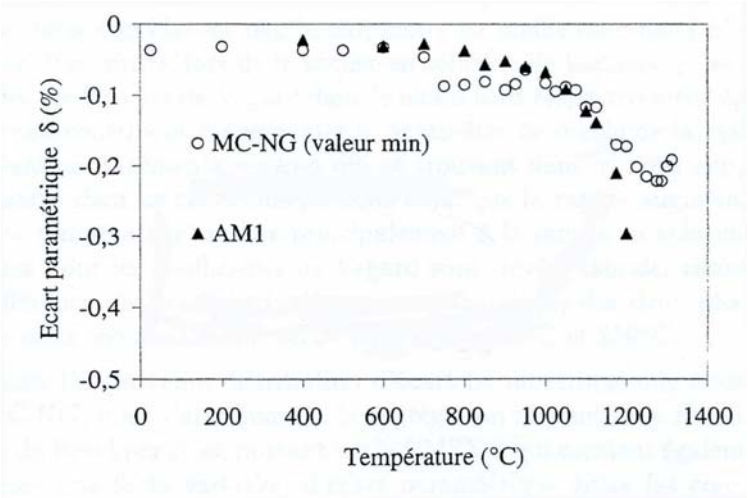

Figure 1.10: Lattice parameter mismatch evolution with temperature in the AM1 and MC-NG superalloys as from [6]

During a high temperature low stress creep test in tension, the mechanisms involved in plastic deformation will differ, depending on the amplitude of the misfit value. When the misfit is negative, the coherency stress field is relaxed by creep dislocations in the matrix channels parallel to the applied stress, whereas dislocation

glide is enhanced in perpendicular channels where the coherency stress field and the applied stress are superimposed [61]. In the case of a large lattice misfit, the superposition of the coherency stress field and externally applied stress drives loops of matrix dislocations to move by cross-slip through the matrix channels, as shown on Figure 1.11. A large lattice misfit is also related to sufficient dislocations source and large driving force for dislocation reorientation at γ/γ' interfaces. When the misfit is small, the driving force for the dislocation to overcome the Orowan resistance is insufficient, and dislocations move by climbing around the γ' particles [62].

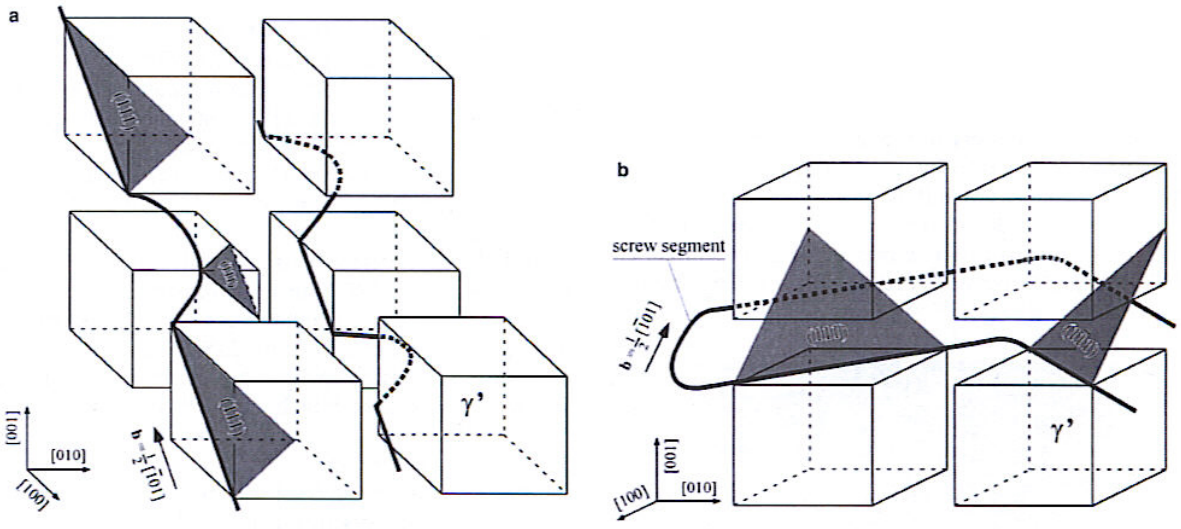

Figure 1.11: Schematic configuration of dislocation configurations at the early stages of a creep test a) small lattice misfit, dislocations are moving by a combined climbing and gliding process; b) large lattice misfit, a dislocation is moving by cross-slip in the γ matrix [62].

I.3 Creep behaviour of the AM1 and MC-NG single crystals superalloys

Turbine blades are subject to high temperatures and centrifugal forces during operation of turbo engines. The wear of these components is mainly due to creep, which becomes significant in the temperature range between 650°C and 1100°C-1200°C. Two characteristic creep behaviours can be distinguished, which apply particularly well to AM1 and MC-NG. The first one, in the intermediate temperature regime (around 800°C) does not involve any microstructure evolution, contrary to the

second one, in the high temperature regime. The microstructure evolution observed in the second case is of great importance to explain the observed creep behaviour. Moreover, the alloy composition, particularly the content in heavy refractory elements, will influence the diffusion processes involved in the microstructure evolution and therefore the creep behaviour.

I.3.1 Creep behaviour in the intermediate temperature range

At temperatures below 850°C, the initial microstructure, consisting in a periodic arrangement of γ' particles, does not evolve significantly through the creep test for AM1 and MC-NG. In this temperature range, the γ' volume fraction remains constant around 70%. Figure 1.12 represents the creep curves obtained at 760°C-840MPa in the AM1 and MC-NG superalloys [6]. In these alloys, we can distinguish two types of macroscopic behaviours at the early stages of the creep test, as seen in Figure 1.13. The first one is characterized by a very fast work hardening as soon as the stress is applied, and the second by an incubation period followed with large deformation during primary creep.

In the first case, perfect matrix dislocations are created as soon as the stress is applied. In the case of a uniaxial tensile stress applied along [001], eight equivalent slip systems of type $\langle 011 \rangle \{111\}$ are potentially activated. The interactions of these slip systems leads to forest hardening of the material. Moreover, the presence of dislocations will alter the internal stress field in order to prevent from further deformation. This is the back stress hardening. The macroscopic deformation reached at the end of the primary creep is therefore limited [63].

In the second case, the density of mobile dislocations at the start of the creep test is lower than in the previous case. The incubation period corresponds to the time necessary for the initiation of the movement of perfect matrix dislocations. During this period the macroscopic creep deformation is almost equal to zero. Cross slip of dislocations results in the creation of Frank Read sources, thus increasing the density of mobile dislocations. Secondary creep stage is reached when the work

hardening induced by back stress and forest dislocations becomes significant. Once dislocations have reached the γ/γ' interface, these perfect matrix dislocations dissociate into two Shockley superpartials of type $a/3\langle 112\rangle$, which will shear the precipitates according to the mechanism described in section I.2.2. This deformation mechanism leads to a large deformation rate, corresponding to the tertiary creep stage.

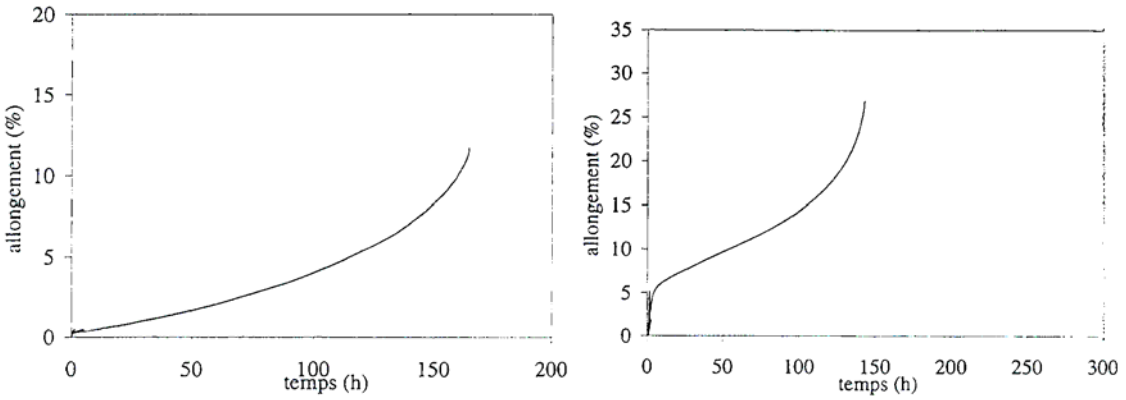

Figure 1.12: Creep behaviour at 760°C-840MPa in the AM1 (left) and MC-NG (right) superalloys. The macroscopic creep strain is plotted versus time [6].

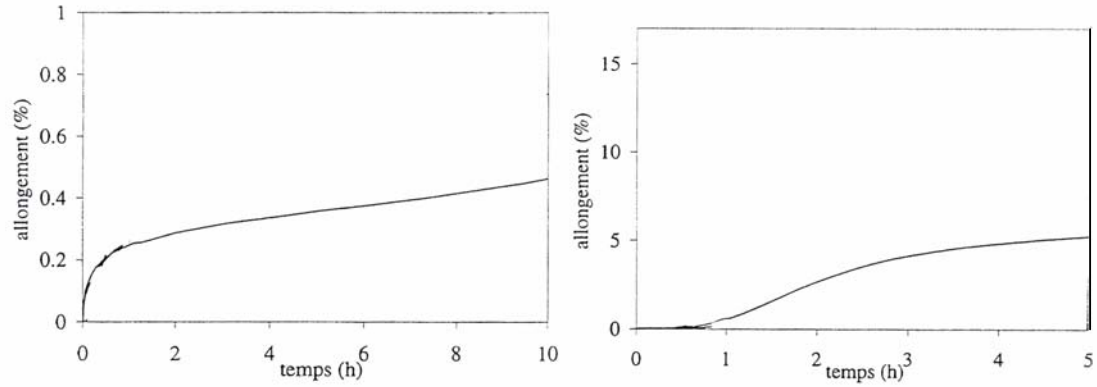

Figure 1.13: Primary creep at 760°C-840MPa in the AM1 (left) and MC-NG (right) superalloys. Two deformation modes are identified [6].

The *post-mortem* observation by means of transmission electron microscopy of the dislocation structures during primary creep has enabled the determination of the deformation mechanisms associated with the two different behaviours observed. In the case of the AM1 superalloy, the deformation occurs preferentially in the γ matrix

through the creation and propagation of perfect dislocations in the vertical and horizontal γ channels, as can be seen in Figure 1.14. In the MC-NG superalloy, the distribution of perfect matrix dislocations is much more heterogeneous, due to the presence of a SRO [15]. Some zones of the sample are depleted in dislocations, as shown in Figure 1.15. Moreover, numerous stacking faults were observed in the γ' phase, showing that particle shearing occurs.

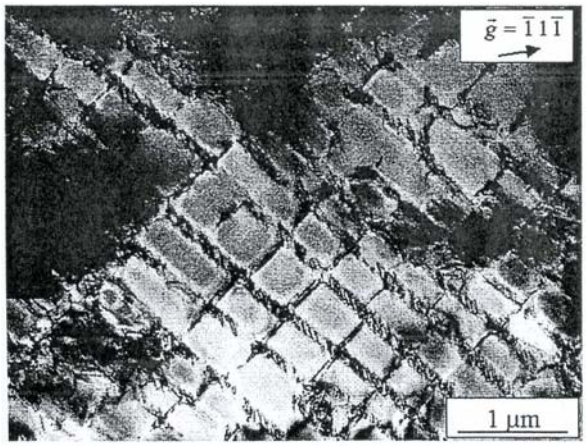

Figure 1.14: Dislocation structure in the AM1 after 1,5h creep at 760°C-840MPa.

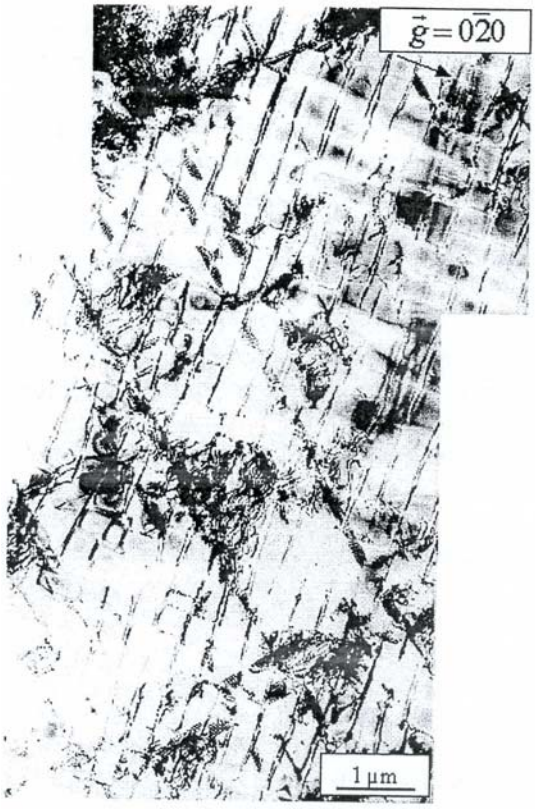

Figure 1.15: Dislocation structure in the MC-NG after 1,5h creep at 760°C-840MPa.

Several parameters that control the Orowan by-passing of γ' particles, such as the size of the particles and to a smaller extent the amplitude of the lattice misfit, were investigated to explain the differences observed between the two superalloys [6]. The outcome of these investigations is that the mobility of perfect matrix dislocations is reduced in the case of MC-NG compared to the AM1 superalloy. This is mainly due to a small particle size, resulting in a small matrix channel width and thus a high Orowan stress, enhanced by the presence of Ru in the MC-NG. The consequences of the solid solution hardening are the existence of an incubation period and the enhancement of γ' particles' shear, instead of Orowan by-passing. Nevertheless, the deformation can be more homogeneous in the MC-NG if the precipitate size is increased through a preliminary ageing treatment. The optimum precipitate size is then 480nm [6].

I.3.2 Creep behaviour in the high temperature range (T>850°C)

The high temperature creep behaviour of single crystal Ni based superalloys is strongly correlated to the directional coarsening of γ' precipitates. The microstructure evolve from a periodic arrangement of γ' cuboidal particles to a lamellar structure, as shown in Figure 1.16. This morphological evolution is also called rafting. The orientation of the lamellar structure was shown to be strongly dependent on the sign of the applied stress and of the lattice parameter mismatch [64, 65]. Moreover, the rafting phenomenon is of crucial importance to explain the high temperature mechanical properties of superalloys. As seen in Figure 1.17, a high temperature creep curve can be decomposed into three stages:

- a primary creep stage, that may be preceded by an incubation period. It is characterized by fast work hardening and low macroscopic deformation.

- a secondary creep stage, during which the deformation rate remains constant.

- a tertiary creep stage, where the deformation rate increases, leading to the rupture of the specimen. This sudden increase is attributed to the shear of the γ' particles

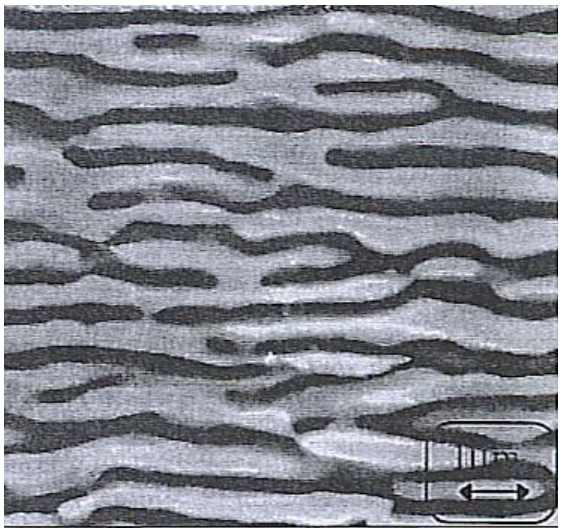

Figure 1.16: γ/γ' lamellar microstructure obtained in AM1 (white γ, black γ')

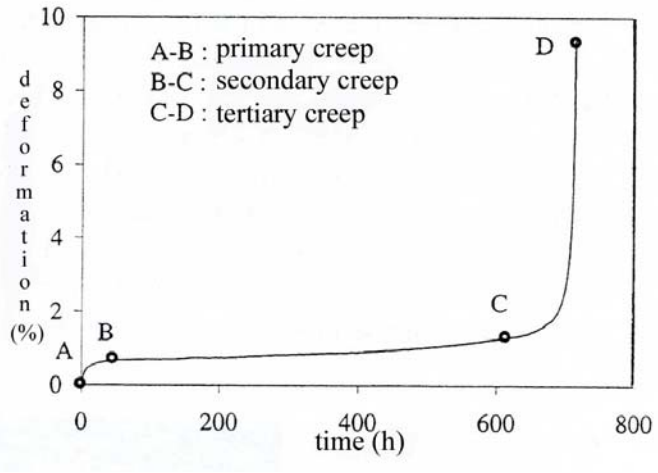

Figure 1.17: Typical high temperature creep curve for Ni based single crystals superalloys

Primary creep

Beyond 1000°C, the primary creep corresponds to the γ' precipitate morphology transition from cuboids to rafts or lamellar structure. During a tensile creep test and for a negative lattice parameter mismatch, the γ' rafts form perpendicularly to the

elongation axis, while they are parallel for a compression creep test. The opposite trends are observed when the lattice parameter mismatch is positive [66].

During the early stages of deformation, perfect matrix dislocations propagate in the γ corridors. As they glide on the {111} planes, the dislocation displacement involves planar glide and cross slips. The superimposition of the coherency stress field and applied stress result in an asymmetric internal stress field. Under the effect of this internal stress field, the propagation of dislocations is enhanced in the channels perpendicular (parallel) to the applied stress in the case of a negative (positive) lattice parameter misfit. In these channels, the coherency stress field is relaxed, while it increases in the others. This asymmetric behaviour is believed to be at the origin of rafting in superalloys [67]. When the microstructure is lamellar, the matrix dislocations lying on the γ/γ' interfaces interact with one another and form a network structure.

Secondary creep

The secondary creep stage is associated with a constant creep rate. The lamellar microstructure that was formed during primary creep is now well established. The γ' rafts act as an obstacle to matrix dislocations, which have to by-pass the precipitates. As the deformation rate remains constant, the density of mobile dislocations is constant. The structure of the interfacial dislocation network that formed during the primary creep stage becomes slowly denser as creep proceeds. Moreover, a localized rearrangement of interfacial dislocations occurs, as schematically shown in Figure 1.18 [1]. This network structure exhibits a very high stability during the secondary creep stage.

On the other hand, although the lamellar microstructure is well established, there is a competition between Ostwald ripening and directional coarsening of the precipitate phase. At the beginning of the secondary creep stage, the thickness of a γ' raft corresponds to the initial precipitate size. A model was proposed by Chen et al. to estimate the thickness variation of a γ' raft during the secondary creep stage [68]. They concluded that for small initial γ' precipitate size, the thickness of the raft must

increase, as the kinetics of ripening is faster than that of coalescence. In the case of average precipitate size (around 500 nm); both phenomena are in equilibrium, thus leading to a constant precipitate thickness. Directional coarsening prevails over Ostwald ripening when the initial precipitate size is large. This model is in agreement with experimental observations [69].

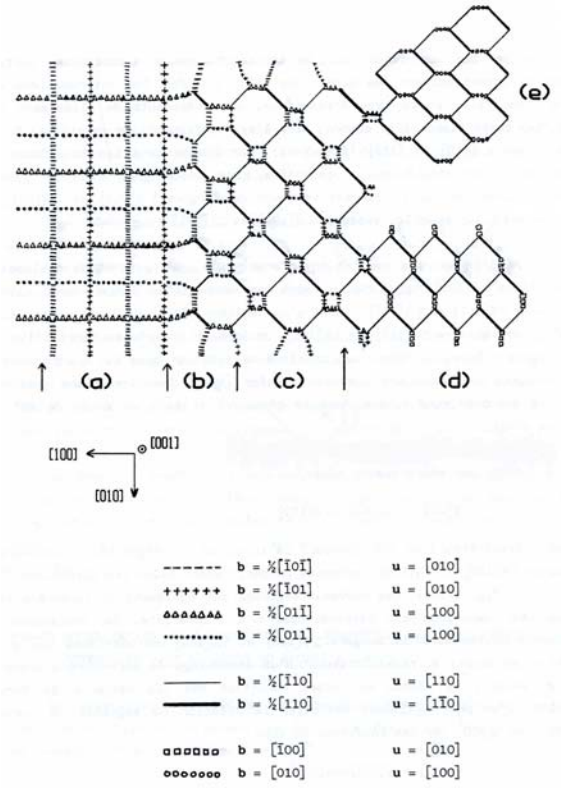

Figure 1.18: Mechanisms involved in the γ/γ' interfacial dislocation network formation, as from [1]. b is the Burgers vector and u the direction of the dislocation line.

Another parameter describing the microstructure, *i.e.* the topology, should be taken into account. In the initial microstructure, γ' is the enveloped phase and the γ matrix is the enveloping phase. Several authors have linked the transition from secondary to tertiary creep stage with a topological inversion, *i.e.* the γ' phase becomes the enveloping phase [1, 70]. This is explained by the formation of junctions connecting neighbouring γ' rafts and separating the γ phase. The dislocation network structure provides fast diffusion paths for the formation of this junction [70]. Moreover, recent studies have shown that this phenomenon occurs if the γ' volume fraction exceeds 50% at the temperature of the creep test [71].

Tertiary creep

During the tertiary creep stage, two mechanisms are identified to explain the sudden increase in deformation rate. On the one hand, the high increase in density of mobile dislocations and its correlation with the topological inversion that deteriorates the microstructure can explain the increase in deformation rate. At this stage, deformation mainly occurs through shear of the γ' phase. On the other hand, extrinsic parameters such as corrosion, oxidation, pores coalescence and crack propagation, which occur in the final stages of creep, can explain the damage of the material.

I.3.3 Comparison between the AM1 and MC-NG superalloys

As it can be seen on Figure 1.19, the high temperature creep behaviours of the AM1 and MC-NG superalloys are very different. In the MC-NG, there is an incubation period preceding the primary creep, which is attributed to the difficult motion of dislocations in the matrix (see section I.3.1). Moreover, the lamellar microstructure appears after a longer creep time in the case of MC-NG (around 100h) than in AM1 (around 20h). The presence of an incubation period can partially explain the delay in rafting. Nevertheless, the effect of refractory elements such as Re and Ru on atomic diffusion phenomena involved in directional coarsening must also be taken into account. As pointed out earlier, this needs however to be quantified. Moreover, at equivalent sample thermal history, the presence of Re leads to a smaller precipitate size and therefore to a smaller width of the γ channels, that will inhibit the plasticity.

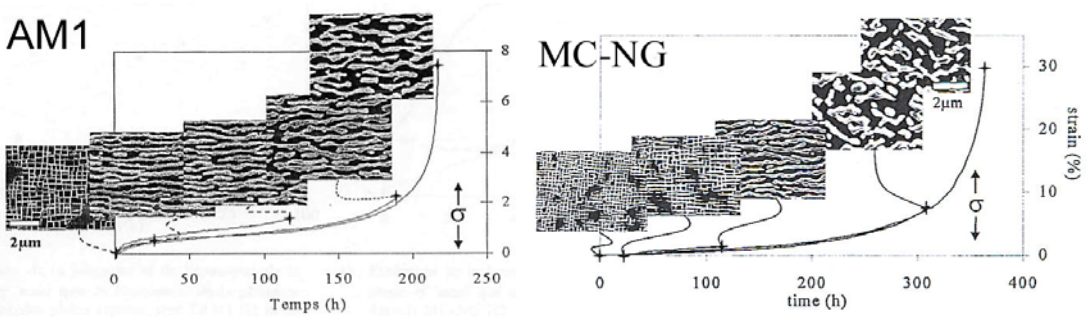

Fig.1.19: The creep behaviour (1050°C 150MPa) and the corresponding microstructure evolution of the AM1 and MC-NG alloys, as from [6].

Scanning electron microscopy observations have led to the conclusion that the γ/γ' lamellar microstructure is much more irregular and therefore less stable in MC-NG than in AM1. The relatively early onset of the tertiary creep stage in MC-NG, where shear of the γ' phase occurs, is attributed to this microstructure irregularity [6]. The presence of refractory elements in the alloy composition is believed to be at the origin of the deceleration of diffusion processes, such as directional coarsening of the γ' phase, ripening of the γ/γ' lamellar microstructure and climb of dislocations [6].

I.4 Strain induced rafting of γ' particles

Strain induced rafting of γ' particles was first reported by Véron et al. [7]. These authors have reported that if a sample is deformed, the anisotropic relaxation of internal stresses brought about by plastic deformation leads to directional coarsening of the γ' particles during a subsequent high temperature annealing without any applied stress. They deformed an AM1 sample in compression through a Vickers indentation. This sample was then annealed at 1050°C for 15 hours. The typical resulting microstructure is shown in Figure 1.20. The γ/γ' lamellar microstructure is developed around the indentation along the stress direction.

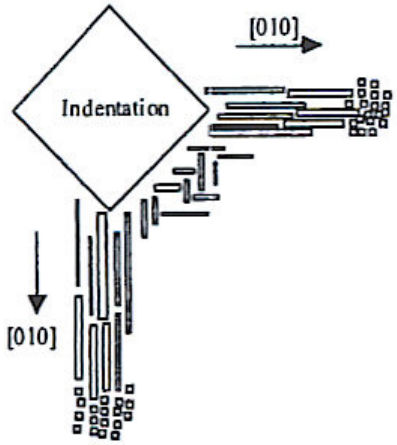

Figure 1.20: Schematic representation of the microstructure around the indentation, as from [7].

A dislocation based criterion was proposed to predict the orientation of the lamellar microstructure obtained during high temperature annealing of a pre-deformed sample [72]. Under the effect of the coherency stress field, dislocations will preferentially propagate in some particular γ channels during pre-deformation. The further relaxation of internal stresses during high temperature annealing will induce atomic diffusion under stress, leading to a lamellar microstructure with a specific orientation. In alloys with a negative lattice parameter misfit, the dislocations created during tensile deformation will preferentially propagate in the horizontal channels and thus will cover the 001 γ/γ' interfaces, where they relax coherency stresses. During high temperature annealing, the disappearance of the high energy interfaces, *i.e.* those less populated in dislocations; leads to the appearance of a lamellar microstructure perpendicular to the stress axis, as shown on Figure 1.21. This directional coarsening is often called of type N. The same scenario occurs for an alloy with a positive lattice misfit under compressive stress. In the case of a positive lattice parameter mismatch, dislocations brought about by tensile deformation will preferentially propagate in the vertical channels, leading to the formation of a lamellar microstructure parallel to the stress axis during further annealing. This corresponds to the type P. An equivalent microstructure is obtained if the lattice parameter mismatch is negative and the pre-deformation was of compression type. The same trends are observed in directional coarsening occurring under the presence of an applied stress [61].

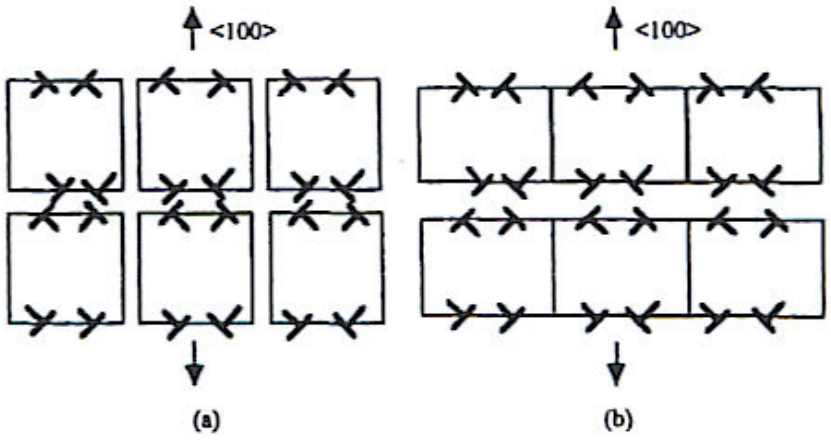

Figure 1.21: Dislocations mechanisms for directional coarsening. (a) Dislocations on interfaces perpendicular to the stress axis relax the coherency stresses in horizontal channels, then the microstructure evolves to form rafts as shown in (b) after high energy interfaces have disappeared.

The model described above does not enable to quantitatively describe the influence of the magnitude of both plastic strain and lattice parameter misfit on the strain induced directional coarsening of the γ' particles. Moreover, the mechanisms involved need to be identified.

In the present work, we will investigate the microstructure evolution as well as the kinetics of strain induced rafting of the γ' precipitates by means of small angle neutron scattering (SANS). Such experiments will also cast light on the role played by heavy refractory elements such as Re and Ru on the diffusion processes. On the other hand, the lattice parameter mismatch evolution during strain induced rafting of the γ' precipitates will be investigated by means of high resolution synchrotron diffraction from which will be deduced the influence of both plastic strain and coherency strain on this phenomenon. These results will be completed by electron microscopy observations so as to quantify the morphology evolution of the precipitates and the dislocations mechanisms associated to rafting of the γ' precipitates. To conclude, the role of precipitation misfit strain and plastic strain is examined using an inclusion theory of anisotropic elasticity.

CHAPTER 2 Experimental techniques

In this section we describe the experimental techniques used in this work. After an introduction to the basics of these techniques, a brief discussion of the peculiar experimental conditions necessary to investigate the case of single crystal nickel based superalloys is conducted.

II.1 Electron Microscopy

II.1.1 Scanning electron microscopy

Electron microscopy uses the interactions between an electron beam and the investigated sample to build an image. The electron beam is usually produced using a tungsten tip, and is accelerated towards the sample by an electric field. As electrons are charged particles, electromagnets are used as focusing lenses. There are different types of interaction between the incident electrons and the specimen, as shown on Figure 2.1.

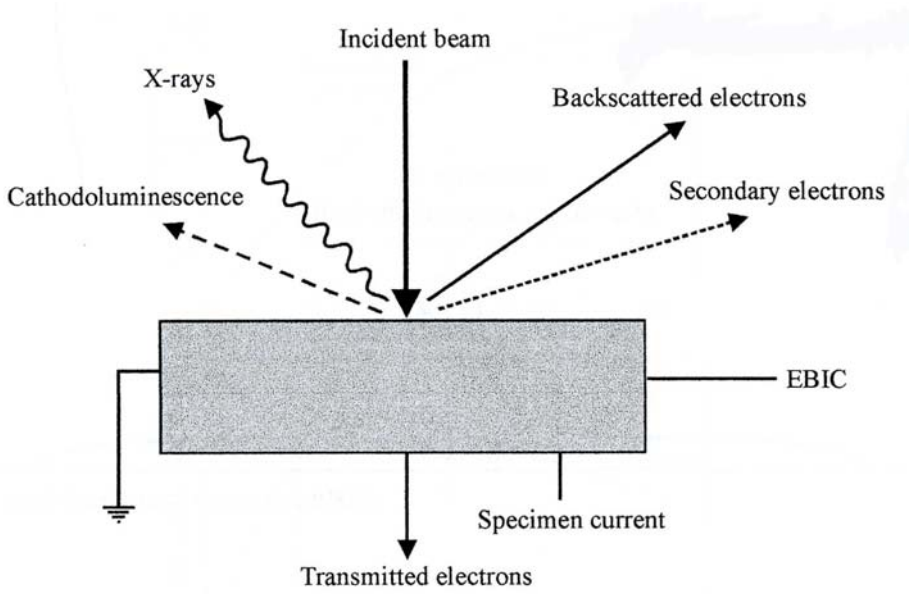

Figure 2.1: Types of interactions between an electron beam and a specimen

Secondary electrons escape from the conduction band of the specimen, as a result of interactions between charged particles. Their mean free path is of the order of a few nanometres in metals. Secondary electrons are therefore generated at the very surface of the material. On the other hand, backscattered electrons are the electrons coming out of the sample without energy loss by the interaction with the nuclei of the atoms constituting the specimen. Incident electrons are deviated from their initial trajectory by the positively charged nuclei and come out of the sample. They are therefore strongly dependent on the atomic number of the irradiated material and provide a source of contrast. Moreover, an incident electron can eject a K-shell electron from the electronic cloud of heavy atoms, thus inducing a fall of electrons from a higher energy shell into the K-shell. This phenomenon is accompanied by X-ray emission. This principle is used in atomic probe spectroscopy to identify the atomic species in the sample. Figure 2.2 shows the typical pear shape of the volume probed by the electron beam and the localization of the different type of interactions when an incident electron beam hits the surface of the specimen.

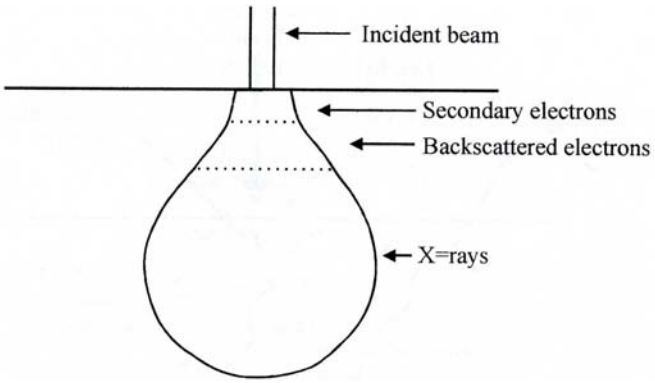

Figure 2.2: Probed volume in an electron microscope

Scanning electron microscopy (SEM) uses secondary and backscattered electrons to build an image. The surface of the specimen emits secondary and backscattered electrons that provide a signal at a given point, whose amplitude depends on the irradiated atomic species. This signal is converted to light by a scintillator detector and multiplied by a photomultiplier. This process is repeated at different sample positions (scanning) so as to finally form an image of a large sample area. Figure 2.3 shows a typical SEM setup.

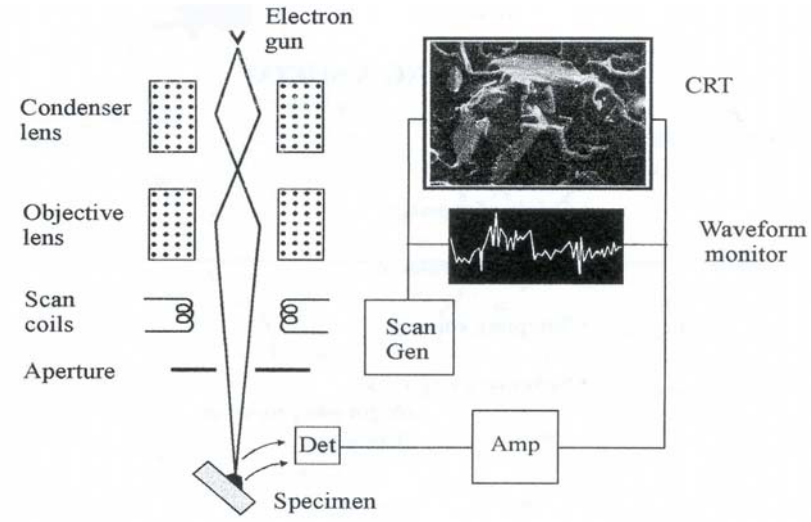

Figure 2.3: Typical SEM setup

Sample preparation is generally required to provide a contrast between the different phases. In this work, small samples were cut from a tensile specimen using electro spark erosion. The specimens were then mechanically polished with a slurry with a granulometry of 0.05µm. We then considered two types of etching. The first method was electro-chemical etching in a reactive solution constituted with 45% H_2SO_4, 42% HNO_3 and 13% H_3PO_4 under a voltage of 6V for around 30 seconds. This method preferentially dissolves the γ matrix. In the second case, the reactive product consists of a mixture of 60% HCl, 15% CH_3COOH, 15% HNO_3 and 10% H_2O. Samples were etched in it for around 10 seconds. This solution etches preferentially the γ' phase.

II.1.2 Transmission electron microscopy

In transmission electron microscopy (TEM), the contrast in crystalline materials arises mostly from diffraction rather than absorption, although the transmitted intensity depends on the nature of the specimen. The wave character of the electron beam is used. The TEM optical column may be split into five sections:

1. the electron gun and accelerator that produces the electrons
2. the condenser lenses that focuses the electrons as a beam or a spot on the specimen

3. the image forming system that focuses the electrons transmitted and diffracted by the specimen to form the primary image
4. the projector lens system that magnifies the image
5. the phosphor screen that is the acquisition system used to record the image

In modern transmission electron microscopes, the specimen is mounted on a platform that can tilt around two axes so as to modify the diffracting planes in the crystal. Moreover, an aperture placed below the specimen allows the selection of a particular diffraction vector $\vec{g}$. Figure 2.4 shows the mechanisms associated with the formation of an image using transmitted and diffracted electrons.

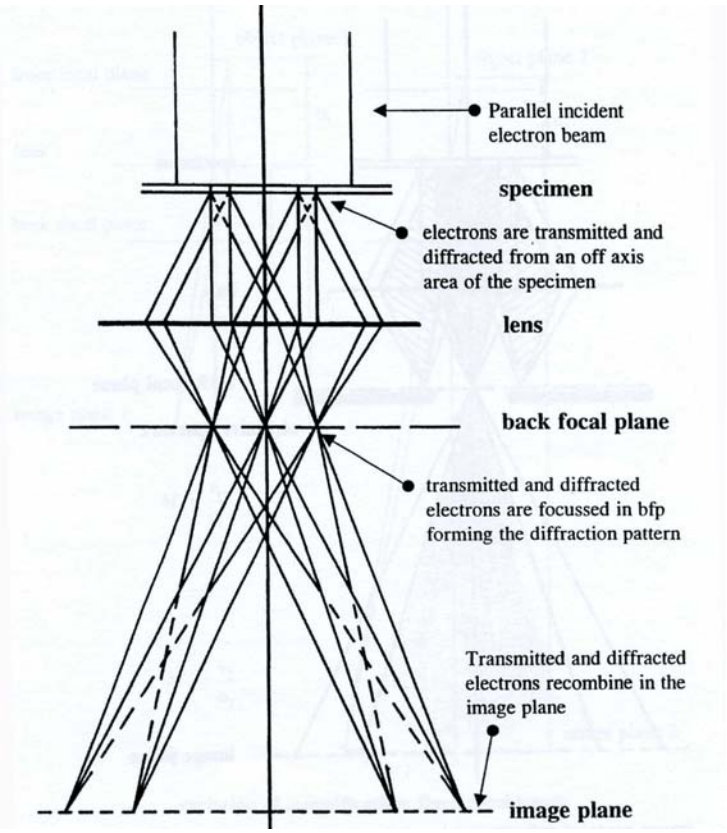

Figure 2.4: Image formation by combination of transmitted and diffracted electrons

In the present work, we have used the TEM technique for the observation of dislocation structures. Indeed, dislocations are only visible if the set of planes that are strongly diffracting are distorted by the presence of the dislocation, and this visibility criterion, in parallel with a series of images taken under carefully selected diffraction

conditions, can be used to determine the Burgers vector $\vec{b}$ of the dislocation. The visibility criterion is

$$\vec{g} \cdot \vec{b} \neq 0 \quad (2.1)$$

The determination of the Burgers vector of an observed dislocation therefore necessitates the observation of the same area of the sample with at least three carefully selected diffraction conditions. In the case of fcc lattice, the usually activated slip systems are of {111} <110> type. In order to identify the Burgers vectors of the observed dislocations, reflections of type 111, 200 and 220 are investigated.

As nickel superalloys contain elements having a large atomic number, TEM samples have to be prepared as thin as possible so that the electron beam is not fully absorbed through the specimen. In our case, focus is made on the observation of the dislocation network structure developing at the γ/γ' interfaces. Thin samples were therefore cut normal to the [001] crystallographic axis and subsequently mechanically polished on both sides with 1µm slurry until the final sample thickness reached around 70µm. Finally, very thin samples (around 50µm thickness) were obtained by ion beam sputtering.

II.2 Small-angle neutron scattering

Small-angle neutron scattering (SANS) has found many applications in materials science, from the observation of structural evolution in industrial alloys to fundamentals investigations of phase separation. Moreover, compared to SEM technique, SANS is non destructive and provides bulk information on a larger volume. The results are averaged on a large number of inhomogeneities, with good statistics, and are related to the Fourier transform of the shape and of the spatial arrangement of the inhomogeneities present in the material investigated. As different object populations can, in some cases, give the same SANS signal, the main drawback of the SANS technique is that it necessitates the formulation of hypotheses regarding the shape of the objects. Such information can be easily obtained through

SEM observations. Therefore, SANS and SEM are complementary techniques. The use of these two techniques on single crystal nickel based superalloys provides information about the morphology and the spatial arrangement of the γ' precipitates in the γ matrix. Moreover, it enables to follow *in-situ* the kinetics associated to microstructure evolution, such as directional coarsening of γ' particles during a high temperature annealing or a creep test. For further details, please refer to [73, 74].

II.2.1 Principles of Small-Angle Neutron Scattering

The SANS technique gives access to structures, whose dimensions are in the nanometre-micrometer range. The SANS signal arises from the difference in scattering length density $\Delta\rho$ between the inhomogeneities and their environment. The geometry of the measurement is schematically shown on Figure 2.5a). In the case of superalloys, the γ' particles have a different chemical composition from the γ matrix, thus providing different scattering length density (SLD) values, and therefore a SLD contrast. The contrast in terms of scattering length density in this two-phase system is calculated according to the following equation

$$\Delta\rho = \left|\rho^P - \rho^M\right| \quad (2.2)$$

In this simple case, the system consists in a set of inhomogeneities (precipitates, voids…) with homogeneous scattering length density ρ^P embedded in a matrix with homogeneous scattering length density ρ^M . The scattering length density is calculated as follows:

$$\rho = n_c \sum_{i=1}^{N} \frac{x_i b_i}{V_c} \quad (2.3)$$

where V_c is the unit cell volume, n_c the number of fundamentals units (atoms or molecules) in the unit cell, b_i .the coherent neutron scattering length of the atom i and x_i the fraction of the atom i in the unit cell. Using equation (2.3) and the data from Table 1.2, the contrast in terms of SLD between the γ matrix and the γ' precipitates for the MC-NG superalloy was calculated to be $\Delta\rho = 5.54E-7$ Å^{-2} at 1050°C to account for partial γ' dissolution. Detailed calculation is shown in Appendix A.

The scattering cross section per unit volume can then be written as

$$\frac{d\Sigma}{d\Omega}(\vec{q}) = \frac{1}{V}\Delta\rho^2 \left| \int_{V_p} \exp(i\vec{q}\cdot\vec{r}) d\vec{r} \right|^2 = \frac{1}{V}\Delta\rho^2 \left| F(\vec{q}) \right|^2 \qquad (2.4)$$

where V is the irradiated volume in the sample, $\vec{q}$ the scattering vector, whose definition is given in Figure 2.5b) and V_p the volume occupied by the particles. The modulus of the scattering vector is

$$\left|\vec{q}\right| = \frac{4\pi \sin\theta}{\lambda} \quad (2.4)$$

where λ is the incident neutron wavelength and 2θ the scattering angle. The function $F(\vec{q})$ is the form factor of the particle (see section II.2.3 for more details).

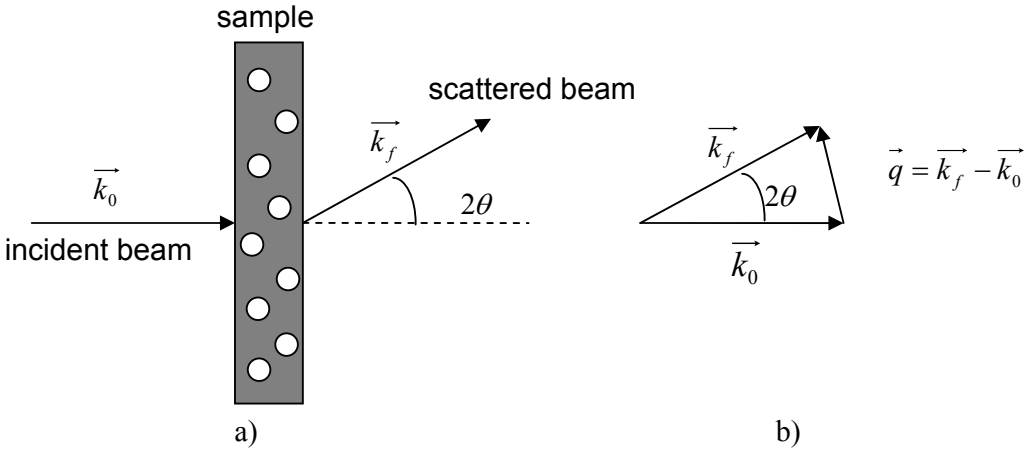

Figure 2.5: a) Geometry of a SANS experiment, b) Definition of the scattering vector

II.2.2 Experimental setup

In this work, two types of experimental setup for SANS investigations have been used. The SANS experiments were performed on the beamlines, D11 at the Institut Laue Langevin (ILL, Grenoble, France), V4 at the Berlin Neutron Scattering Centre in the Hahn Meitner Institut (HMI, Berlin, Germany) and DN-2 at the Nuclear Physics Institute (NPI, Řež- Czech Republic). The first two have a pinhole camera geometry, as shown in Figure 2.6. It typically consists in a mechanical velocity selector that selects neutrons at a given energy so as to obtain a pseudo-monochromatic beam.

The wavelength dispersion is usually around $\frac{\Delta\lambda}{\lambda} = 10\%$. The beam is then collimated by apertures in order to reduce the angular divergence of the incident beam. The length of the collimation zone is adjustable and usually varies between 3 and 38m. The intensity scattered by the sample is then collected by a 64*64 cm^2 ^{3}He detector made with usually 1cm^2 pixels. A beamstop is placed on the detector to mask the incident beam and to avoid detector saturation. The sample-to-detector distance can be varied to modify the observed q-range. The further the detector, the lower the q values (see Eq 2.4). The q-range that can be investigated with this setup depends on the instrument geometry and is in the best case 10^{-3} – 0.5$Å^{-1}$ (D11-ILL). The whole collimation zone and the space between the sample and the detector are under primary vacuum to avoid neutron absorption and scattering from the air.

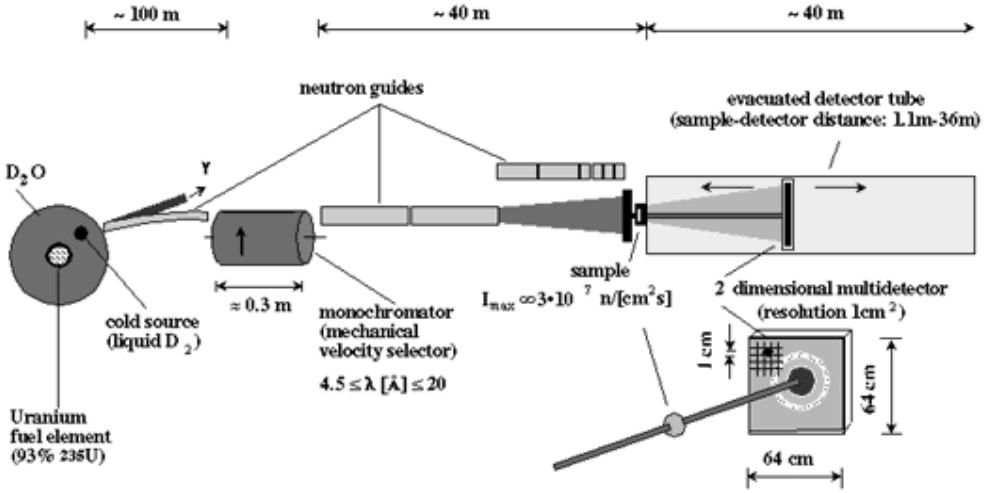

Figure 2.6: Layout of the D11 pinhole camera at the ILL

Another type of setup was used at the NPI. The double crystal SANS diffractometer DN-2 is designed for the measurements of small-angle neutron scattering at high q-resolution in the low q-range. The setup is shown on Figure 2.7. A bent Si 111 crystal is used to select the incident neutron wavelength. The monochromatic beam hits the sample and the scattered beam is again diffracted by a bent Si 111 analyser crystal asymmetrically cut. The fully asymmetric diffraction geometry on the elastically bent Si analyser is employed to transfer the angular distribution of the scattered neutrons to the spatial distribution and to analyse the whole scattering curve by a one dimensional position sensitive detector. The remote

control of the curvatures of both monochromator and analyser crystals enable to tune the instrument resolution in the δq range from 10^{-4} to 10^{-3} Å^{-1}. The q-range investigated in this setup varies between $2*10^{-4}$ – $2*10^{-2}$ Å^{-1}.

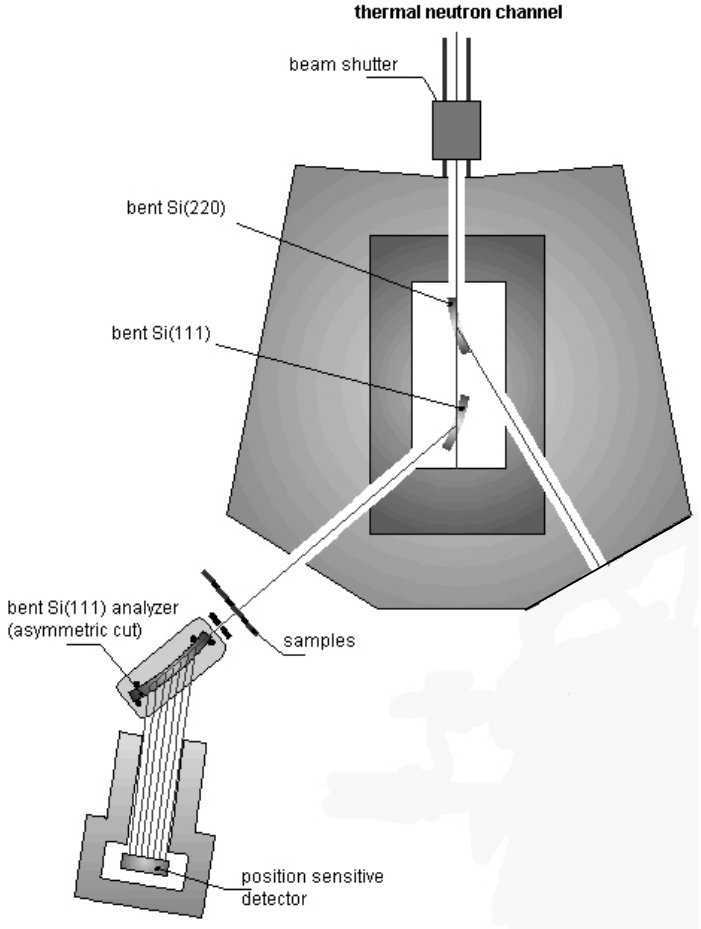

Figure 2.7: Double crystal SANS diffractometer setup

II.2.3 From intensity to microstructure

The macroscopic scattering from a set of particles is the result of the interaction of all scattered signals from each single particle and can be decomposed in the product of two specific functions:

$$I(\vec{q}) \approx \Delta\rho^2 N_P V_P^2 \left\langle \left| F(\vec{q}) \right|^2 \right\rangle S(\vec{q}) \quad (2.5)$$

where N_p is the density in scattering elements and V_p the average volume of a particle. The two functions $\left\langle \left| F(\vec{q}) \right|^2 \right\rangle$ and $S(\vec{q})$ are the particle average form factor and structure factor respectively.

The form factor depends on the morphology of the particles, and is a function of the orientation of $\vec{q}$ if there is a strong orientation correlation between the particles. For instance, spherical particles give a isotropic SANS spectrum, as well as randomly oriented cuboidal particles. Equation (2.6) gives the form factor in the case of a spherical particle of radius R and the corresponding plot is given in Figure 2.8 [75].

$$F_{sph}(q,R) = 3\left[\frac{\sin(qR) - qR\cos(qR)}{(qR)^3}\right] \qquad (2.6)$$

We can see that if $\frac{qR}{2\pi} \approx \frac{(2k+1)}{4}$, $F_{sph}(q,R) = 0$; and if $\frac{qR}{2\pi} \approx \frac{k}{2}$, $F_{sph}(q,R)$ reaches its relative maxima ($k \in \mathrm{N}$).

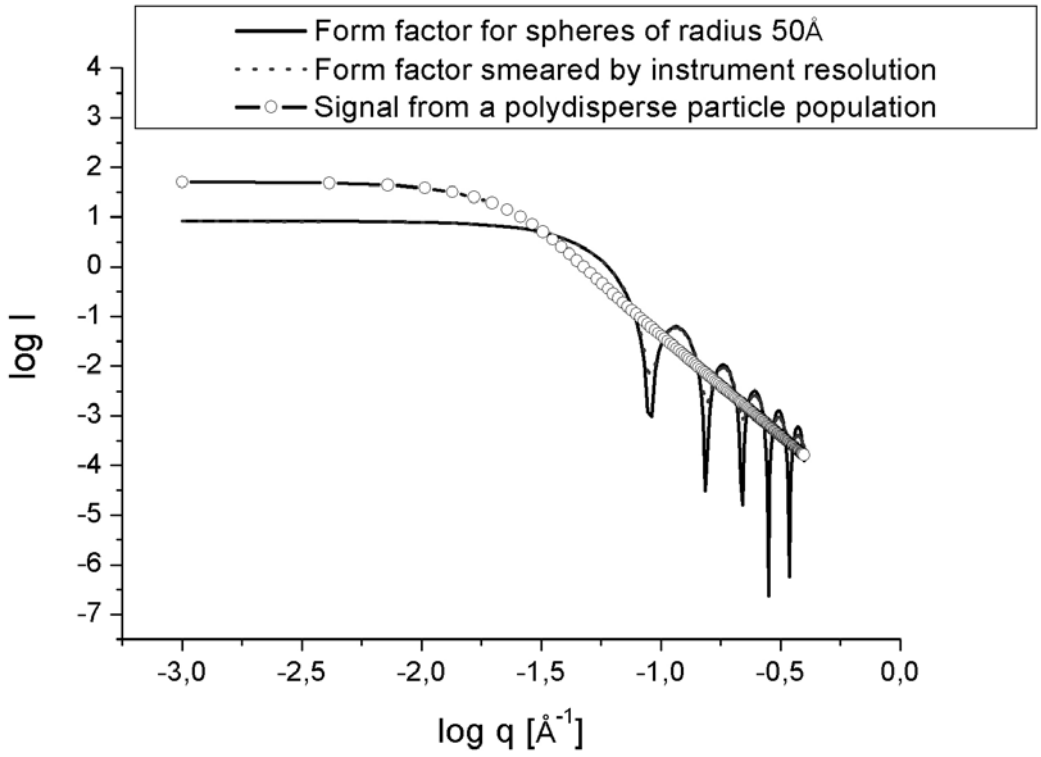

Figure 2.8: Form factor of a spherical particle of diameter 2R. The smearing induced by instrument resolution and particle size distribution is also shown.

In the case of polydisperse systems, *i.e.* when a particle size distribution $N(r)$ exists, the form factors from each single particle will be added to each other, leading to a smearing effect of the form factor oscillations obtained in the case of a dilute system constituted by monodisperse particles (see Figure 2.8). This has been simulated and is schematically shown on Figure 2.9. The average form factor in the case of a size distribution of spherical particle is then expressed as

$$\left\langle \left| F_{sph}(q) \right| \right\rangle = \int_0^\infty \left| F_{sph}(q,r) \right| N(r) dr \qquad (2.7)$$

The structure factor takes into account the interferences between the scattered signals by each single particle. In the case of dilute systems, the structure factor $S(\vec{q})$ is equal to unity. For a set of particles, it is generally expressed as:

$$S(\vec{q}) = 1 + N_p \int_V (g(\vec{r}) - 1) \frac{\sin(\vec{q}.\vec{r})}{\vec{q}.\vec{r}} 4\pi r^2 d\vec{r} \qquad (2.8)$$

where N_p is the particles density, and $g(\vec{r})$ the pair function distribution. The latter gives the probability to find a particle at the distance r from a particle located at $\vec{r} = \vec{0}$. In little cases, equation (2.6) can be formulated by an analytical expression. However, in strongly correlated systems such as nickel based single crystal superalloys with a high particle volume fraction, the regular arrangement of the cuboidal precipitates will lead to the appearance of several maxima or correlation peaks in the scattering curve. This is shown if Figure 2.9c. If the particles are regularly separated by a distance L along the {100} crystallographic axes, a correlation peak is visible in the scattering curves averaged along {100} at the following position:

$$q^* = n \frac{2\pi}{L} \qquad (2.9)$$

Where $n \in Z$ is the order of the interference peak. Depending on the regularity of the spatial arrangement of the cuboidal particles, the correlation peaks may be smeared and it is quite common to observe only the first order correlation peak ($n = 1$).

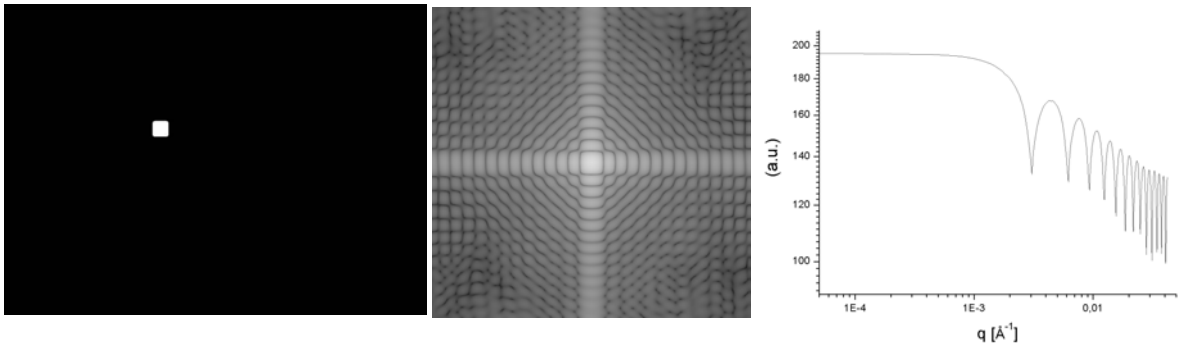

a) dilute cuboidal particle (size of the edge=100nm)

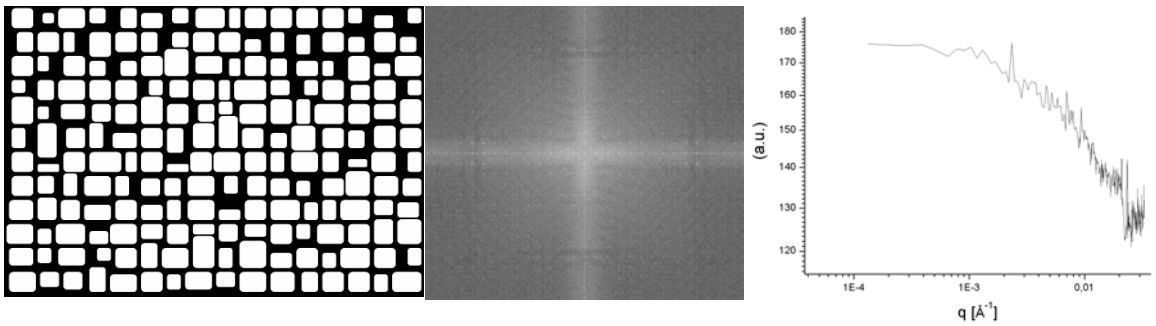

b) System of cuboidal particles with size distribution (mean size=100nm)

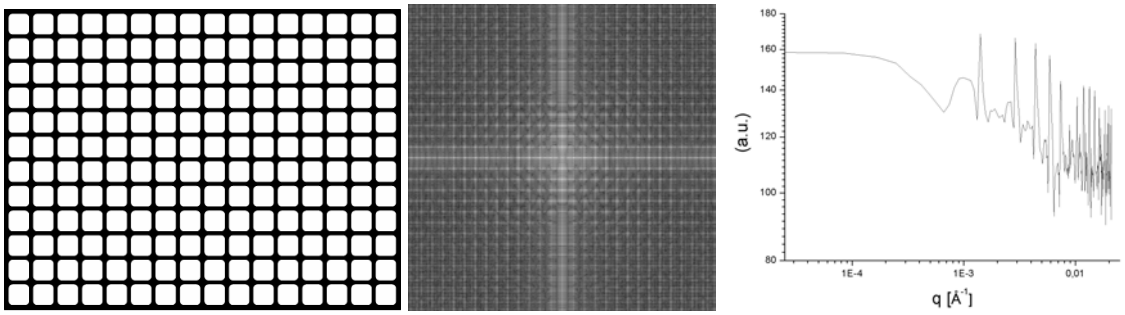

c) System of monodisperse cuboidal particles regularly arranged

Figure 2.9: Effects of a particle size distribution on the scattered intensity, left: image in the direct space, middle: Fourier transform, right: greyscale profile of the Fourier transform. b) Smearing of form factor oscillations associated to size distribution and c) the apparition of correlation peaks associated to a regular arrangement of particles are clearly visible.

II.2.4 Data Processing

Small-angle scattering data usually contain the background from the instrument and the scattering from sample environment $I_b(\vec{q})$ in addition to the scattering from

the specimen itself $I_s(\vec{q})$. Therefore, a measurement of $I_b(\vec{q})$ performed during the acquisition of the scattering from the empty cell or empty furnace has to be carried out for background subtraction. Moreover, the transmissions of both sample T_s and sample environment T_b have to be precisely measured and taken into account for this subtraction if the absolute scattered intensity is to be considered and different samples have to be compared. The detector efficiency can be determined by the measurement of the intensity I_w incoherently scattered by a reference element such as water or graphite. Such elements scatter the neutrons incoherently and porvide a isotropic and flat intensity. This measurement is also used to scale the scattering from the sample, assuming that the scattering cross section $\frac{d\Sigma}{d\Omega_w}(\lambda)$ of the reference sample is known. For consistency reasons, the reference measurement I_w also has to be corrected for background subtraction I_{EC} (empty cell) as well as water and empty cell transmissions T_w, T_{EC} respectively. In these conditions, the absolute scattered intensity is calculated using the following equation:

$$I(\vec{q}) = \frac{\left[\frac{I_s(\vec{q})}{M_s T_s} - \frac{I_b(\vec{q})}{M_b T_b}\right]\frac{1}{t_s}}{\left[\frac{I_w}{M_w T_w} - \frac{I_{EC}}{M_{EC} T_{EC}}\right]\frac{1}{t_w}} \cdot \frac{d\Sigma}{d\Omega}(w,\lambda) \quad (2.10)$$

where M_s, M_b, M_w, M_{EC} are the total monitor counts for sample, background, water and empty cell measurements. t_s and t_w are the respective thicknesses of sample and water cell respectively. This data processing is implemented in the software suit developed by R. E. Gosh [76] or the GRASP software developed by C. Dewhurst [77] for data recorded at the ILL. The BerSANS software [78] was used for data recorded in HMI. In all the software pack used, it is possible to average the scattered intensity along selected directions through the definition of angular sectors. An orientation dependent plot of $I(q)$ along certain crystallographic axes can be obtained in this way, assuming that the SANS signal is isotropic in the angular sector considered. This is shown in Figure 2.10.

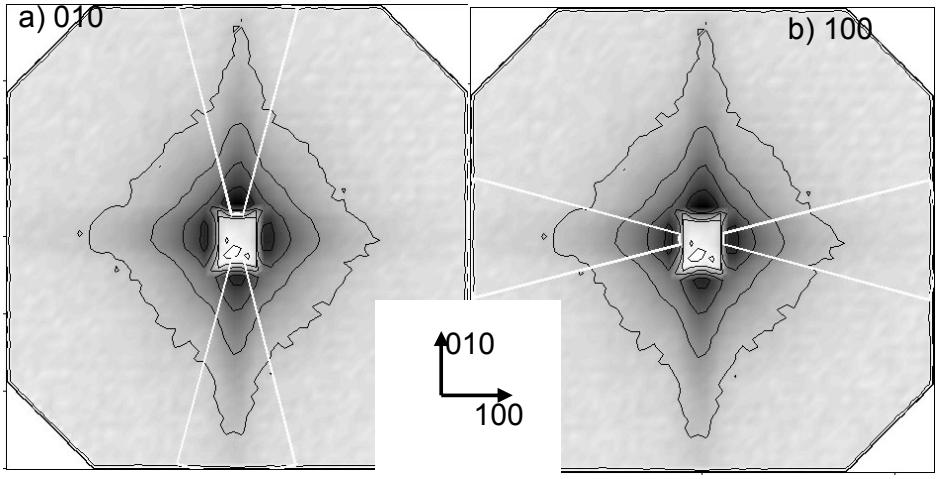

Figure 2.10: Averaging of the scattered intensity along some crystallographic directions using angular sectors

It is possible to extract quantitative information from the $I(q)$ curves. When two media, in our case matrix and particles phases, are separated by a sharp interface, the scattered intensity follows an asymptotic law in the large q region, *i.e.* when $q >> 2\pi / R$, where R is the mean particle size. This law is the Porod's approximation and is written under the following form

$$\lim_{q\to\infty} I(q) \propto 4\pi\Sigma(\Delta\rho)^2 q^{-4} \quad (2.10)$$

where Σ is the specific surface area of the investigated system. It corresponds to the total surface area per unit of bulk volume, accounting for textured surfaces, and is commonly expressed in $m^2.cm^{-3}$. Therefore the plot of $I(q).q^4$ versus q^4 results in a straight line in the large q-range, whose intercept with the vertical axis gives access to the determination of the specific area. An example of Porod plot is shown on Figure 2.11. When compare with the q-range classically measured on a standard pinhole camera (up to $0.5Å^{-1}$) with the typical particle size in nickel based superalloys (around 350nm), it appears that the Porod law is valid over a large q-range.

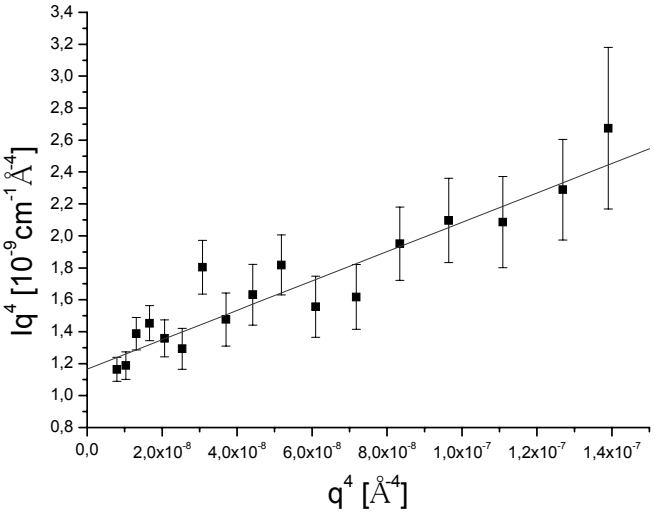

Figure 2.11 : Example of a Porod plot and linear fit associated

II.3 High resolution diffraction of high energy synchrotron radiation

In this work, high resolution diffraction of high energy synchrotron radiation is used to determine the lattice parameter mismatch between γ and γ' phases in nickel based superalloys. In this section, we briefly remind the principles of a diffraction experiment. After describing the high resolution setup used, the procedure for data analysis and lattice parameter mismatch determination is detailed.

II.3.1 Principles of the diffraction technique

Diffraction results from interferences between elastic scattering events occurring when a crystalline object is irradiated by a wave. An incident plane wave is scattered by a single atom as a spherical wave. The spherical waves scattered by many atoms interfere with each other in a constructive or destructive way. A diffraction peak is observed when the interferences are constructive, *i.e*. when the scattered waves are in phase. This is the peculiarity of diffraction by a lattice of atoms (see Figure 2.12). Crystalline planes are usually indexed using Miller's indexes (hkl). The geometric conditions for constructive interference to occur are given by the Bragg law

$$n\lambda = 2d_{hkl}\sin\theta \quad (2.11)$$

where λ is the monochromatic incident wavelength, d_{hkl} the distance between two (hkl) planes, and θ the diffraction angle.

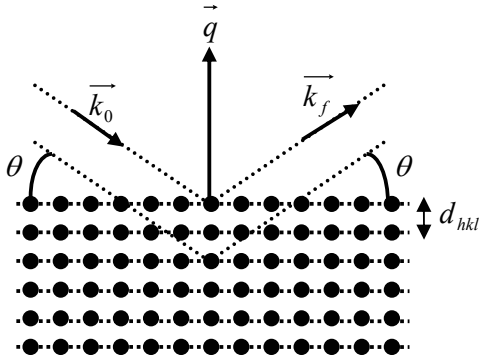

Figure 2.12: Schematic view of Bragg's law. $\overrightarrow{k_0}$ and $\overrightarrow{k_f}$ are the incident and diffracted wave vectors respectively. $\vec{q} = \overrightarrow{k_f} - \overrightarrow{k_0}$ is the scattering vector

In these conditions, the amplitude of the diffracted wave is proportional to

$$A(\vec{q}) = \sum_j f_j(\vec{q}).e^{i\vec{q}.\vec{r_j}} \qquad (2.12)$$

where $f_j(\vec{q})$ is the atomic form factor of the scattering atom at the position $\overrightarrow{r_j}$ in the unit cell over which j runs. The atomic form factor is equal to the Fourier transform of the electronic density in the case of X-ray diffraction and of neutron scattering lengths in the case of neutron diffraction.

A representation of diffraction in reciprocal space is commonly used. If $\vec{a},\vec{b},\vec{c}$ are the primitive vectors of a lattice unit cell, the position of an atom j can be expressed as $\overrightarrow{r_j} = x_j\vec{a} + y_j\vec{b} + z_j\vec{c}$. We can define $\overrightarrow{a^*} = 2\pi\frac{\vec{b}\times\vec{c}}{\vec{a}\cdot(\vec{b}\times\vec{c})}$, $\overrightarrow{b^*} = 2\pi\frac{\vec{c}\times\vec{a}}{\vec{a}\cdot(\vec{b}\times\vec{c})}$, $\overrightarrow{c^*} = 2\pi\frac{\vec{a}\times\vec{b}}{\vec{a}\cdot(\vec{b}\times\vec{c})}$ as the primitive vectors of the reciprocal space. The (h, k, l) reciprocal lattice point defined by the vector $\overrightarrow{G} = h\overrightarrow{a^*} + k\overrightarrow{b^*} + l\overrightarrow{c^*}$ is associated to the (hkl) plane in the direct space. With this representation, Bragg condition for diffraction to occur is equivalently written as $\vec{q} = \overrightarrow{G}$. Equation 2.12 can then be written as

$$A(\vec{q}) \propto \left|F_{hkl}\right|^2 \qquad (2.13)$$

where F_{hkl} is the structure factor and is defined as

$$F_{hkl} = \sum_n f_n \exp[-2i\pi\{hx_n + ky_n + lz_n\}] \qquad (2.14)$$

where the sum over n is the sum over the atoms constituting the primitive unit cell. For particular values of (hkl), the structure factor may be equal to zero, leading to the extinction of the reflection. In the case of a fcc unit cell constituted by four identical atoms, the atomic positions in the cubic cell are (0, 0, 0), (1/2, 1/2, 0), (1/2, 0, 1/2) and (0, 1/2, 1/2). The structure factor is then calculated to be

$$F_{hkl} = f\{1 + \exp[-i\pi(h+k)] + \exp[-i\pi(h+l)] + \exp[-i\pi(k+l)]\} \quad (2.15)$$

Such a structure factor differs from zero if h, k and l are either all odd or all even. However, if the unit cell contains atoms of different types with preferential site occupancy, as it is the case for Ni_3Al, the structure factor is never equal to zero. In such case, extra reflections appear, also called superlattice reflections.

II.3.2 Instrumental setup

As the lattice parameter mismatch defined in section I.2.4 in nickel based superalloys is usually small (around 10^{-3}), a high resolution setup is necessary if the γ and the γ' peaks are to be distinguished. The high resolution setup used consists in a triple crystal diffractometer (TCD) [79], whose representation is given on Figure 2.13. Experiments were carried out on the high energy beamline BW5 in HASYLAB (Hamburg - Germany). Measurements were performed using high energy synchrotron radiation (120keV) corresponding to a wavelength around 0.1Å. The monochromator at BW5 is a Si single crystal with a (311) orientation ($\theta_{Si} = 1.81^\circ$), which selects a particular wavelength from the white beam. The monochromatic beam is then diffracted by the sample (in our case $\theta \approx 1.62^\circ$ for the 200 or 002 reflection in nickel superalloys at room temperature), and the resulting intensity is measured by a Ge detector after a third reflection on the analyser crystal (Si single

crystal with a (311) orientation). The advantage of using the Si 311 reflection is that the d-spacing, and thus the diffraction angle, is close to that of single crystal nickel based superalloys (around 3.6 Å). In this (+,-,+) setup, the instrument contribution to the diffraction peak broadening is extremely small, compare to that of the sample.

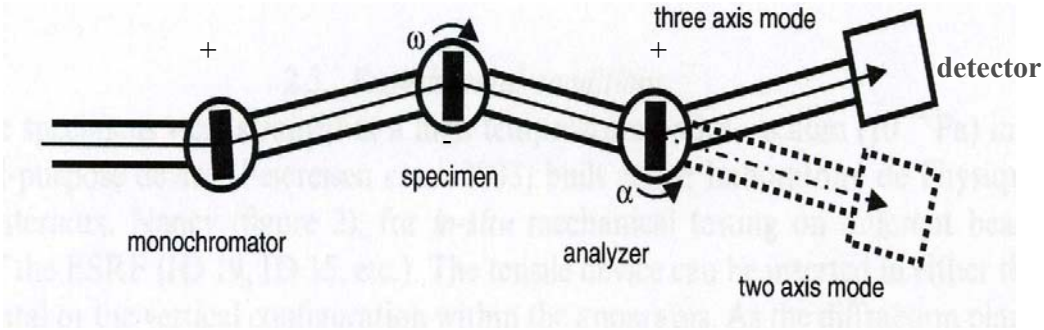

Figure 2.13: Triple crystal diffractometer: (+,-,+) setup

Due to the high energy of the radiation, Bragg angles are small and the scans in the reciprocal space are carried out almost perpendicular or parallel to the scattering vector, as shown in Figure 2.14. A transverse scan around the sample axis (perpendicular to the scattering vector $\vec{q}$) is performed by simple ω rotation. In this case, measurements are sensitive to the mosaicity of the sample. A longitudinal scan (almost) along $\vec{q}$ is performed by rotating the analyser (α scan). Measurements are then sensitive to the lattice parameter distribution. Therefore, in order to determine the lattice parameter mismatch between γ and γ' phases in nickel based superalloys, iso-intensity maps can easily be recorded by performing analyser scans at a fixed ω position. This process can be repeated at different ω, thus obtaining the variation of the mismatch in different sub-grains of the mosaic. The high resolution in the reciprocal space provided by this setup enables the determination of the lattice mismatch with an accuracy better than 10^{-4}.

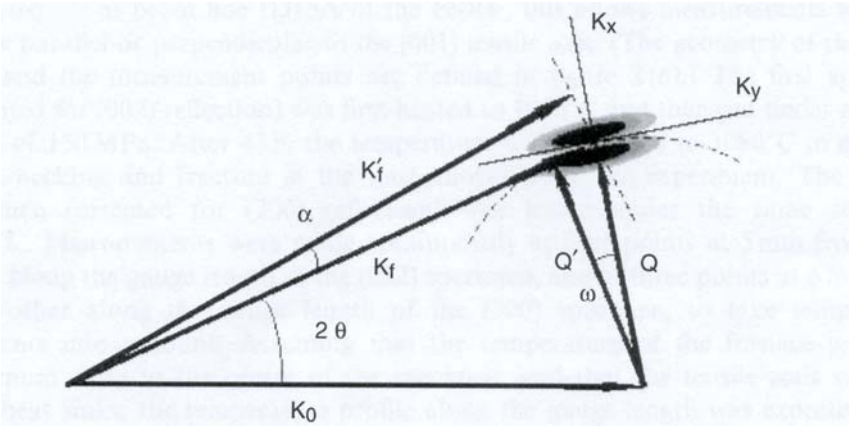

Figure 2.14: Reciprocal space representation of the scanning of a Bragg reflection. An ω rotation scans the mosaicity and an α scan gives the lattice parameter distribution

II.3.3 Data processing

When the microstructure consists in a periodic arrangement of cuboidal γ' particles, three contributions to the diffraction pattern around a 200, 020 or 002 reflection can be distinguished [80, 81]. These are shown in Figure 2.15. There is a sharp and intense γ' peak, corresponding to the contribution of the γ' phase. The matrix channels contribute to the diffraction pattern into two separate contributions. The γ channels perpendicular to the scattering vector $\vec{g}$ contribute in the total diffraction pattern in a narrow peak γI, whose position is not centred on that of the γ' peak. The distance $\Delta\alpha$ between the centres of the γ' peak and of the γI peak gives access to the determination of the measured lattice misfit δ^{3D}. Müller et al. [80, 81] have shown that the measured lattice parameter mismatch is related to the natural lattice parameter misfit δ defined in equation (1.7) using

$$\delta^{3D} = \frac{1+\upsilon}{1-\upsilon}\delta \approx 2.45\delta \quad (2.16)$$

where $\upsilon = 0.42$ is the Poisson's ratio. The other channels contribute in a wide peak γII which is almost centred on the γ' peak, these γ channels being stressed by the presence of the γ' phase .

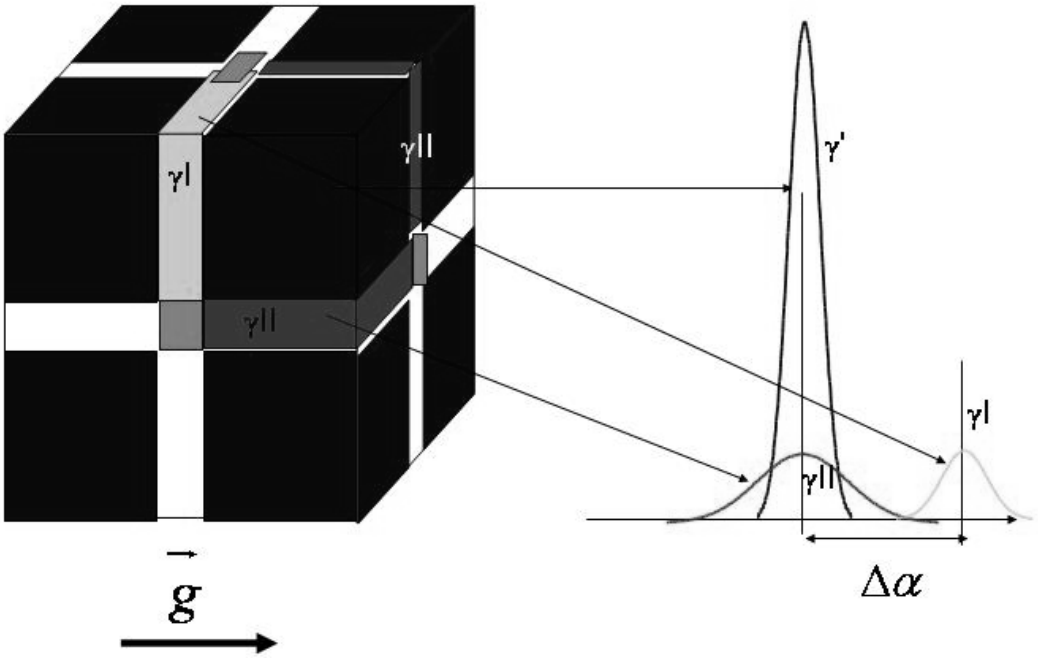

Figure 2.15: Relationship between microstructure and diffraction pattern

Figure 2.16 shows an example of a 200 reflection obtained in a nickel based superalloy with a rafted microstructure. The most striking features in this profile are the presence of two well defined peaks attributed to the contributions of γ and γ' phases, and a linear decrease of the tail intensity in logarithmic scale. In a rafted microstructure, the γ and γ' peaks are better separated than in a cuboidal microstructure, as different stress states coexist.

The data processing procedure consists in using three symmetrical peaks to fit the experimental data after background subtraction. In this particular case, the adjustment of the data is carried out using the following function, that fits well the linear tails observed in logarithmic scale [82]

$$P(x) = A\exp\left\{1-\left[1+\left(\frac{|x-x_0|}{w_\alpha}\right)^\alpha\right]^{\frac{1}{\alpha}}\right\} \qquad (2.17)$$

where A is the peak height, x_0 the peak centre, $1/w_\alpha$ the slope of the curve tails in log scale and $\alpha>1$ a parameter determining the peak sharpness. The peak parameters are adjusted using the least square method. We can see on Figure 2.16 that the main features are reproduced, including the tails of the peak (up to a few counts).

The most intense peak corresponds to the γ' contribution as this phase shows the highest volume fraction at temperatures below 1150°C in the MC-NG alloy. Two peaks are necessary to account for the γ matrix contribution. When the γ' particles develop as rafts perpendicular to the tensile axis, the sharpest and most intense (γ_I) peak is the contribution of the γ channels perpendicular to the tensile axis while a wide (γ_{II}) peak takes into account the contribution from the residual channels parallel to the tensile axis. In the latter, the stress state is supposed to be less homogeneous. This data processing procedure is well adapted for the case of a lamellar microstructure. The data extracted from this fitting procedure are the full-widths at half maximum (FWHM) of the two main peaks (γ') and (γ_I), the intensities of the two main peaks and the angular distance $\Delta\alpha_{hkl}$ between the maxima. The lattice parameter mismatch between γ and γ' phases is then determined using the following equation

$$\delta_{hkl} = \frac{\Delta\alpha_{hkl}}{2}\cot(\theta_{Si}) = \frac{2(a_{\gamma'} - a_{\gamma})}{a_{\gamma'} + a_{\gamma}} \qquad (2.18)$$

where θ_{Si} is the monochromator or analyser diffraction angle. The FWHM is determined using

$$FWHM = 2w_{\alpha}[(1+\ln 2)^{\alpha} - 1]^{1/\alpha} \qquad (2.19)$$

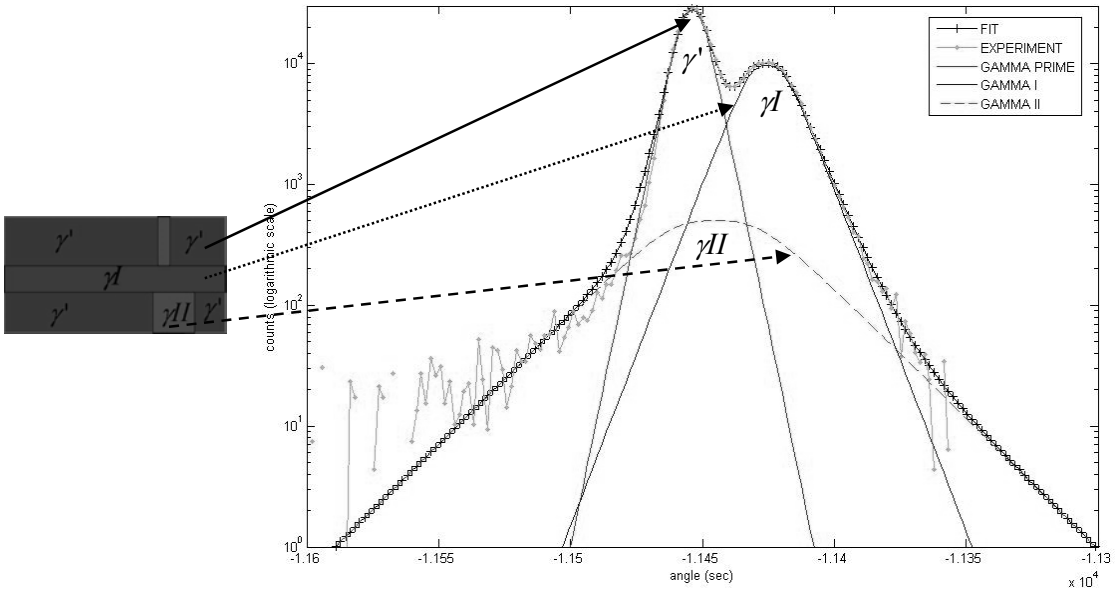

Figure 2.16: Typical 200 reflection in a rafted microstructure

In the case of deformed nickel based superalloys, distinction is made between the lattice parameter mismatch parallel and perpendicular to the deformation axis. As was discussed in Chapter1, the dislocations created by deformation will interact with the coherency stress field induced by the natural misfit strain, leading to an anisotropy in dislocation density. Therefore, at least two reflections have to be measured to fully characterize the lattice parameter mismatch. If the elongation axis is along [001], the 002 reflection will give access to the lattice parameter misfit parallel to the deformation axis defined as $\delta_{//}$. On the other hand, the 200 or 020 reflections give access to the lattice parameter mismatch perpendicular to the elongation axis and is defined as $\delta_{\perp}$.

II.4 Experimental investigations

Most of the experimental investigations carried out consist in the study of the rafting of γ' particles in nickel superalloys during isothermal annealing. The morphology change of the particles and the associated kinetics are investigated *in-situ* using the SANS technique. Prior to the experiment, MC-NG samples were deformed in tension at 850°C until the plastic deformation develops homogeneously. The acquisition of the SANS patterns during high temperature annealing of the deformed sample casts light on the kinetics of rafting and the possible influence of the alloy composition, particularly the content in refractory elements (Re-Ru). Direct microstructure observations by means of SEM confirm these results.

Complementarily, a similar experiment was conducted but using the high resolution diffraction of synchrotron radiation. The measurement of the lattice parameter mismatch evolution during rafting of γ' particles has enabled the determination of the micromechanics involved in the morphology change. These results are completed by TEM observations of the dislocation structures before and after the high temperature annealing during which rafting occurs. In all the investigations performed in large scale facilities, the beam size was large enough to analyse dendritic and interdenditric regions of the specimen.

CHAPTER 3 Presentation and discussion of the experimental results

In this chapter, the experimental results obtained using the techniques described in the previous section are shown. After a full characterization of the initial microstructure, the evolution of the specimen at each step of the strain induced rafting phenomenon is conducted. The kinetics of the microstructure evolution, the evolution of the lattice parameter mismatch during annealing and the evolution of the dislocation structure are discussed.

III.1 Investigation of the initial microstructure

Experiments are carried out on MC-NG samples provided by SNECMA. The specimens were subject to homogenisation heat treatment prior to each investigation. After homogenisation heat treatment, the MC-NG microstructure was analysed by SANS, completed by SEM observations. Diffraction measurements allowed the determination of the lattice parameter misfit between γ and γ' phases in the standard conditions of use of these materials, *i.e.* after homogenisation heat treatment.

III.1.1 SANS investigations of the initial microstructure

Two sets of SANS experiments were carried out to investigate the microstructure of the MC-NG superalloy after homogenisation heat treatment (1310°C-3h). The first set of experiments was carried out on D11 at the ILL and focused on the observation of the particle shape. The second experiment was performed on DN-2 at the NPL, which enables to observe the USANS (Ultra Small Angle Neutron Scattering) signal arising in the very low q-regime and check the occurrence of a correlation peak (see Chapter 2) that provides information about the spatial arrangement of particles [8].

✓ **The D11 experiment**

- Experimental procedure:

The neutron wavelength was chosen to be 12 Å so as to obtain the best compromise in terms of incident flux and investigated q-range. The sample to detector distance was fixed at 4m. In this q-range, corresponding to the Porod regime, the microstructure was investigated in terms of particle shape and specific area. The sample was rotated around the [010] axis (ω), as schematically shown in Figure 3.1. The position $\omega = 0°$ corresponds to the neutron beam aligned with the [001] crystallographic axis of the sample. The acquisition of the SANS pattern at successive ω positions provides information about the γ/γ' interface sharpness, as SANS measurements are sensitive to the specific area. As the shape of γ' particles is expected to be of cubic symmetry, the ω angle was varied between 0° and 45°. In other words, the SANS spectra acquired during this experiment contain, among others, the scattering from (010) interfaces, and from the ($\vec{X}$) interfaces, where the vector $\vec{X}(\omega)$ is varied between [100] and [101] with $\vec{X}(\omega = 0^0) = [100]$ and $\vec{X}(\omega = 45^0) = [101]$. The correspondence between $\vec{X}(\omega)$ and ω was performed using a stereographic projection. The experimental data were reduced using GRASP [77].

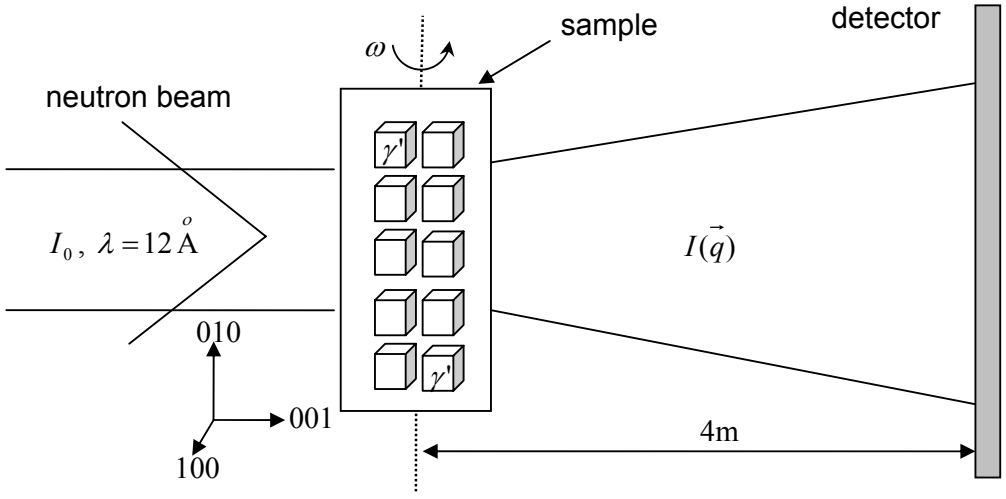

Figure 3.1: Schematic view of the experiment carried out on D11. The sample orientation corresponds to $\omega = 0^0$

- Experimental results

Figure 3.2 shows the evolution of the SANS patterns with the rotation angle ω. At the position $\omega = 0^0$, the SANS pattern shows a fourfold symmetry (Figure 3.2 a). The scattering occurs preferentially along the 100 and 010 crystallographic directions. This is typical of a cuboidal particle shape, whose faces are normal to the <100> crystallographic axes [32, 83]. Moreover, the SANS patterns show similarities in the range $15^0 \leq \omega \leq 45^0$. The streaks in the SANS spectra along the $\overrightarrow{X}$ direction are shorter than when $\omega = 0^0$.This is linked to the flatness and sharpness of the cuboid interfaces. Indeed, in this ω range, the signal along [010] remains constant but that normal to it blurs considerably, resembling to that of spherical particles.

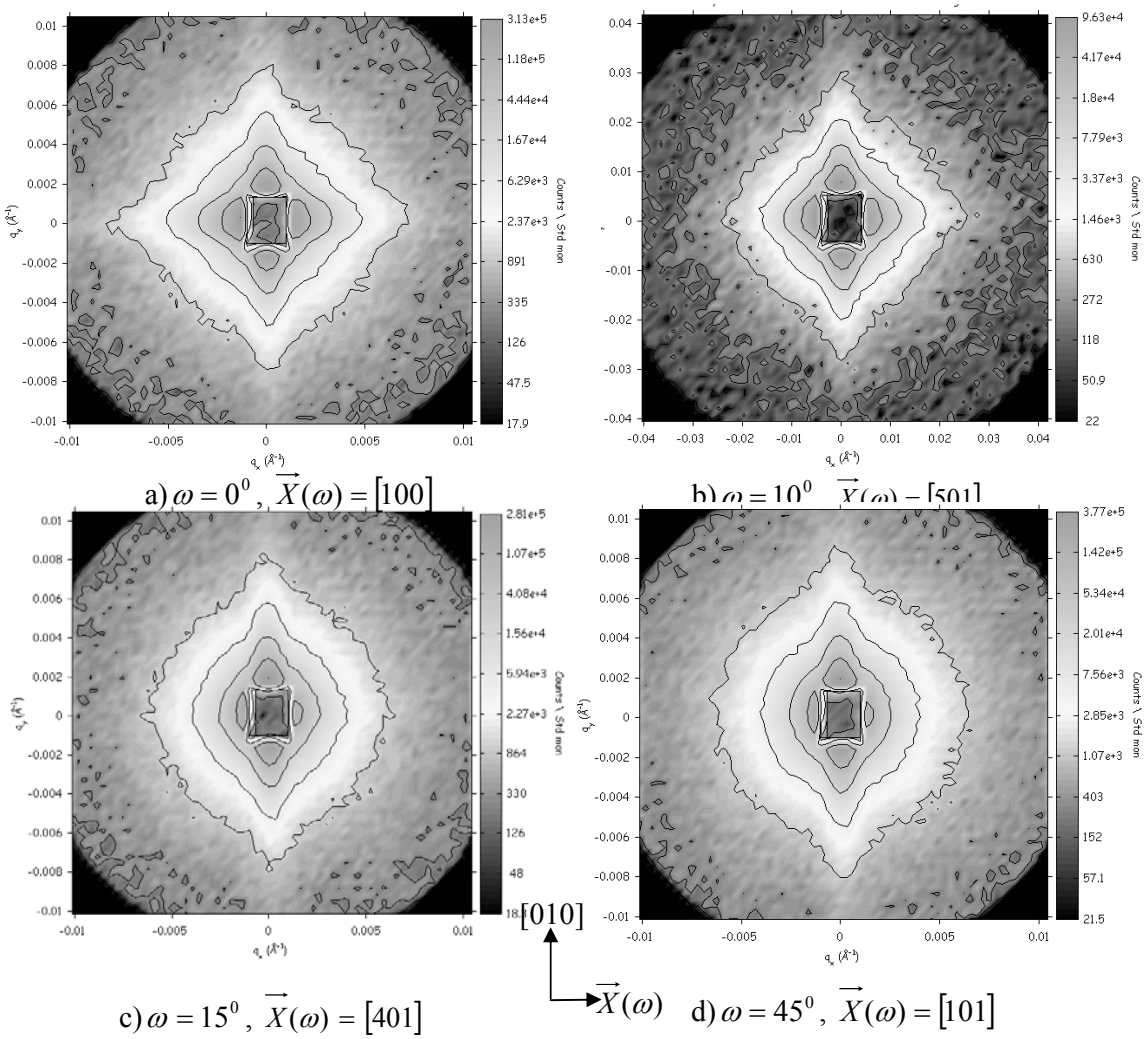

Figure 3.2: SANS patterns obtained at different ω positions on a MC-NG sample after homogeneisation heat treatment.

- Analysis

Figure 3.3 shows the averaged scattered intensity along the crystallographic axes. It can be seen that the scattered intensity shows an asymptotic behaviour close to q^{-4} when $\omega = 0^0$ and along [010], which is typical of a cuboidal (or spherical) shape [83]. In the range $15^0 \leq \omega \leq 45^0$, the asymptotic behaviour deviates from q^{-4} and is closer to q^{-3}. This means that the observed interface is between that of a perfectly flat surface (q^{-2} asymptotic behaviour) and that of a sphere (q^{-4} behaviour) [83]. No major evolution in the SANS signal is visible in the range $15^0 \leq \omega \leq 45^0$, suggesting the spherical character of the particle shape in this ω range. Moreover, no form factor oscillations are visible, indicating a distribution in particle size, inducing a smearing of the form factor (see section II.2.3).

a)

b)

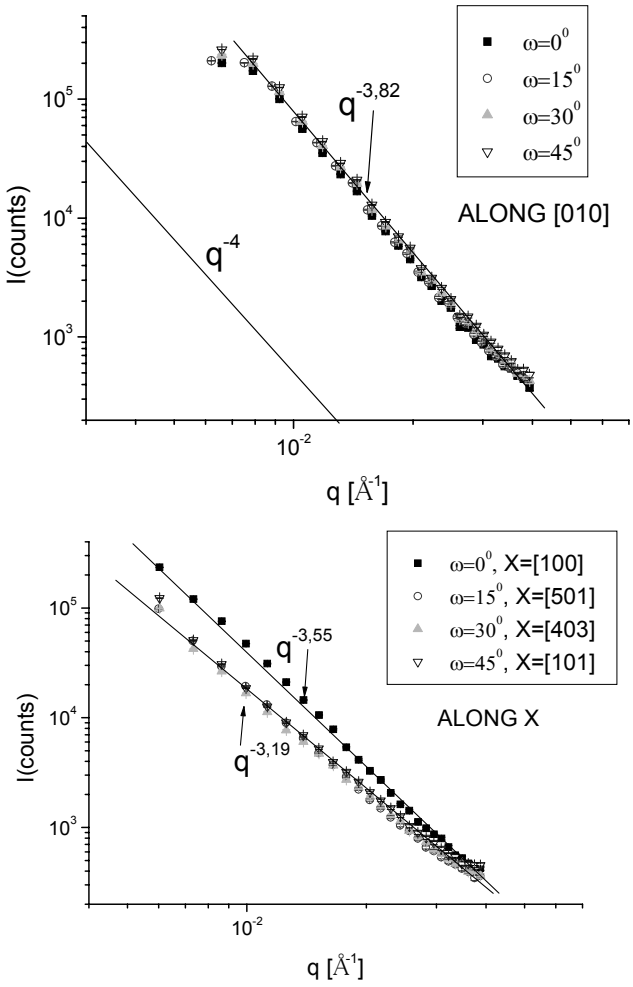

Figure 3.3: Evolution of the scattered intensity with ω: a) along [010] b) along X]

Figure 3.4 shows the evolution of the ratio of the specific areas Σ determined along 010 and $\vec{X}(\omega)$ with the rotation angle ω. The specific area was determined according to Porod law (see section II.2.4). We considered the ratio $\Sigma_{010}/\Sigma_{\vec{X}(\omega)}$, as no major evolution of the specific area is visible if we consider the 010 interfaces (normal to the rotation axis) and as the scattered intensity shows a q^{-4} asymptotic behaviour. Nevertheless, the ratio of specific area is close to unity in a 10° wide ω range centred on $\omega_0 = 0^0$. In this range, the specific area of the $\vec{X}(\omega)$ interface is almost equal to that of the 010 interface. Then, $\Sigma_{010}/\Sigma_{\vec{X}(\omega)}$ increases until ω reaches a critical value $\omega_c = 12^0$ and then remains roughly constant with increasing ω between 15° and 45°. In this range, a ω rotation should induce an evolution in the specific area, unless the particles are spherical. In this particular case, the specific area is invariant with respect to ω rotation. The point ω_c where the specific area along $\vec{X}(\omega)$ reaches its constant value shows therefore the deviation of the particle shape from a perfectly spherical shape to a more cubic one. This point confirms the spherical character of the particle shape in the range $15^0 \le \omega \le 45^0$, as no evolution of the specific area of the $\vec{X}(\omega)$ interface is visible. For comparison, the value of ω_c in the AM1 superalloy was found to be around 30° [84], indicating that the edges of the γ' cuboids in AM1 are much less sharp than those of the MC-NG alloy.

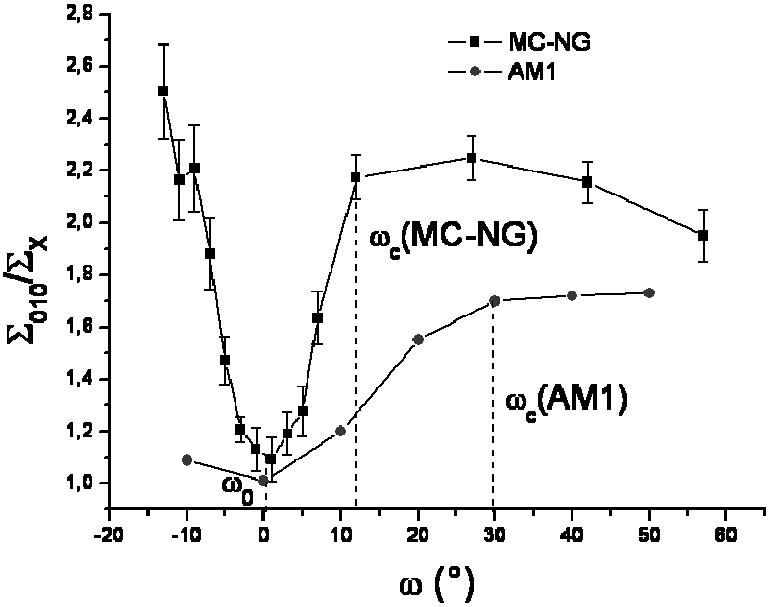

Figure 3.4 : Evolution of the ratio of the specific area along 010 and $\vec{X}(\omega)$ with ω.

- Modelling

The average shape of the γ' particles is approximated as that of a perfect cube of edge size a, inside which eight spheres of radius $R < a/2$ are inserted at each corner, as schematically shown in Figure 3.5a. The angle ω_c corresponds to the angle for which the line joining the middle of a cube edge intercepts a sphere of radius R on another edge normal to the considered edge. This is shown in Figure 3.5b. From this figure, we can estimate the tendency for the particle to be of spherical shape. This tendency can be defined by the ratio R/a. The case of a spherical particle is characterized by a ratio $R/a = 1/2$ and results in $\omega_c = 45°$. Conversely, if the particle is of perfect cubic shape, the ratio tends to zero and $\omega_c = 0°$. This ratio is defined by

$$\frac{R}{a} = \frac{\tan(\omega_c)}{2} \quad (3.1)$$

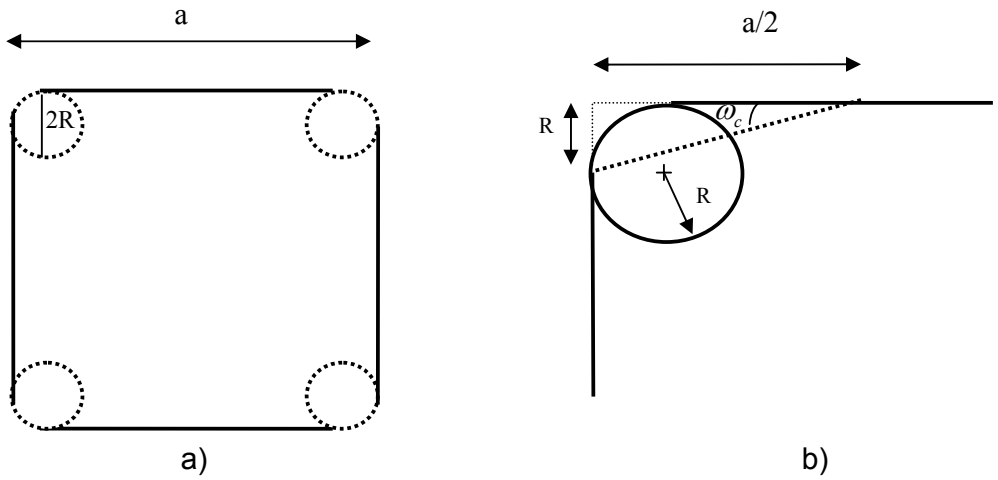

Figure 3.5: a) Schematic view of the model shape of the γ' particles
b)View of the geometry of the model

When this model is applied to the MC-NG and AM1 superalloys, we obtain: $\frac{R}{a}(MC-NG) = 0.11$ and $\frac{R}{a}(AM1) = 0.28$. In other words, the γ' particles show flatter particle edges in the MC-NG superalloy than in the AM1, where the spherical shape is

more pronounced. Moreover, the SANS investigations carried out on the AM1 superalloy have shown that some scattering streaks were observed along the 111 crystallographic direction. This was interpreted as the scattering from the corner of the cuboidal particle which was assumed to be a flat plane with 111 Miller indexes [84].

✓ The DN-2 experiment

The instrument setup allows the investigation of the ultra small angle scattering occurring in the low q-regime with a high q-resolution, as mentioned in section II.2.2. In such conditions, and in the case of superalloys, the structure factor, resulting from the particles interactions, plays a dominant role in the SANS signal. We therefore expect to observe a correlation peak in the SANS signal at the position $q^* = 2\pi / L$, where L is the average centre to centre distance between two particles. The incident neutron wavelength selected by the Si 111 monochromator is fixed at $\lambda = 2.1 \overset{0}{\text{A}}$. $I(q)$ scattering curves were acquired on the PSD detector after reflection on the Si 111 analyser crystal. These data correspond to the reduction of a two dimensional SANS pattern, usually obtained on pinhole cameras, into one dimension along the crystallographic direction determined by the specimen orientation. The SANS signal obtained with the MC-NG sample after homogenisation heat treatment is shown in Figure 3.6. For comparison, the scattering curve obtained in a MC2 first generation alloy in similar conditions is also shown.

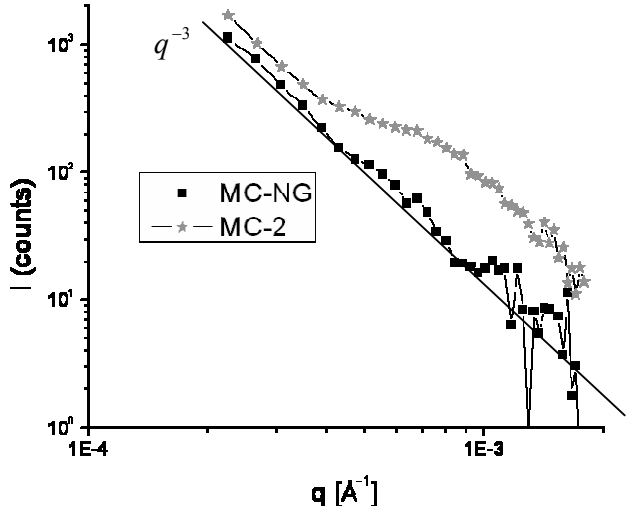

Figure 3.6 : $I(q)$ curve for the MC-NG sample after homogenisation heat treatment

In this q range, the one dimensional scattering curve shows a q^{-3} behaviour, if the background contribution, which becomes significant above $q = 10^{-3}$ Å^{-1}, is ignored. Moreover, some oscillations are visible in the USANS signal but interpreting these oscillations as a correlation peak is not trivial. If a correlation peak is to be observed, it should be centred on $q^* \approx 2.51 \cdot 10^{-3}$ $\overset{0}{\mathrm{A}}^{-1}$, corresponding to an inter-particle distance L around 250nm (see section III.1.2). However, this correlation peak is not clearly visible, neither on D11, neither on DN-2. Figure 3.7 shows a comparison of the SANS spectra obtained in similar experimental conditions on D11 in the case of AM1 and MC-NG alloys.

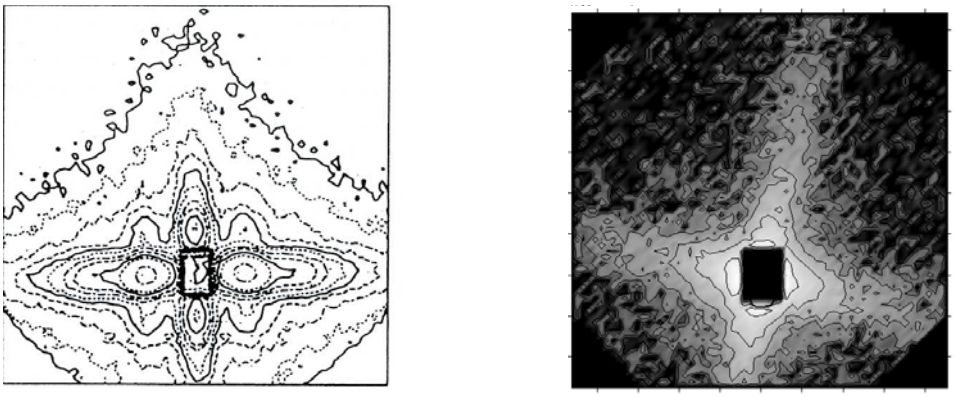

a) AM1 b) MC-NG

Figure 3.7: SANS spectra obtained on D11 in the small q-range

It can be noticed that the observed oscillation is much broader in the case of the MC-NG alloy than the correlation peak observed in the AM1. The absence of the correlation peak in the MC-NG can be attributed to a less regular spatial arrangement of the γ' particles, thus inducing a smearing of the structure factor. Nevertheless, as schematically shown in Figure 3.8, the averaging of the intensity along the 100 crystallographic direction may result in an increased broadening of the correlation peak, as a result of the overlap of the 100 and 010 correlation peaks. The latter are usually observed in the neighbourhood of the beamstop when using a pinhole experimental setup. We can therefore only qualitatively conclude that the microstructure of the MC-NG is rather irregular compared to that of the AM1.

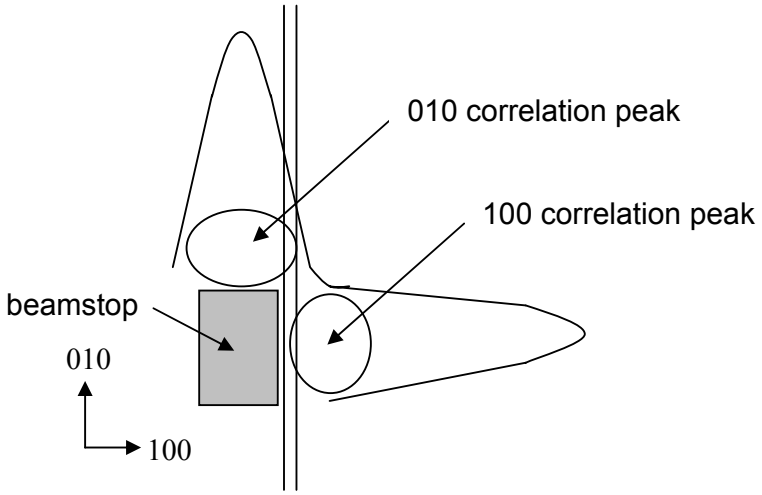

Figure 3.8: Correlation peak broadening due to averaging from a tow dimensional scattering curve to a one-dimensional one

III.1.2 SEM investigation of the initial microstructure

Scanning electron microscopy was used to complete the microstructure observations in reciprocal space by SANS. Indeed, SEM allows microstructure observation in real space. However, it must be pointed out that the number of particles observed by SEM is far below that observed by means of small angle neutron scattering, which provides bulk information on large sample volumes. Therefore, statistical results may differ between the two techniques. A sample of MC-NG after homogenisation heat treatment was prepared according to the protocol described in section II.1.1. Figure 3.9a shows the obtained microstructure. For comparison, the microstructure of the AM1 alloy after homogenisation heat treatment is shown in Figure 3.9b.

It can be seen that the spatial arrangement of the γ' particles is rather irregular, although the cuboids are all aligned along the <100> crystallographic axes. This observation confirms the fact that the absence of the correlation peak is due to the irregular arrangement of the particles.The shape of the γ' particles appears to be close to that of a perfectly cubic particle, with slightly spherical corners. The γ' particles in the MC-NG superalloy have a rather cubic shape with rounded corners. The cubic character of the particle shape is more pronounced in the case of the MC-NG, when compared to that of AM1 [6]. These observations confirm the SANS

results described above. The flat maximum of $\Sigma_{010}/\Sigma_{\vec{X}(\omega)}$ observed in Figure 3.4 can also be explained by the strong disorientation of the γ' particles observed in MC-NG. In such conditions, the superposition of the SANS signal from each particle results in an average SANS signal similar to that of spherical particles.

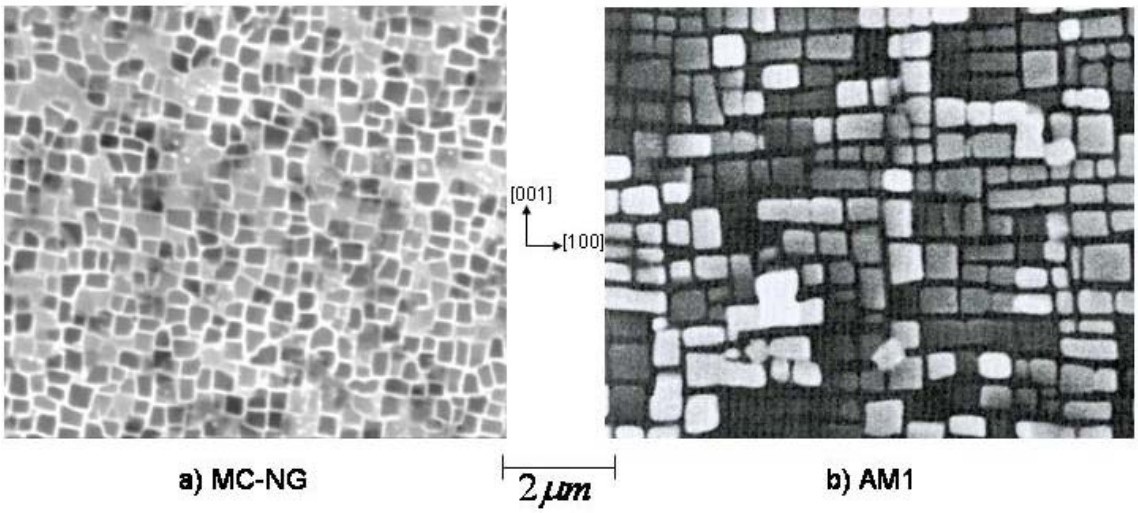

Figure 3.9: SEM observation of the AM1 and MC-NG microstructures after homogenisation heat treatment: a) black: γ'; white: γ; b) white: γ'; black: γ

On the other hand, it is observed that all the γ' particles do not have the same size. The size distribution was determined using the ImageJ freeware, by first adjusting the threshold of the image shown in Figure 3.9a in terms of grey levels, and analysing the particle size distribution. The resulting particle size distribution is shown in Figure 3.10. On the experimental data, three maxima can be observed. They correspond to three particle size distributions. The first one contains the particles whose size is between 100 and 350 nm. This is the main contribution. The second and third size distributions are much less populated (less than 10% of the whole population each) and contain the γ' particles whose size is around 400nm and 510nm, respectively. Considering statistical aspects, these two distributions will not be considered further. The main particle size distribution (first maximum) can be adjusted using a lognormal function, whose equation is given by

$$f(x,\mu,\sigma) = \frac{\exp(-\frac{(\ln(x)-\mu)^2}{(2\sigma)^2})}{x\sigma\sqrt{2\pi}} \qquad (3.2)$$

where μ and σ are the mean value and standard deviation respectively. The adjustment of the experimental curve with the lognormal distribution gives an average particle size of $\mu = 212nm$. For comparison, the mean γ' size in the AM1 superalloy after homogenisation heat treatment was found to be around 350nm. The presence of this particle size distribution in the microstructure of the MC-NG induces a smearing of the form factor in the SANS signal, as previously mentioned.

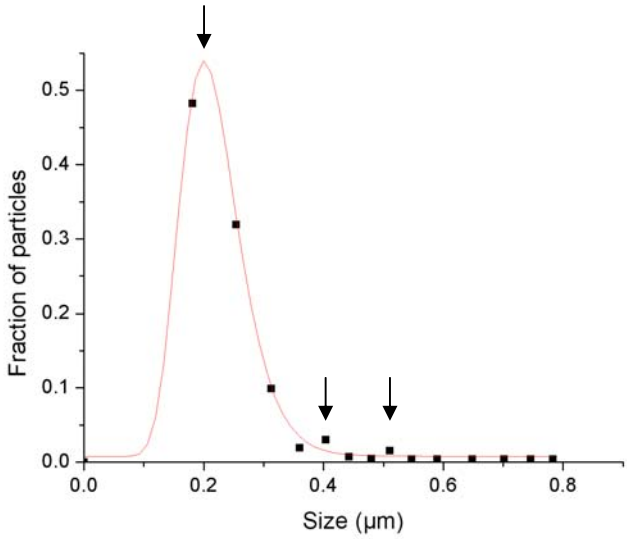

Figure 3.10 : Particle size distribution observed in the MC-NG alloy after homogenisation heat treatment. (dots: experimental data, line: fit of the main size distribution with a lognormal function). The three maxima are indicated by arrows.

III.1.3 Determination of the initial lattice parameter mismatch

The lattice parameter mismatch between γ and γ' phases in the MC-NG superalloy after homogenisation heat treatment was determined using high resolution diffraction of high energy synchrotron radiation at BW5 in Hamburg (see section II.3). A specimen was cut out of a MC-NG sample after homogenisation treatment and mounted on the triple crystal diffractometer (see section II.3.2) so as to investigate the 002 reflection. First, an ω scan was performed in order to analyse the sample mosaicity. The ω position was then fixed at the position corresponding to the maximum diffracted intensity. An α scan (analyser crystal rotation) was then carried out on the 002 reflection in order to obtain the lattice parameter distribution, from which is determined the lattice parameter mismatch. The resulting diffraction profile

and adjustment are shown in Figure 3.11. The lattice parameter mismatch was determined according to the procedure detailed in section II.3.3 and was found to be $\delta^{3D} = -0.14\%$. The application of equation (2.16) leads to a stress free lattice parameter mismatch value of $\delta = -0.057\%$. This value is in agreement with the value determined in [6] ($\approx -0.05\%$).

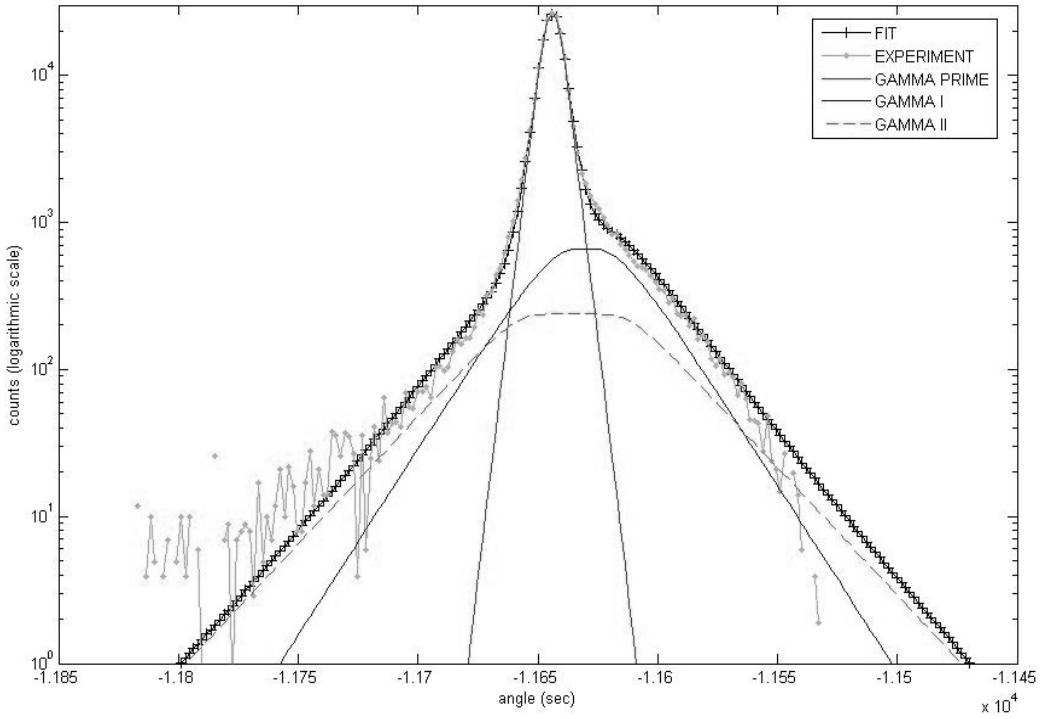

Figure 3.11: Diffraction pattern around the 002 reflection in the MC-NG superalloy after homogenisation heat treatment (log scale)

III.2 Microstructure evolution during strain induced rafting

As mentioned in section I.4, strain induced rafting of γ' particles occurs when a plastically deformed sample is annealed at high temperature (around 1100°C). The microstructure evolution during this annealing has been examined in detail using the SANS technique. An *in-situ* annealing of a deformed sample was carried out at the V4 pinhole camera at HMI (see section II.2). The morphology change of the γ' particles has been characterized and the associated kinetics identified. The influence of the amount of plastic strain introduced in the material prior to the high temperature annealing, as well as that of the annealing temperature, on the kinetics of rafting are discussed.

✓ **Experimental procedure**

Two MCNG samples were strained in tension along the [001] direction at 850ºC prior to the SANS experiment. The plastic strains introduced in these samples were 0.2% and 0.6% for samples 1 and 2 respectively. Each sample was then oriented in a Laue camera in order to identify the <100> crystallographic axes. In order to avoid multiple scattering which may occur in thick specimens, thin slices (1.5mm thickness) normal to the [001] axis were cut from each specimen by spark erosion. Each sample was then mounted in a boron nitride (neutron absorber) diaphragm ($1*0.4cm^2$) and placed in a high temperature furnace. The [010] crystallographic direction was placed parallel to the neutron beam. During annealing at 1100ºC and 1050ºC for samples 1 and 2 respectively, successive SANS patterns were acquired. The total *in-situ* annealing time was around 15 hours for both samples. The SANS patterns contain the scattering contributions from 100 and 001 interfaces; as the [010] axis is parallel to the neutron beam. Table 3.1 summarizes the experimental conditions for each investigated sample. In both cases, the neutron wavelength was 6Å and the sample to detector distance was 16m so as to explore the smallest q range attainable without too much loss of neutron flux. The microstructure evolution occurring during the high temperature annealing can then be deduced from these measurements. After annealing, SANS patterns with λ=19Å were recorded so as to widen the investigated q range towards low q-values for the investigation of the final microstructure. The coarsening of the precipitates results in an increased size of the particles, whose visibility becomes better in the small q range accessible at this wavelength. In these conditions, after sufficient ageing time, γ' platelets (or rafts) are expected to form perpendicularly to the tensile axis [001]. The SANS signal is therefore expected to decrease in the low q range along the [100] and/or [010] direction.

Sample number	Plastic strain	Annealing Temperature (°C)
1	0.20%	1100
2	0.60%	1050

Table 3.1: Experimental conditions for each investigated sample

✓ **Experimental results**

Figure 3.12 shows the two dimensional SANS patterns acquired before and after high temperature annealing of sample 1. Similar results were obtained in the case of sample 2. The fourfold symmetry observed on the SANS pattern that was obtained at room temperature prior to annealing is representative of the cuboidal shape and of the periodic spatial arrangement of the γ' precipitates after the standard heat treatment. This means that the average particle shape was not altered during the plastic deformation, consisting in the introduction and glide of dislocations. The fourfold symmetry becomes twofold after the high temperature annealing, as shown in Figure 3.12b. The SANS intensity decreases along the [100] crystallographic direction during annealing. In the investigated q-range (large q values), the scattered intensity along a crystallographic direction, more sensitive to the average form factor, is proportional to the specific area of the interface normal to this direction, as stated by Porod approximation. In other words, as the scattered intensity decreases along the [100] direction, the specific area of the 100 interfaces becomes smaller. This decrease is attributed to the disappearance of some 100 interfaces attributed to the coalescence of two adjacent cuboidal particles along [100]. This result clearly indicates a directional coarsening of type N of the γ' particles. The resulting microstructure consists in a lamellar γ/γ' structure normal to the tensile axis. As the lattice parameter mismatch is negative in the investigated alloy, and a tensile plastic strain was introduced, the resulting microstructure corresponds to the expectations.

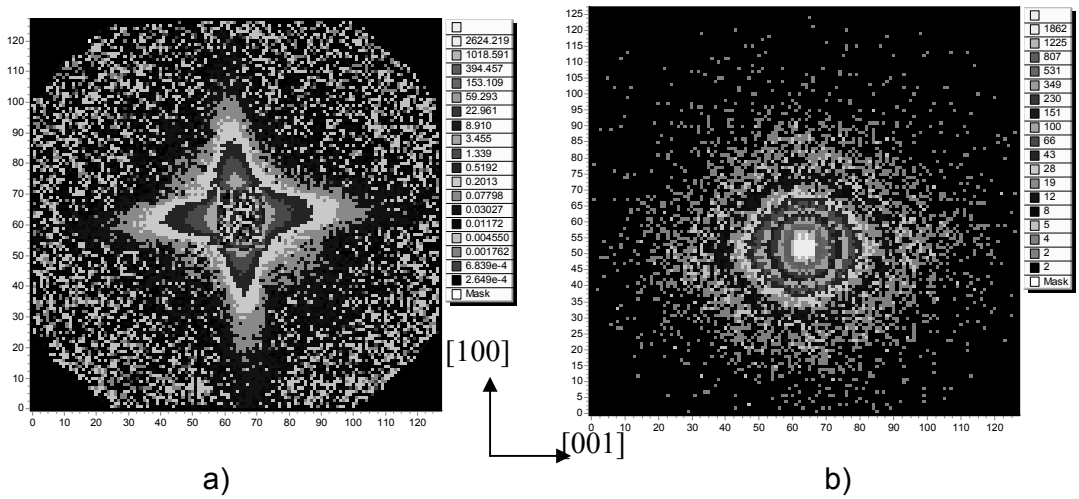

a) b)

Figure 3.12: SANS patterns obtained in sample 1 a) before annealing at room temperature (λ=6Å, 0.2<q<2 $Å^{-1}$) and b) after annealing at 1100ºC (λ=19Å, 0.06<q<0.6 $Å^{-1}$).

✓ **Analysis**

Data were reduced and corrected using BerSANS software developed at HMI [78]. Corrections for background, solid angle viewed by a pixel on the PSD, sample and cell transmissions were taken into account. The data were averaged along the [100] and [001] crystallographic direction using 30° wide angular sectors. Figure 3.13 and 3.14 show the comparison of the obtained one dimensional $I(q)$ curves before and after the high temperature annealing in sample1 and sample 2. By comparison of the two figures, we observe that, in both samples, the scattering intensity shows a similar behaviour before the annealing along the [100] and [001] directions. Moreover, after the high temperature annealing, the scattered intensity along the [100] direction is smaller at low q-values than that along the [001] direction (see Figures 3.13 and 3.14). In both samples, the scattered intensity along [001] remains constant throughout the thermal treatment. The observed asymmetric behaviour of the scattered intensity is the signature of a morphology change of the γ' precipitates from a cuboidal shape to that of a platelet normal to the [001] crystallographic axis. Moreover, the evolution of the 010 interfaces can be assumed to be similar to that of 100 interfaces, by symmetry. The intensity scattered by the 010 interfaces is not visible in the performed experiment, as those interfaces are perpendicular to the beam. The hypothesis that the 010 interfaces behave in the same way as 100 interfaces is obtained from the symmetry of the plastic prestrain (see section IV.3.1, eq (4.26)), which is believed to be responsible for rafting.

The evolution of the scattered intensity along [100] with the annealing time is not large enough to quantify the kinetics of the morphology change of the γ' particles. As the investigated q-range corresponds to the Porod regime, the scattered intensity is related to the specific area. The application of Porod approximation on the SANS data collected during the annealing provides information on the kinetics of the particles morphology change. Figure 3.15 shows the evolution of the specific surface area calculated with equation.(2.10) with the annealing time for both samples and for the 100 and 001 interfaces.

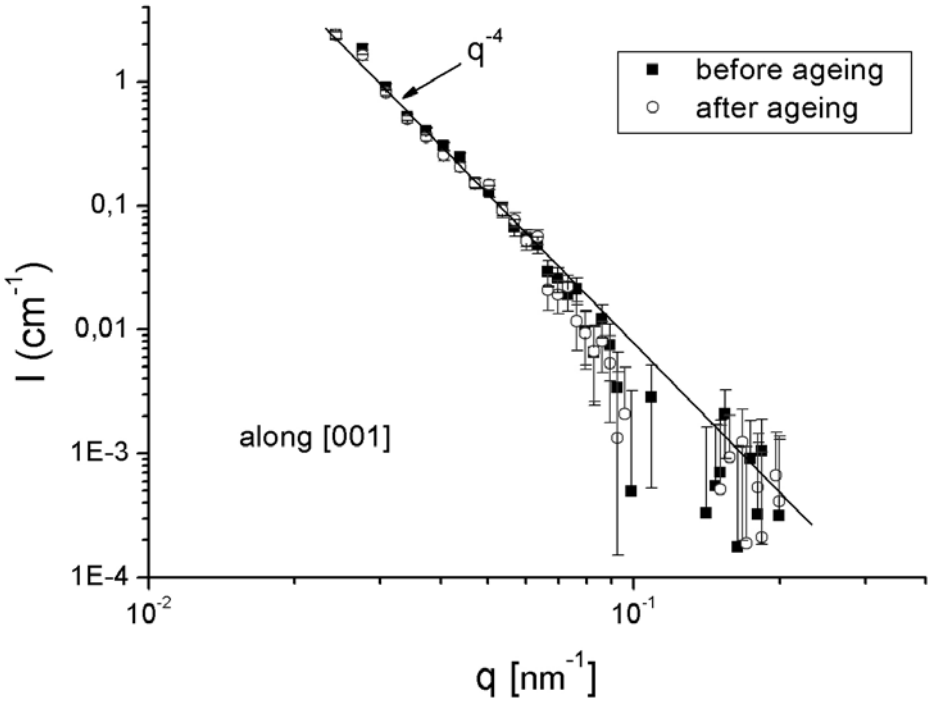

a) along [001]

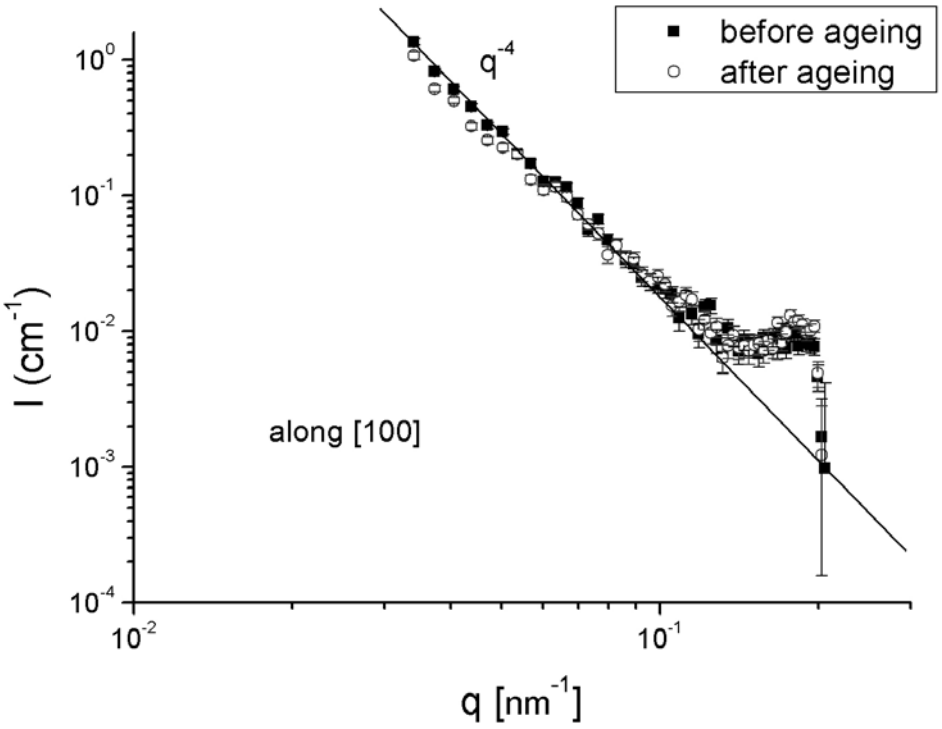

b) along [100]

Figure 3.13: $I(q)$ curve for sample 1 (0.2% plastic strain, T=1100°C)

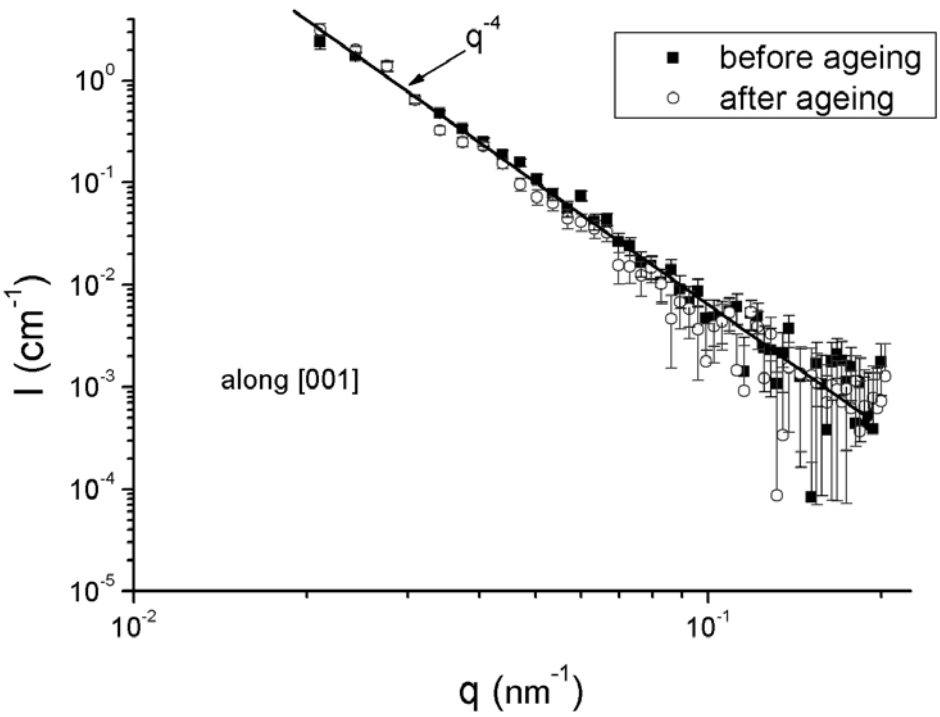

a) along [001]

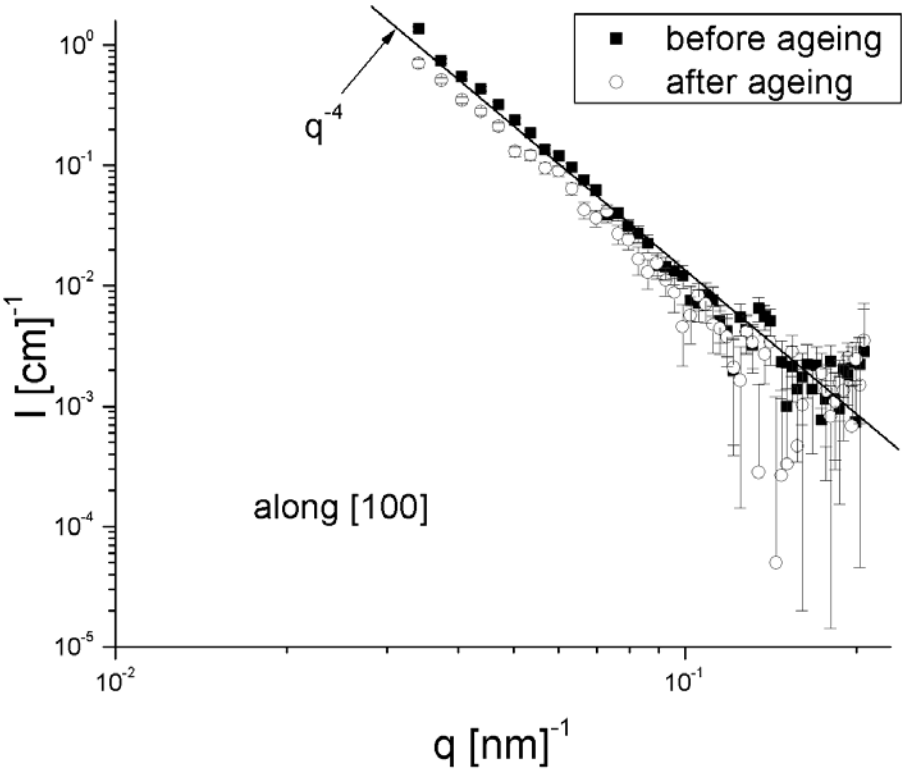

b) along [100]

Figure 3.14: $I(q)$ curve for sample 2 (0.6% plastic strain, T=1050°C)

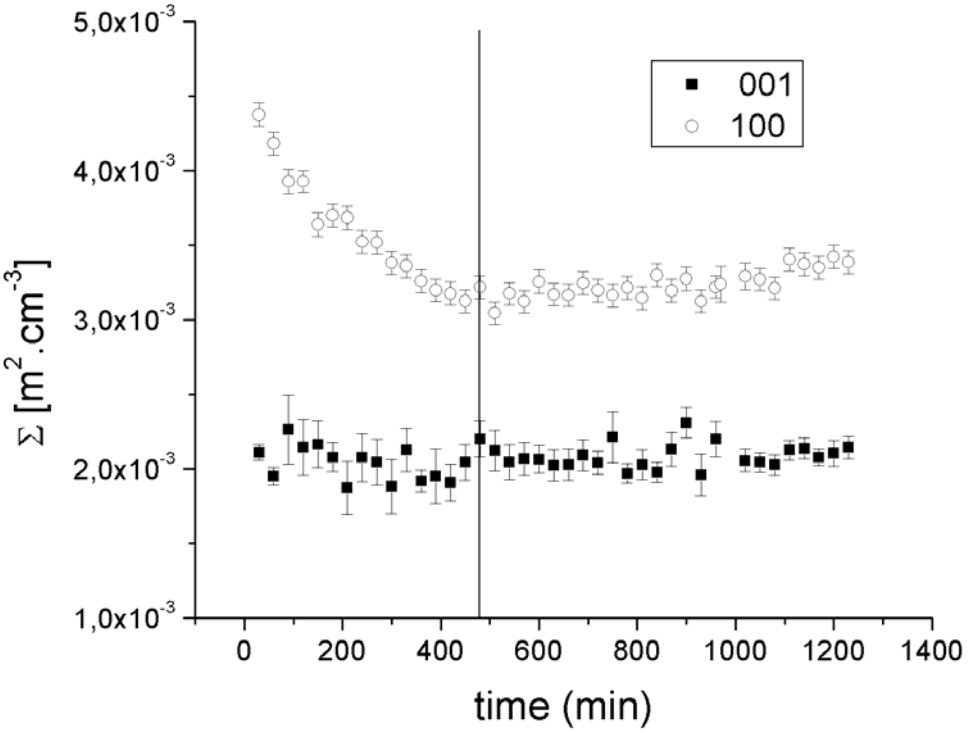

a) 0.2% plastic strain - annealing at 1100°C

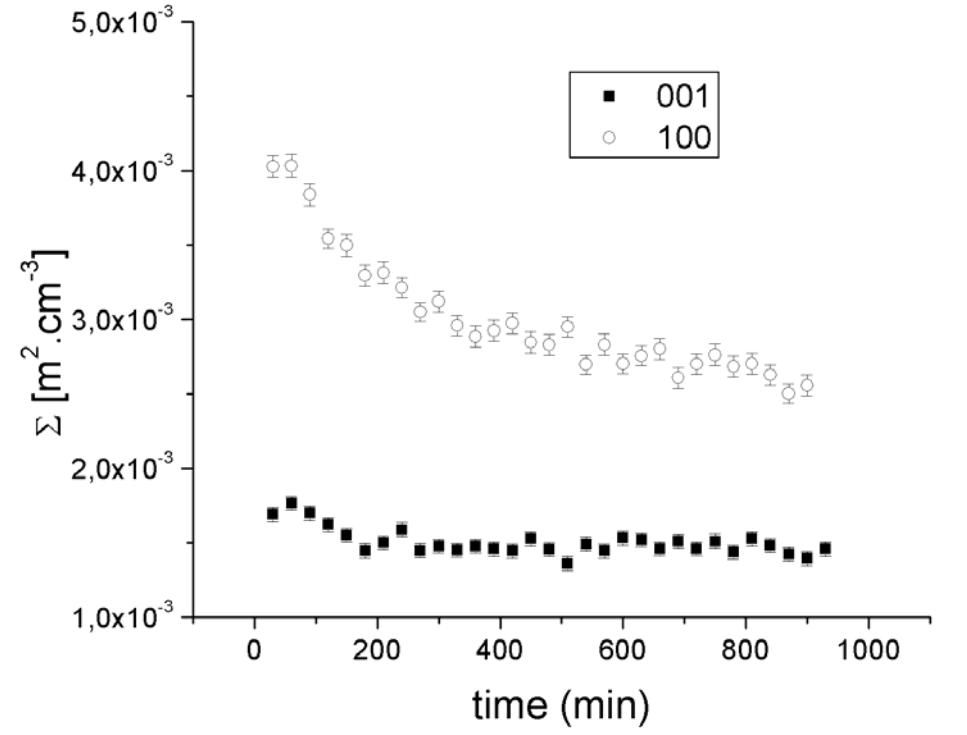

b) 0.6% plastic strain – annealing at 1050°C

Figures 3.15: Evolution of the specific area with annealing time: a) Sample 1
b) Sample 2

In each sample, the specific area of the 001 interfaces remains almost constant throughout the whole annealing. Its mean value is smaller than the specific area of the 100 interfaces in both samples. This may be due to a misorientation of the neutron beam with the (001) lattice planes of the sample. The decrease of the specific area of the 100 interfaces is clearly visible. In sample 1 (0.2% plastic strain, annealed at 1100°C), this decrease can be decomposed into two regimes, as shown in Figure 3.14a. The first regime corresponds to the first hours of annealing (up to around 450min), during which the decrease in specific area is relatively fast and can be fitted with an exponential decay.

During the second regime, the 100 specific area is roughly constant or even slightly increases. In the case of sample 2 (0.6% plastic strain, annealed at 1050°C), the decrease of the specific area of the 100 interfaces is continuous and exponential. The exponential decay of the (100) specific area in samples 1 and 2 can be compared. The time constants were estimated in both samples and were found to be close to each other (274±78 min. for sample 1 and 231±21 min. in sample 2). This result is surprising because the annealing temperature for the sample 2 is lower than that of sample 1. Diffusion processes should therefore be slower in sample 2 than in sample 1, but a reverse trend seems to be observed. As no temperature effect on the microstructure evolution is observed, we can consider the role of plastic strain, which is larger in sample 2 than in sample 1. We can reasonably speculate that the dislocations and/or vacancies created during plastic deformation provide fast diffusion paths for the atomic diffusion involved in rafting. Such a mechanism would confirm the crucial role played by the amount of plastic strain on the diffusion processes involved in rafting.

It must be pointed out that the values of specific area determined above are three orders of magnitude below that expected. This discrepancy can be attributed to the values of chemical composition used in the evaluation of the contrast in terms of scattering length density $\Delta\rho$. These values come from atomic probe spectroscopy investigation, which provide extremely local information. The strong partitioning of heavy refractory elements is therefore not accounted for in the evaluation of $\Delta\rho$. In contrary, SANS investigation provide bulk information and consist in an average

between dendritic and interdendritic regions of the specimen, taking therefore the chemical elements partitioning into account. Moreover, a small change in the value of the contrast in terms of scattering length density results in a large change in the determination of the specific area, as it is proportional to $(\Delta\rho)^{-2}$.

Moreover, if these results are compared with those from a similar experiment that was carried out on the AM1 alloy [8], we can see that the kinetics of rafting is comparable to that observed in MC-NG. In this analysis, the authors considered the evolution of the peak correlation position as rafting proceeds during the high temperature annealing, and using a similar experimental setup as that used in the case of MC-NG. They found that the microstructure evolution was completed after around 8 hours of ageing at 1100°C in a sample that was plastically deformed at 0.2%, as shown in Figure 3.16. Surprisingly, we can deduce from this remark that the diffusion processes involved in rafting do not seem to depend even on the alloy composition. This remark confirms the crucial role of plastic strain and associated dislocations and/or vacancies in the diffusion processes involved in strain induced rafting.

However, in the particular case of the MC-NG alloy, there is a strong partitioning of the heavy elements such as rhenium and ruthenium. These two elements are those showing the slowest diffusion coefficients in the matrix [55]. They might therefore not be involved in the rafting process and incorporated into the γ' phase. Further investigations are required to confirm this hypothesis. We can expect an increase in Re and Ru content in the composition of the γ' phase. This high concentration of heavy elements could be localised where the vertical γ channels have disappeared during rafting.

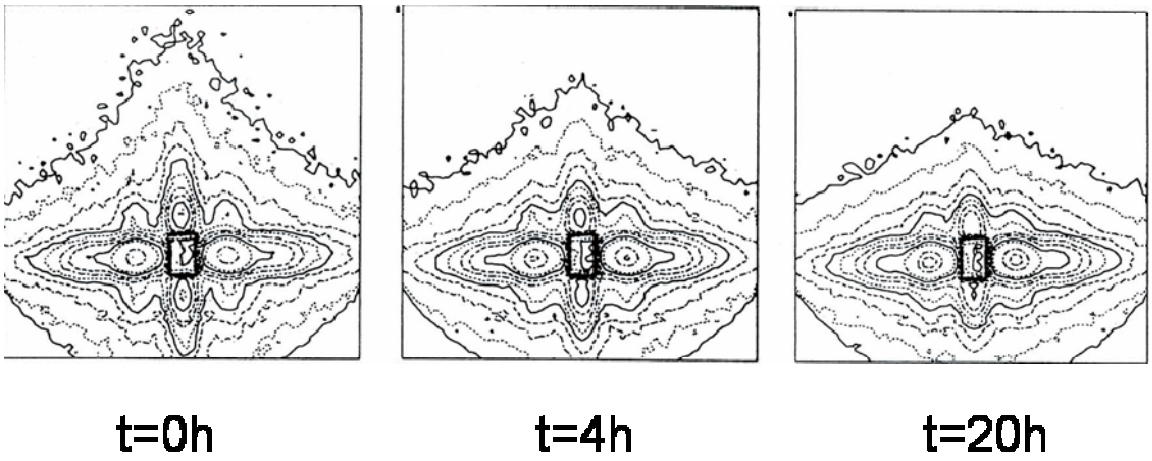

a)

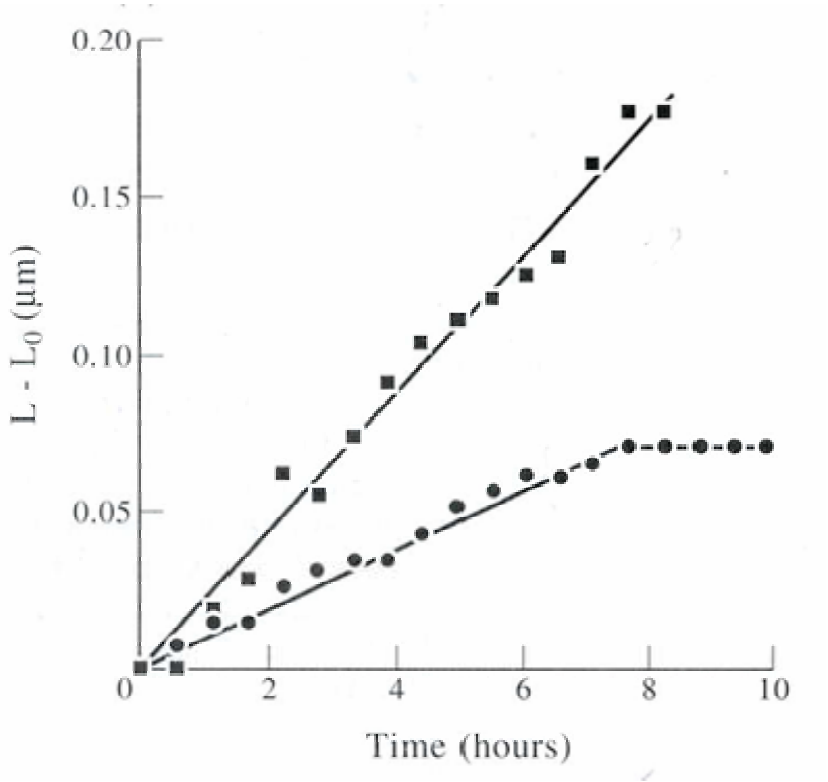

b)

Figure 3.16: a) SANS pattern evolution during strain induced rafting in AM1 (0,2% plastic strain, T=1100°C)

b) Evolution of the correlation peak position, as from [8] (squares: along [010], full circles: along [001]

III.3 Evolution of the lattice parameter misfit during strain induced rafting

✓ Experimental procedure

The experiment was carried out at the high energy X-Ray diffraction beamline BW5 at Hasylab (Hamburg, Germany). The aim of the experiment was to follow in-situ the evolution of internal stresses during the strain induced rafting process. As mentioned in section II.3, the lattice parameter mismatch between γ and γ' phases can be deduced from diffraction experiments using a high resolution setup. The lattice parameters are used as a strain gauge. The matrix plastic deformation produces anisotropy inside the sample. It is therefore essential to investigate two reflections: 002 (along the tensile axis) and 200, which is equivalent to 020 by symmetry. This allows the determination of the lattice misfit parallel $\delta_{//}$ (002 reflection) and perpendicular $\delta_{\perp}$ (200 reflection) to the tensile axis.

Prior to the experiment, two sets of samples were deformed along [001] at 850°C until the amount of plastic strain reached 0.2% and 0.6%. The first set (samples 1 and 2) was deformed at 0.2% and the second set (samples 3, 4, 5 and 6) at 0.6%. Samples 1, 2, 3 and 4 were successively placed in a high temperature furnace and annealed at 1100°C for around 15 hours, while samples 5 and 6 were annealed at 1050°C for around 30 hours. Successive acquisition of the reflections during each annealing gives access to the evolution of the lattice parameter mismatch during strain induced rafting. However, it must be pointed out that, due to some beam instabilities, the experiments conducted in samples 3 and 4 were interrupted for several days. This might have affected the experimental results.

The synchrotron beam energy was selected by a perfect Si 311 crystal and set at 120keV. The slits placed in front of the sample and the detector defined a square diffracted beam section whose dimensions were 1*1mm^2, thus making possible average measurements over dendritic and interdendritic areas. The probed volume is elongated over the whole sample thickness, which increases the averaging statistics.

✓ **Experimental results**

Figure 3.17 shows the evolution of the 002 and 200 reflections in samples 1 to 4. The same trends were observed in samples 5 and 6, for which the annealing temperature was 1050°C. During the annealing, the γ and γ' contributions to the reflections get better and better separated. This phenomenon is typically observed during rafting [82], as mentioned in section II.4. Moreover, we can see that the shift between γ and γ' peaks is increased during annealing on the 002 reflections. This means an increase in the measured or apparent lattice parameter mismatch parallel to the tensile axis. If we consider the stress balance condition, which implies that the sum of all stresses inside the whole volume of a material must vanish, we can expect a decrease of the measured lattice parameter mismatch perpendicular to the elongation axis. In such conditions, the γ and γ' peaks on the 200 reflection should get closer to each other as the high temperature annealing proceeds.

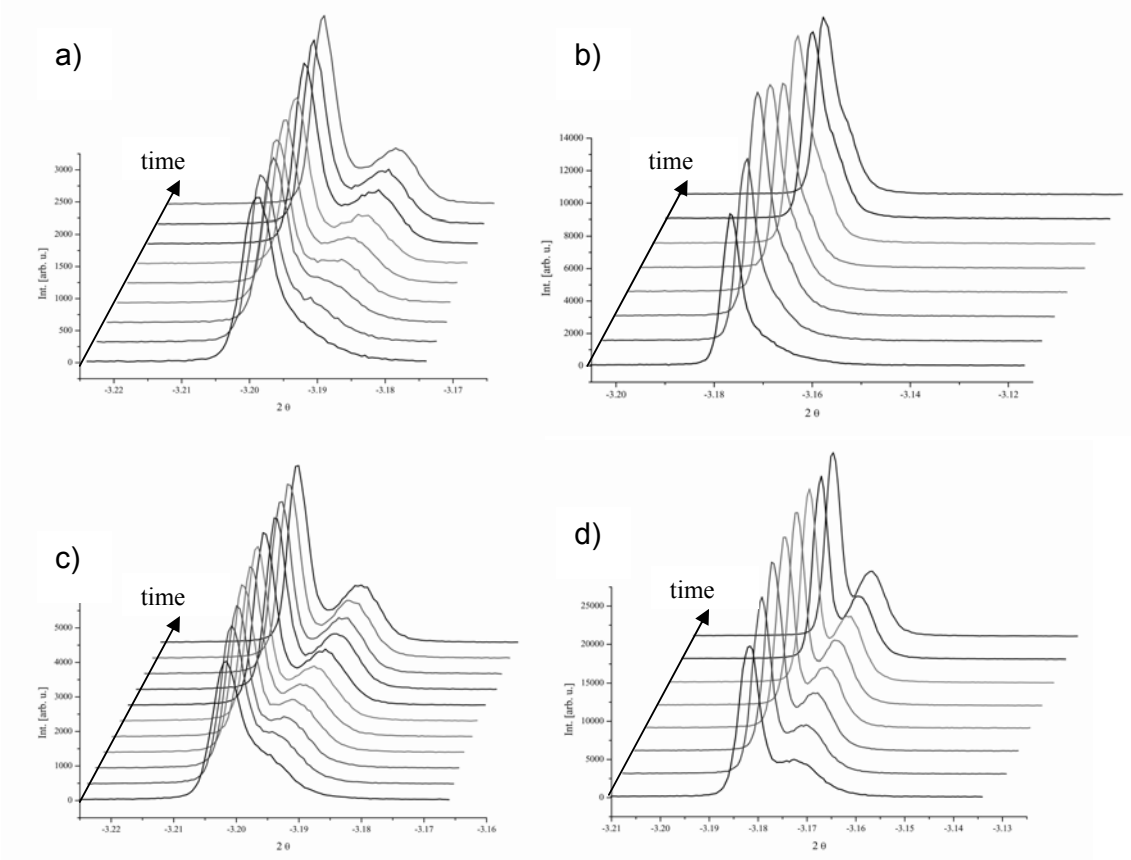

Figure 3.17: Peak profile (I *vs.* 2θ) evolution during ageing at 1100ºC (linear scale)
a) reflection 002, strain +0.2%, b) reflection 200, strain +0.2%
c) reflection 002, strain +0.6% and d) reflection 200, strain +0.6%

This evolution of the apparent mismatch parallel and perpendicular to the elongation axis can be easily understood if microstructure aspects are considered. During rafting, the γ channels parallel to the deformation axis disappear. In the case of the 200 reflection, only the γII channels perpendicular to the deformation axis remain throughout the whole annealing (see Figure 3.18a). This means that the γI contribution, leading to a large apparent misfit, becomes less and less significant as rafting proceeds. In such conditions, the apparent mismatch perpendicular to the deformation axis appears to decrease during rafting. In the case of the 002 reflection, the γI contribution becomes predominant, as γII channels, and therefore their contribution to the diffraction pattern, disappear as rafting proceeds. This point is shown in Figure 3.18b. The apparent lattice parameter mismatch parallel to the deformation axis then seems to increase.

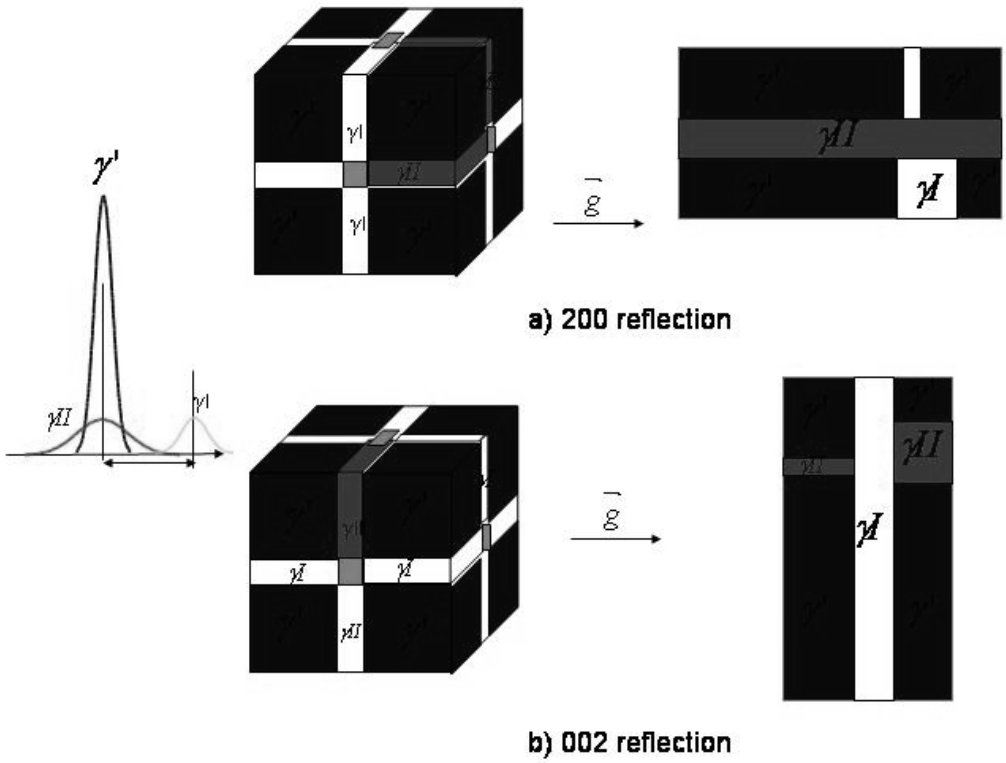

Figure 3.18: Schematic view of the microstructure evolution during rafting and the consequences on the diffraction patterns around the 200 and 002 reflections (black: γ', white and grey: γ)

✓ **Analysis**

The evolution with annealing time of the apparent lattice parameter mismatch parallel (reflection 002) and perpendicular (reflection 200) to the elongation axis is shown in Figure 3.19. Every sample shows the same behaviour, that is an increase in absolute value of the apparent misfit parallel $\delta_{//}$ to the tensile axis and a relaxation of the apparent misfit perpendicular $\delta_{\perp}$.

On the other hand, the annealing temperature plays a dominant role in the kinetics evolution of the lattice parameter mismatch. The evolution of the apparent parallel and perpendicular misfit is much slower at 1050°C than at 1100°C. This suggests a diffusion controlled character of the apparent misfit evolution during strain induced rafting. The evolution of the misfit parallel to the elongation axis shows a first order exponential growth for all annealing temperatures. Moreover, the evolution of $\delta_{\perp}$ with annealing time shows a different behaviour at 1050°C than at 1100°C. At the latter temperature, the evolution of the lattice parameter mismatch perpendicular to the elongation axis can be decomposed into two relaxation regimes, as shown in Figure 3.20. The first relaxation regime is very fast (time constant τ_1) and corresponds to a large decrease of the apparent misfit. The transition between the two regimes occurs at the time t_{trans1}. The second relaxation regime is much slower (time constant τ_2) and makes the misfit perpendicular to the tensile axis converge to an asymptotic value, which is strongly dependant on the amount of plastic strain formerly introduced in the specimen. On the other hand, in the case of an annealing at 1050°C, the time evolution of the apparent lattice parameter mismatch behaves like a single exponential decay (time constant τ). This result is in agreement with the previous SANS observations that show a continuous process for the kinetics of rafting at this temperature. Therefore, the annealing temperature, linked to the γ' volume fraction and lattice parameter mismatch, plays a dominant role on the mechanisms involved in strain induced rafting. In all cases, as mentioned before, the evolution of $\delta_{//}$ shows an exponential growth behaviour (time constant τ_3), whatever the annealing temperature.

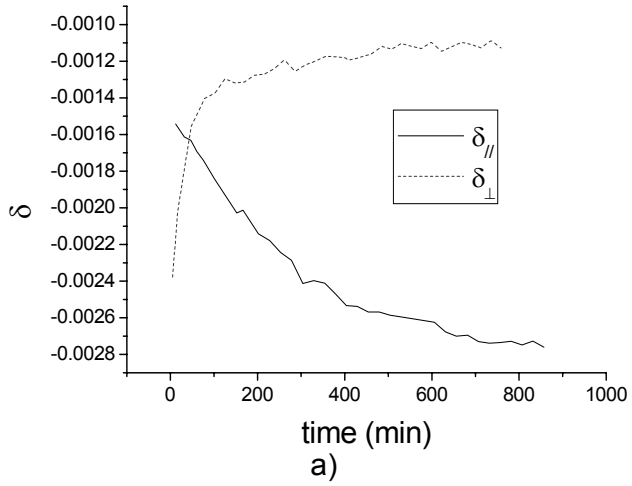

a)

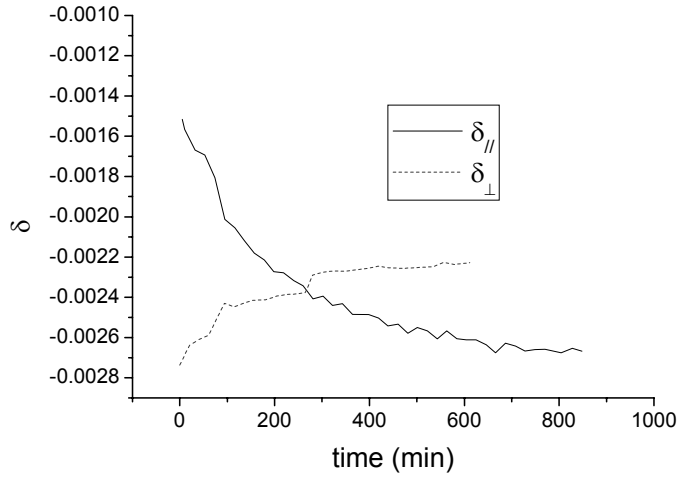

b)

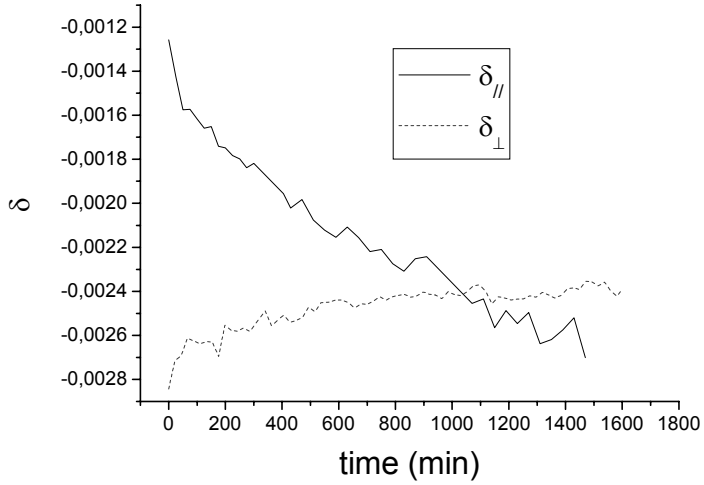

c)

Figure 3.19: Apparent lattice misfit evolution: a) +0.2% strain -1100°C
b) +0.6% strain -1100°C
c) +0.6% strain -1050°C

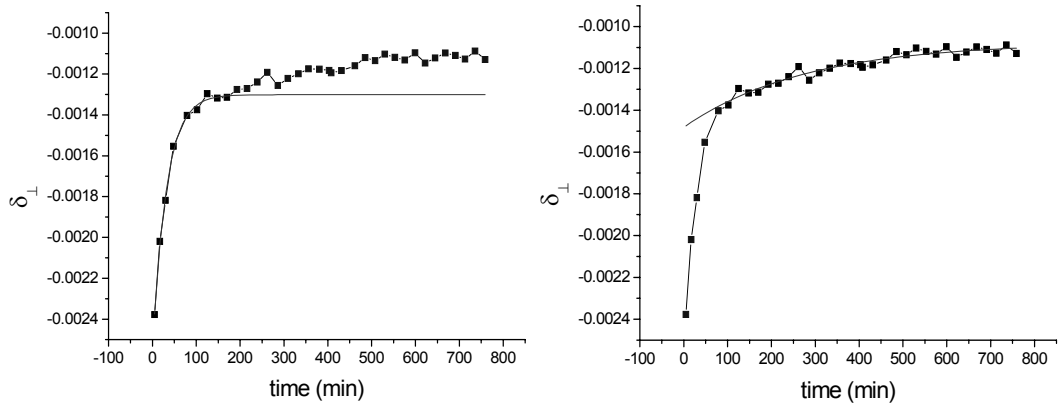

a) b)

Figure 3.20: Distinction between the two regimes of relaxation observed in the evolution of $\delta_\perp$ (samples 1 and 2): a) first regime, $\tau_1 = 30\,\mathrm{min}$
b) second regime, $\tau_2 = 269\,\mathrm{min}$

Plastic strain also seems to influence the mechanisms involved in the morphology change of the particles. At the start of the experiment, the difference between $\delta_{//}$ and $\delta_\perp$ depends on the amplitude of the pre-introduced plastic strain. If we assume that the plastic strain is confined within the γ matrix and that it results from the activation of matrix dislocations on many slip systems, the lateral directions ([100] and [010]) undergo a deformation of $-\varepsilon_P/2$ while the deformation along [001] on the 001 interfaces is ε_P (see Chapter 4). Moreover, in the case of an annealing temperature set at 1100°C, after sufficient annealing time, the values of δ reach their asymptotic values $\delta_{\min}$ and $\delta_{\max}$ for $\delta_\perp$ and $\delta_{//}$ respectively. The asymptotic misfit values also depend on the amount of plastic strain, as $\delta_\perp$ is proportional to interface dislocation density [82].

Figures 3.21 to 3.23 show the evolution with annealing time of the change in full width at half maximum (FWHM) of the γ and γ' peaks for the 002 and 200 reflections for each type of sample. The change in FWHM at a given annealing time is evaluated in (%) with respect to the initial FWHM value (expressed in $10^{-3}\Delta d/d$) at the beginning of the high temperature annealing during which rafting occurs. Moreover, it

must be pointed out that the FWHM of the γ reflections is always larger than that of the γ' reflections, confirming the hypothesis that plastic strain is confined in the γ matrix. This point is shown in Figures 3.24 to 3.26. In the samples that were annealed at 1100°C, *i.e.* samples 1 to 4, the distinction between two relaxation regimes, corresponding to those observed in the evolution of $\delta_{\perp}$, is clearly visible on the evolution of the FWHM of the 002 reflection.

During the first regime, the FWHM of the γ 002 reflection increases, while the FWHM of the γ' 002 reflection decreases, suggesting that some dislocation rearrangement occurs at the interface between the two phases. Both trends show an exponential behaviour, with very similar time constants τ_4. At the transition time t_{trans2}, the FWHM shows a different behaviour. During the second observed regime, the FWHM of the 002 reflection decreases linearly for both phases (slopes p_1 and p_2 for γ and γ' phases respectively).

On the other hand, the FWHM of the 200 reflection of the γ' phase is almost unchanged at the beginning of the experiment, until a transition time t_{trans3} at which it suddenly drops. Possible physical origins for this discontinuity may be the coalescence of two adjacent particles, through the suppression of the 100 interfaces , or the rearrangement of interface dislocations. Further investigations are required to confirm these hypotheses. The FWHM of the 200 reflection from the γ phase shows a continuous exponential decay, whose time constant is defined as τ_5. The results from the different fits performed are summarized in Table 3.2. By examining the quantities $\tau_1, \tau_2, \tau_3, \tau_4, \tau_5, t_{trans1}, t_{trans2}, t_{trans3}, p_1, p_2$, the influence of temperature and plastic strain on the kinetics of the mechanisms involved in strain induced rafting are discussed. A summary of the observed behaviours of the lattice parameter mismatch and the peak width is given in Figure 3.27.

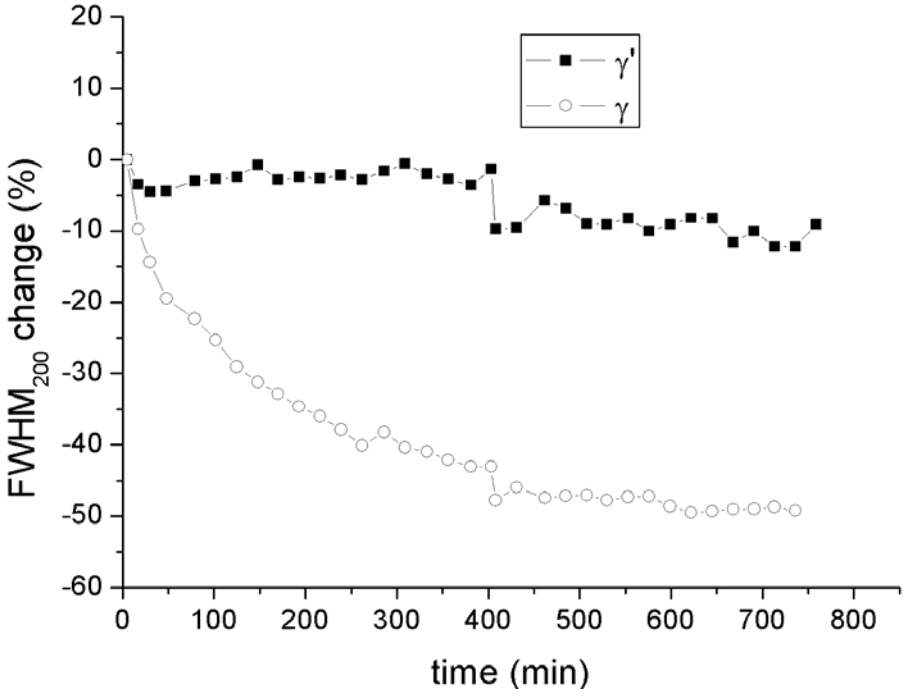

a) 200 reflection

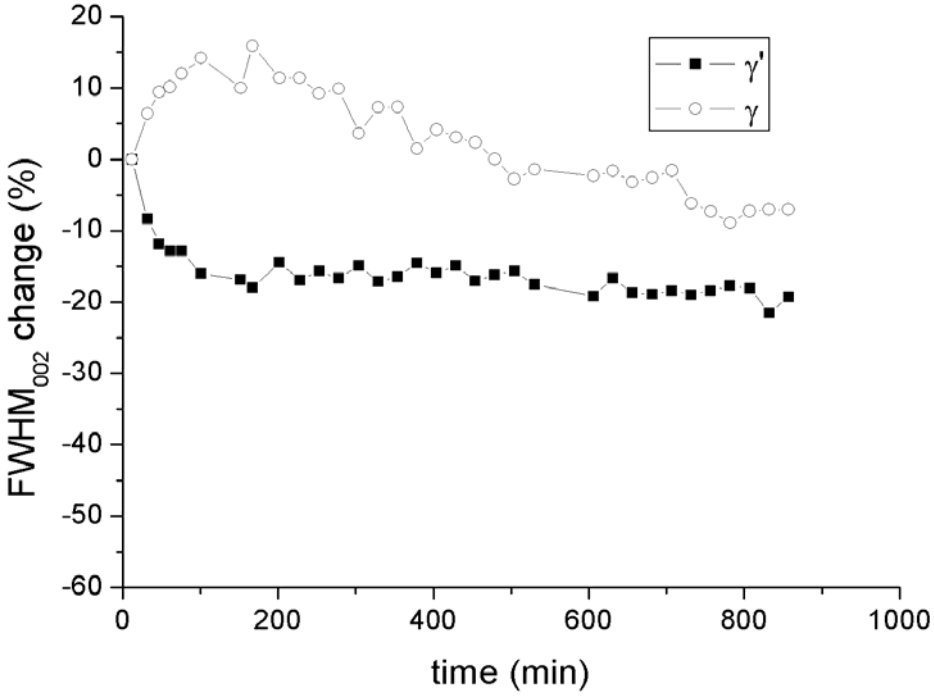

b) 002 reflection

Figure 3.21: Evolution of the FWHM change in the samples deformed at 0.2% plastic strain and annealed at 1100°C (samples 1 and 2)

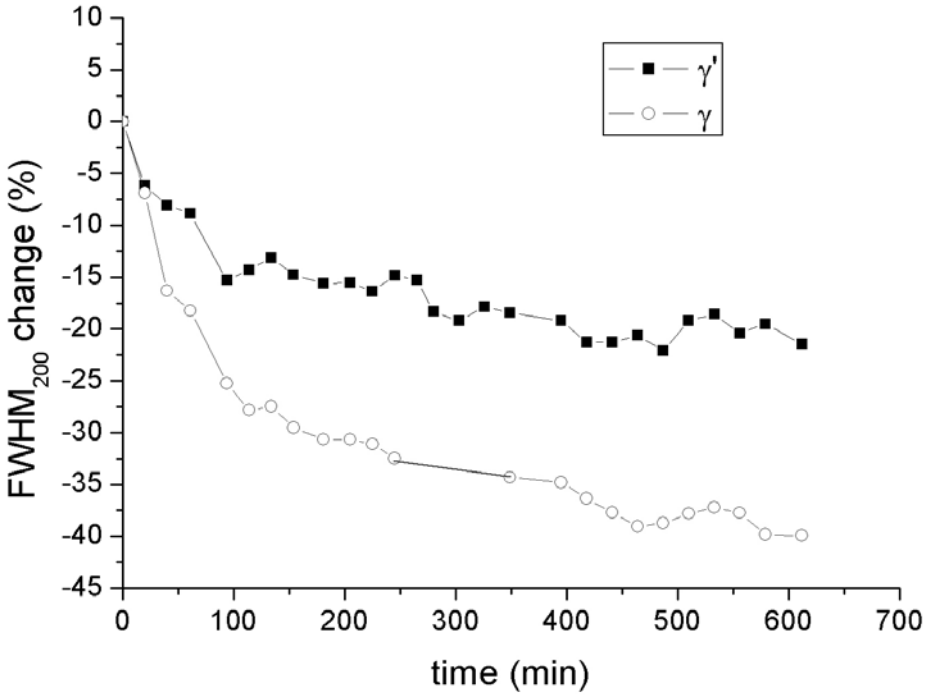

a) 200 reflection

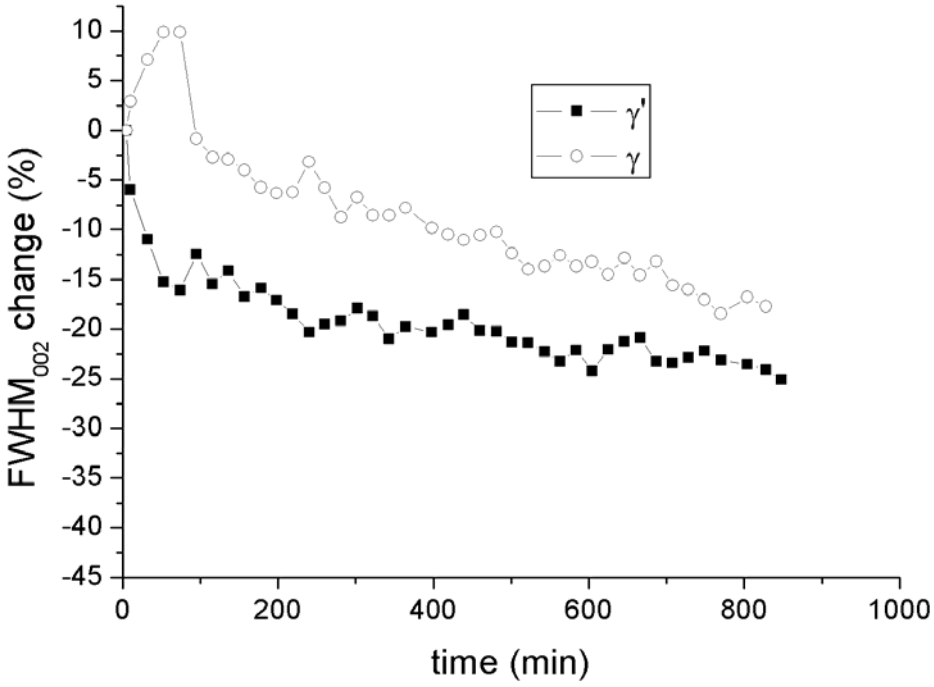

b) 002 reflection

Figure 3.22: Evolution of the FWHM change in the samples deformed at 0.6% plastic strain and annealed at 1100°C (samples 3 and 4)

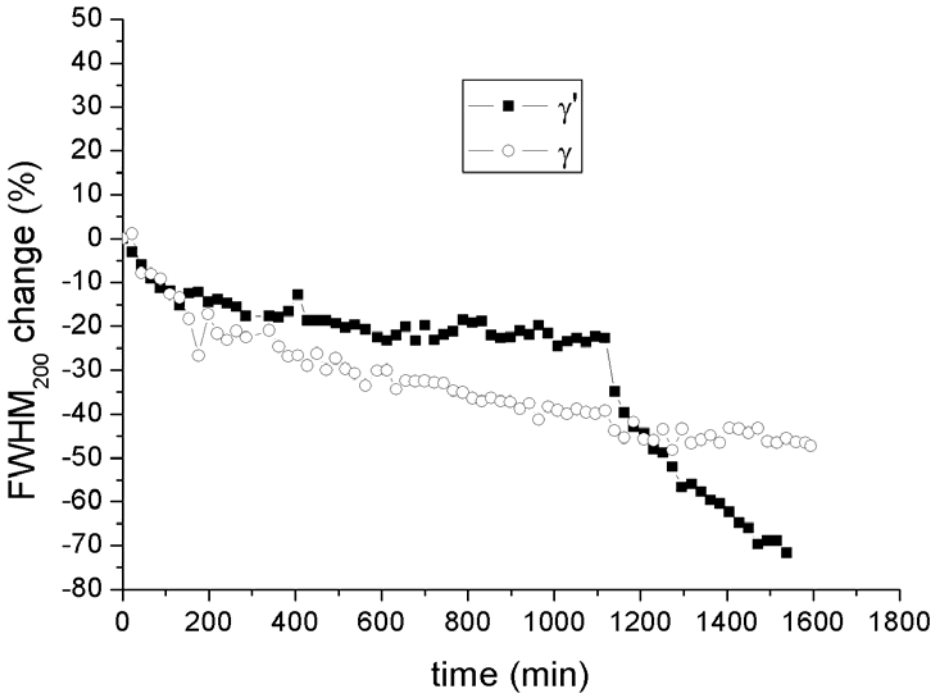

a) 200 reflection

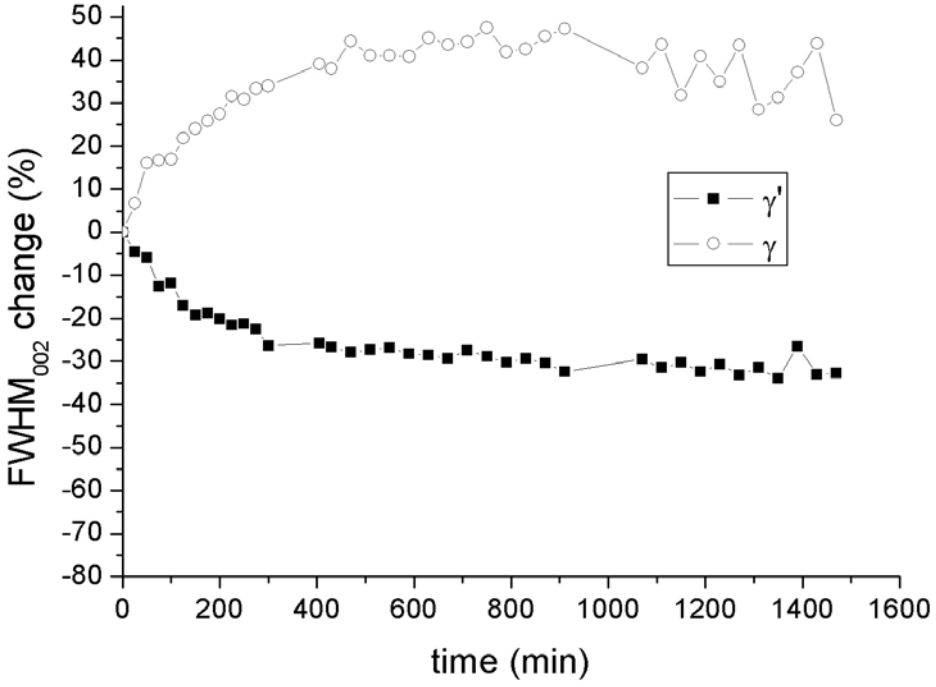

c) 002 reflection

Figure 3.23: Evolution of the FWHM change in the samples deformed at 0.6% plastic strain and annealed at 1050°C (samples 5 and 6)

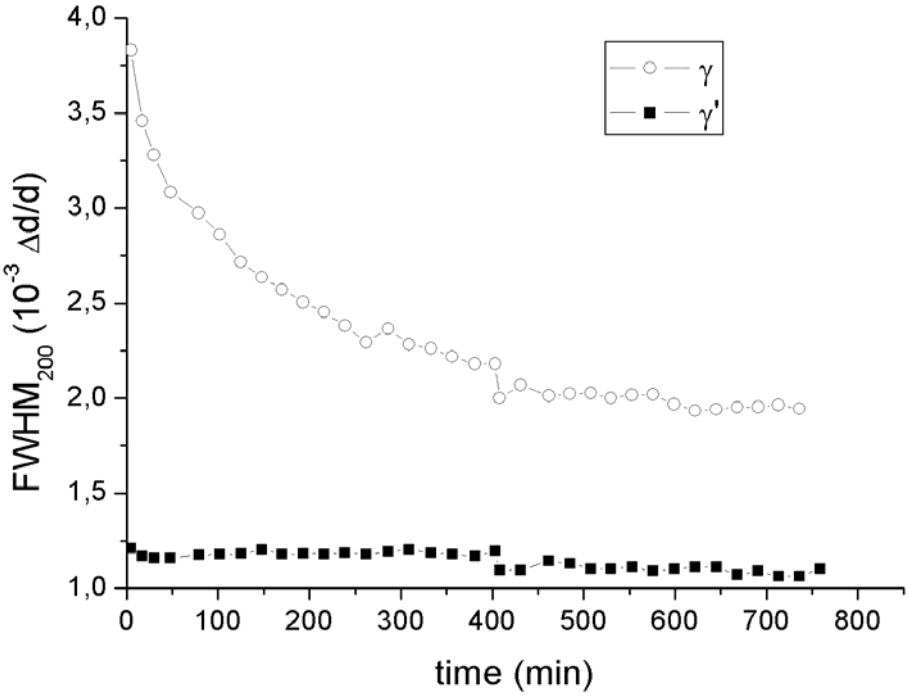

a) 200 reflection

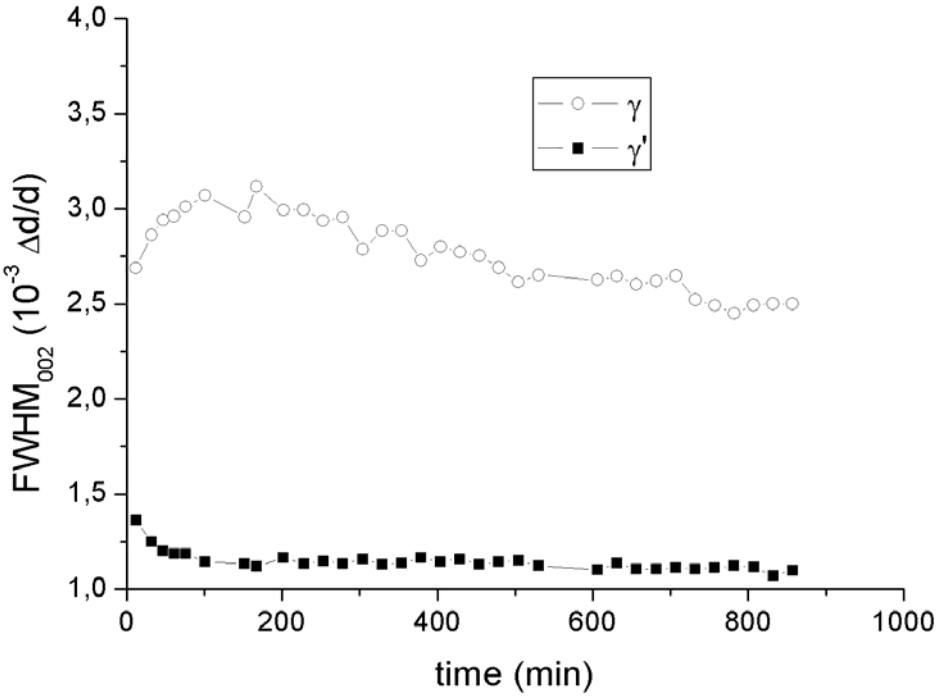

b) 002 reflection

Figure 3.24: Evolution of the FWHM in samples 1 and 2 (0.2% plastic strain-annealing at 1100°C)

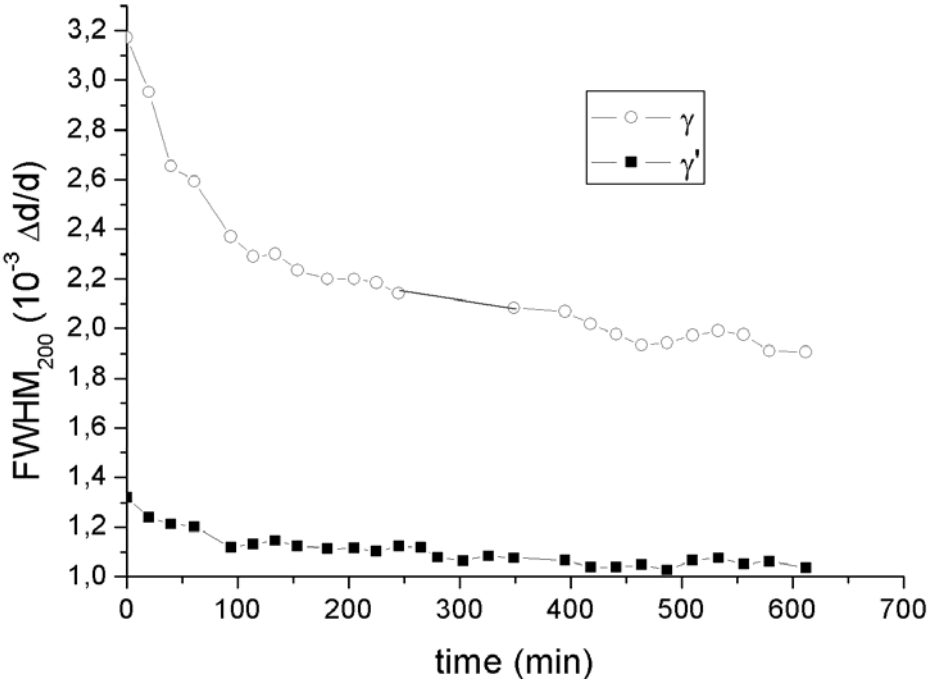

a) 200 reflection

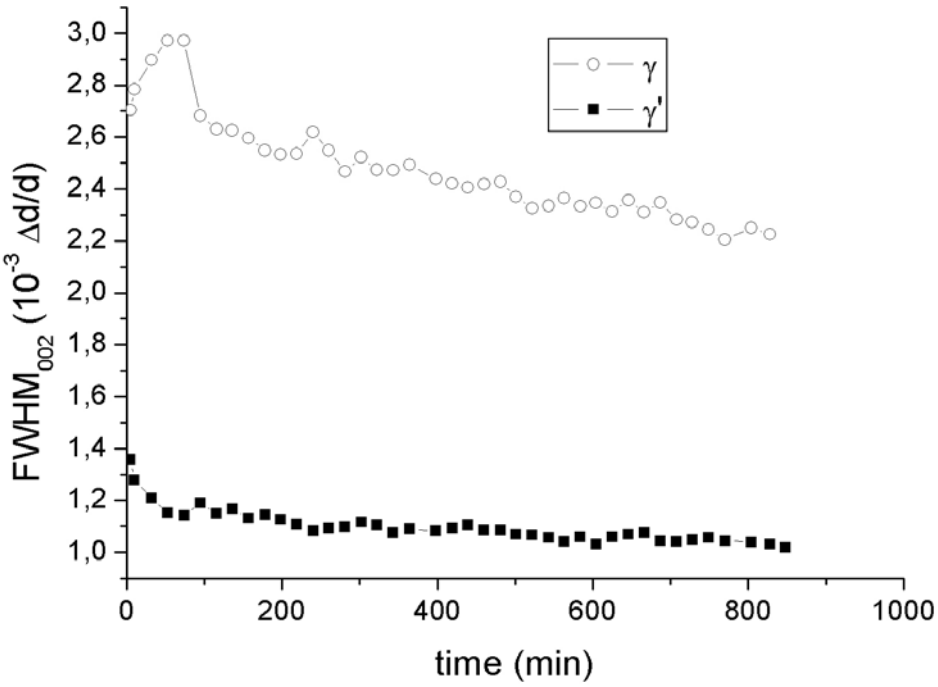

b) 002 reflection

Figure 3.25: Evolution of the FWHM in samples 3 and 4 (0.6% plastic strain-annealing at 1100°C)

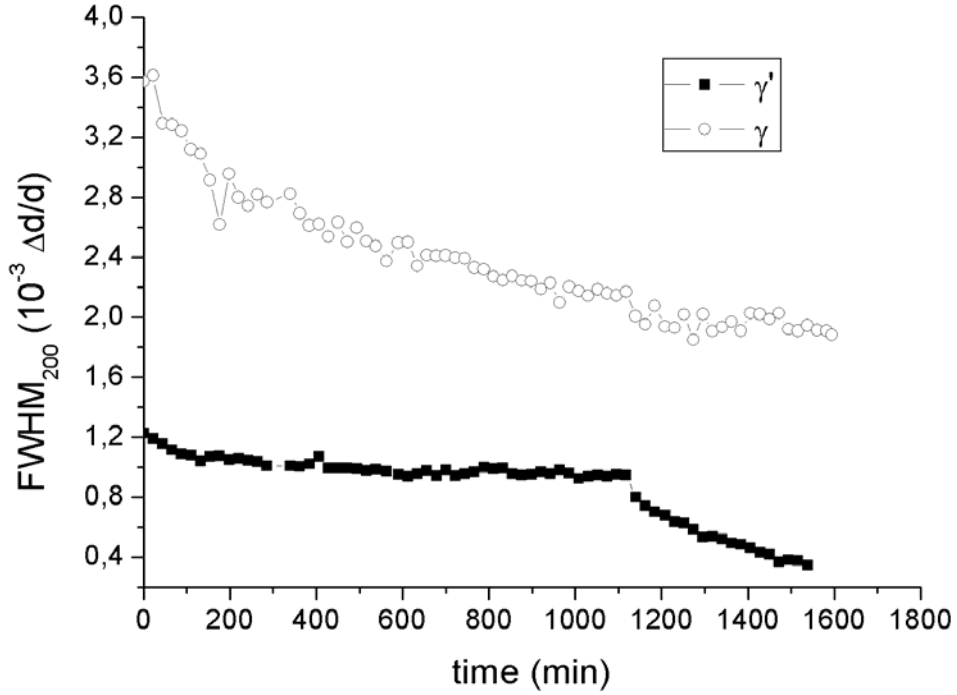

a) 200 reflection

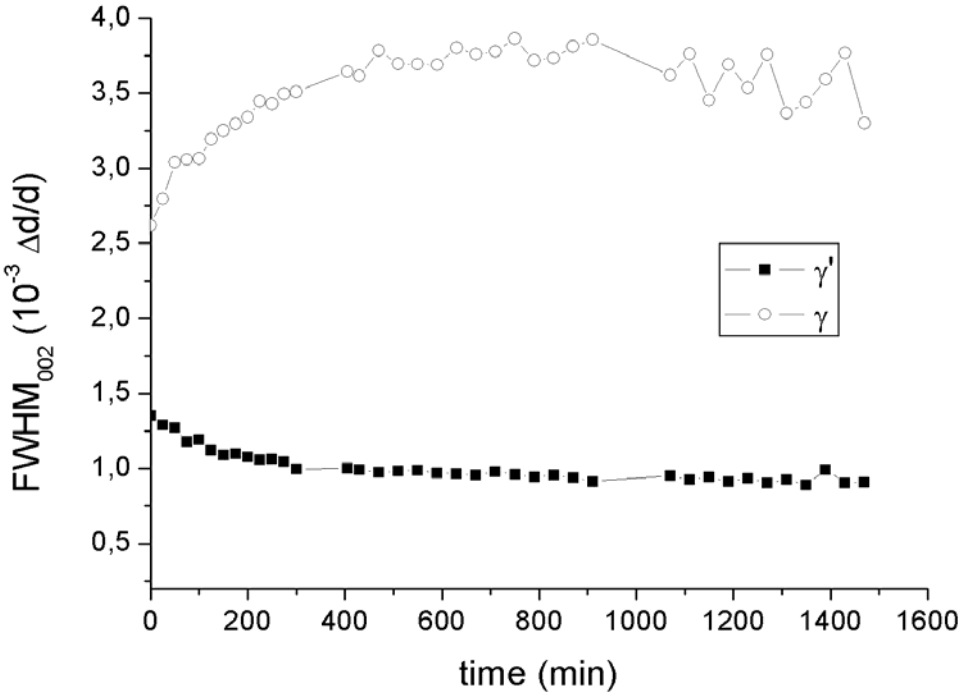

b) 002 reflection

Figure 3.26: Evolution of the FWHM in samples 5 and 6 (0.6% plastic strain-annealing at 1050°C)

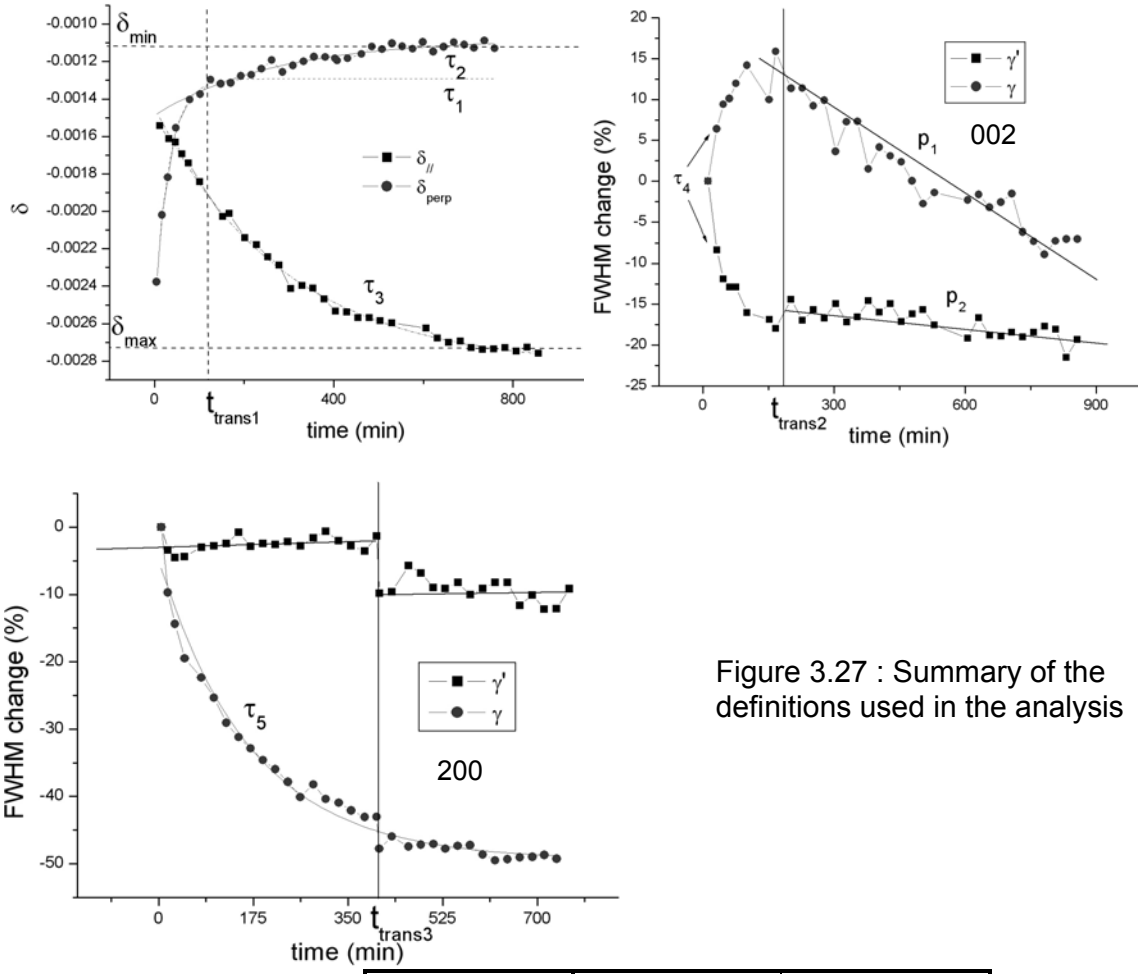

Figure 3.27 : Summary of the definitions used in the analysis

	SAMPLES 1&2	SAMPLES 3&4	SAMPLES 5&6
STRAIN	0.2%	0.6%	0.6%
AGEING T°C	1100°C	1100°C	1050°C
τ_1 (min.)	30	52	τ=533
τ_2 (min.)	269	228	
t_{trans1} (min.)	148	89	NA
τ_3 (min.)	288	195	676
δ_{min} (%)	-0.11	-0.22	-0.24
δ_{max} (%)	-0.27	-0.27	NA
τ_4 (min.)	41.32	21.8	207
p_1 (10^{-3} min.$^{-1}$)	-0.8	-21	-16
p_2 (10^{-3} min.$^{-1}$)	-0.08	-11	-3
t_{trans2} (min.)	152	84	910
τ_5 (min.)	173	106.8	631
t_{trans3} (min.)	405	NA	1118

Table 3.2 : Results obtained after fitting on the investigated samples

At an annealing temperature of 1100°C, the evolution of the lattice parameter mismatch perpendicular to the deformation axis is decomposed into two regimes. This point is also visible on the evolution of the FWHM of the 002 reflections from γ and γ' phases. In other words, the evolution of $\delta_{\perp}$ is correlated to the lattice parameter distribution in the 001 crystallographic direction in both phases. This point is supported by the fact that the time t_{trans1}, at which the evolution of $\delta_{\perp}$ is marked by a regime change, is very close to the time t_{trans2} at which the evolution of the FWHM change becomes linear. Comparing samples 1 and 2 with samples 3 and 4, it appears that the value of the transition time between the two regimes strongly depends on the amount of plastic strain that was formerly introduced in the specimen. Indeed, for a given annealing temperature (here 1100°C), a higher amount of plastic strain induces a lower transition time. Moreover, as mentioned before, the value $\delta_{\min}$, at which the apparent misfit perpendicular to the elongation axis is fixed at the end of the rafting process, also depends on the amount of plastic strain formerly introduced in the specimen.

On the other hand, it must be pointed out that the annealing temperature strongly influences the internal stress relaxation process that accompanies strain induced rafting. As can be expected from diffusion controlled phenomena, the higher the temperature, the faster the diffusion processes. However, in this particular case, the behaviour of the lattice parameter misfit relaxation is very different between 1050°C and 1100°C. In this temperature range, the γ' volume fraction, as well as the lattice parameter mismatch, decrease with increasing temperature. As was discussed in Chapter 1, the solutionising of γ' forming elements into the γ matrix induces a decrease (increase in absolute value) in the lattice parameter mismatch. Moreover, from a microstructure point of view, the dissolution of the γ' phase induces an increase in the width of the γ channels, leading to a decrease in the Orowan stress. From this point of view, the dislocation propagation is enhanced by a low γ' volume fraction (*i.e.* at high temperature) in addition to enhanced diffusion.

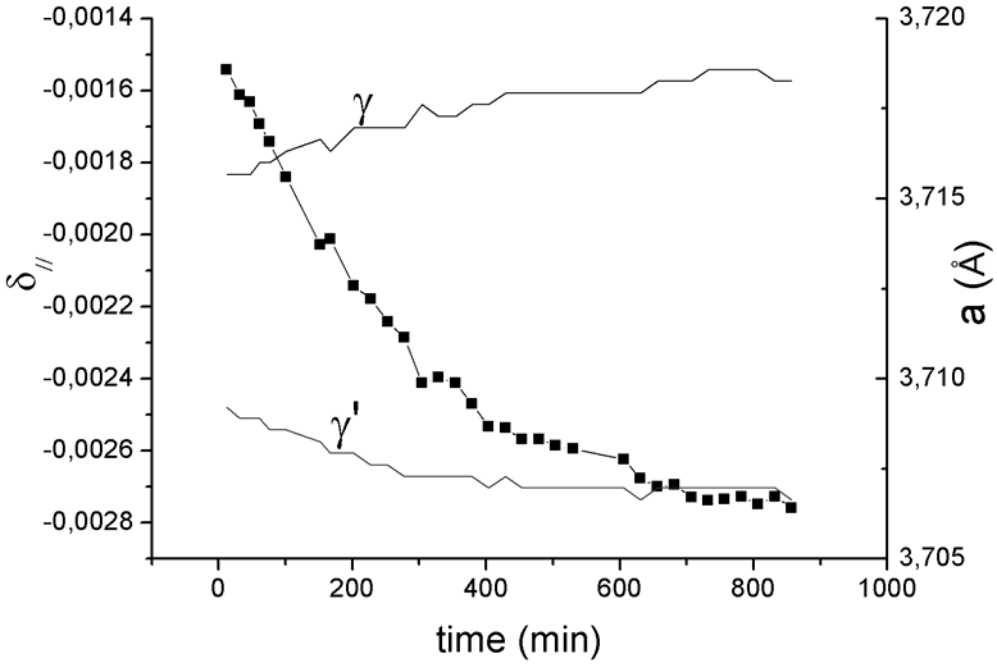

a) 002 reflection

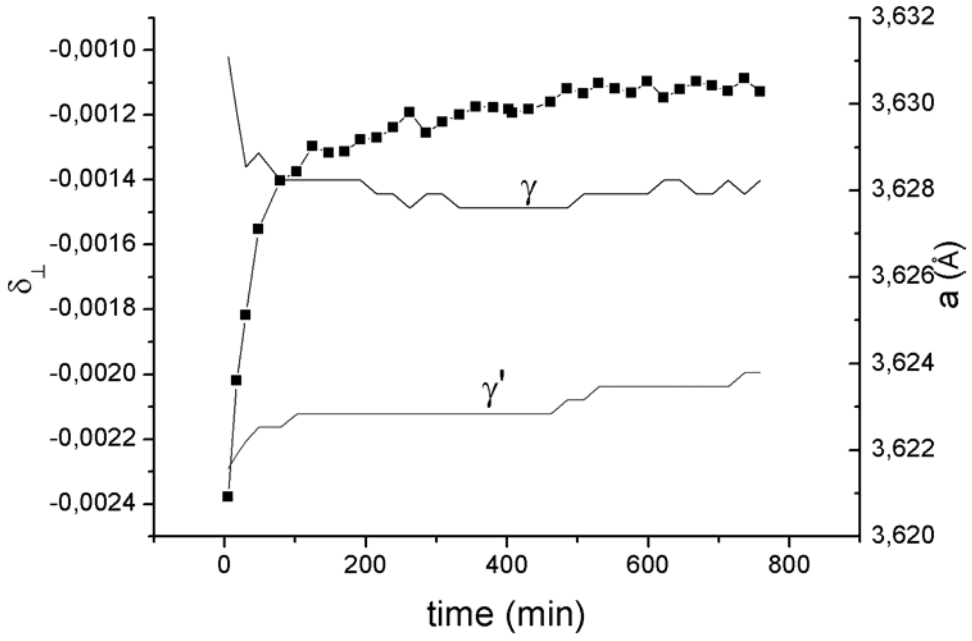

b) 200 reflection

Figure 3.28: Evolution of the lattice parameters of γ and γ' phases with annealing time in the samples deformed at 0.2% and annealed at 1100°C (samples 1&2)

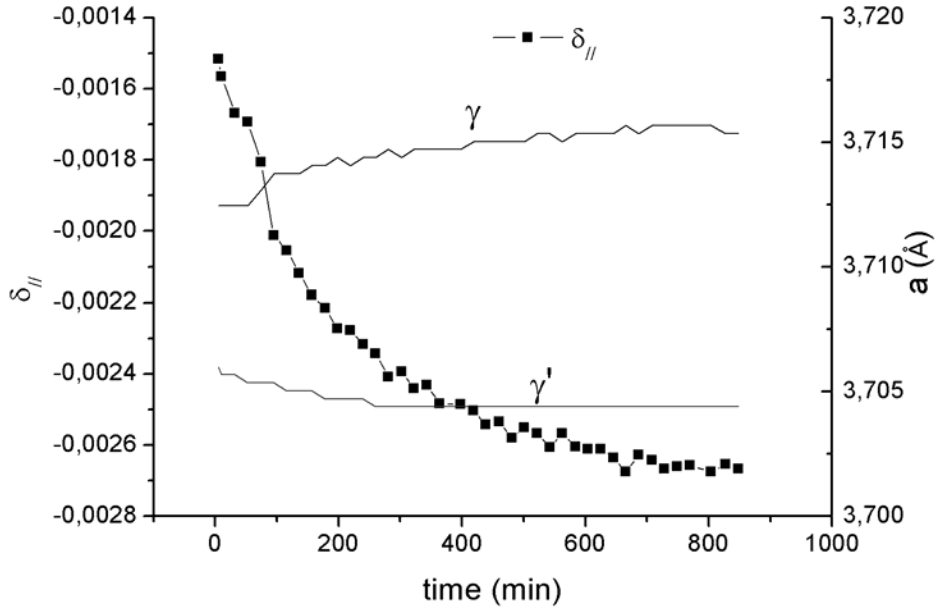

a) 002 reflection

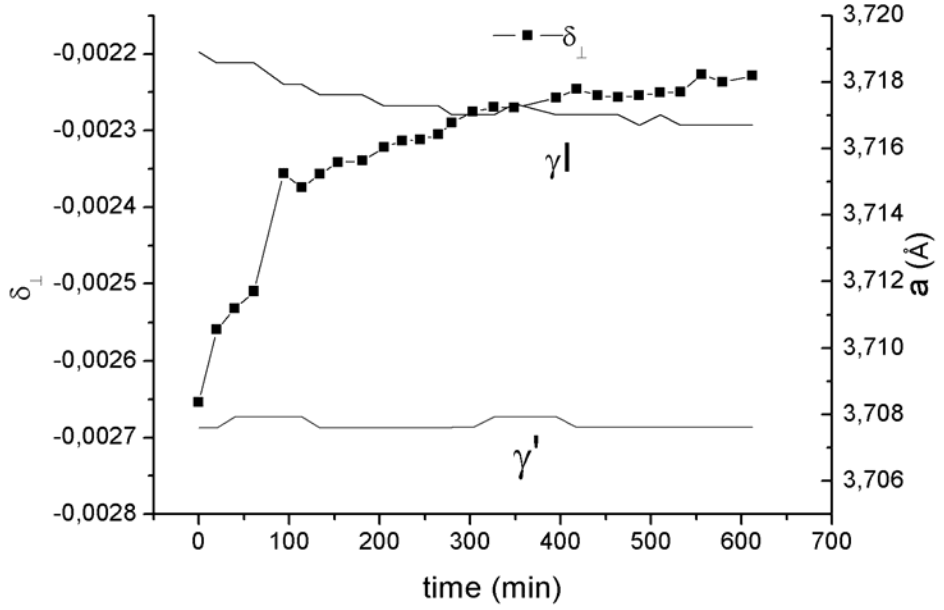

b) 200 reflection

Figure 3.29: Evolution of the lattice parameters of γ and γ' phases with annealing time in the samples deformed at 0.6% and annealed at 1100°C (samples 3&4)

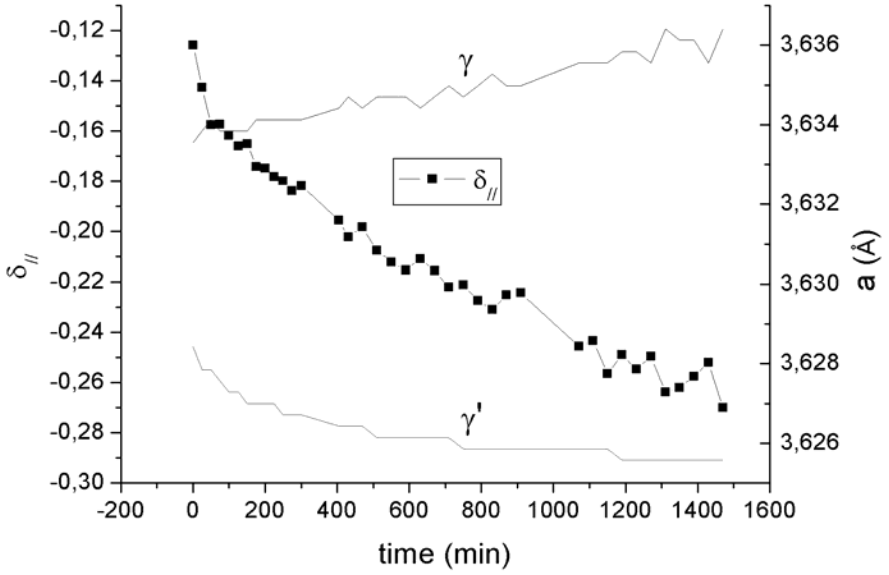

a) 002 reflection

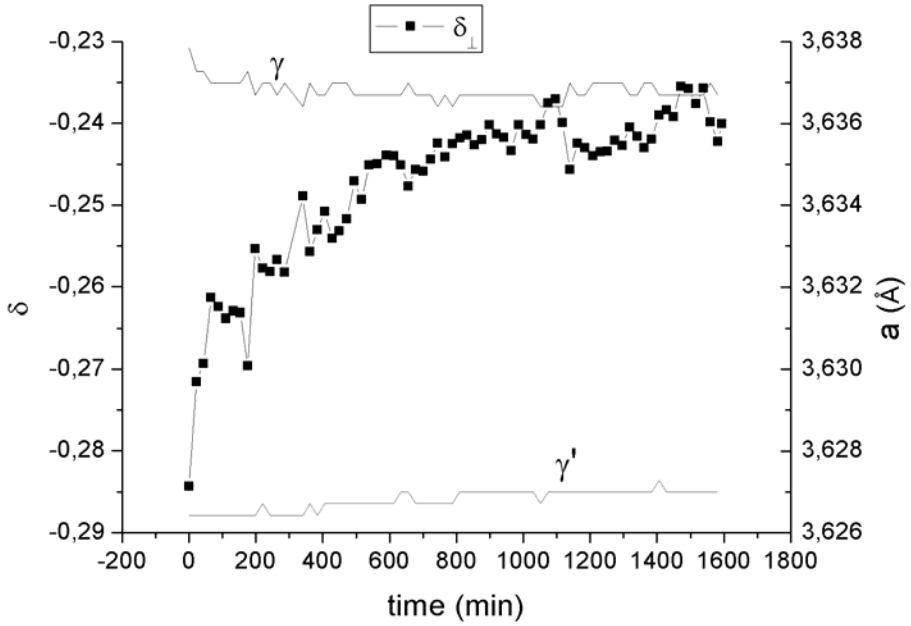

b) 200 reflection

Figure 3.30: Evolution of the lattice parameters of γ and γ' phases with annealing time in the samples deformed at 0.6% and annealed at 1050°C (samples 5&6)

Figures 3.28 to 3.30 show the time evolution of the lattice parameters of γ and γ' phases in each investigated sample. Each sample shows the same behaviour. The lattice parameters of both phases evolve together with the lattice parameter mismatch. This means that both phases experience the evolution of the γ/γ' interfacial stress field as rafting proceeds. Moreover, we can see that the evolution of the lattice parameters of γ and γ' phases is continuous in the case of the 002 reflection, as is that of the lattice parameter mismatch parallel to the deformation axis. The γ' lattice parameter decreases while the γ lattice expands in the 002 direction. Meanwhile, and as an application of the volume conservation rule, the γ' phase expands while the γ lattice shrinks in the 200 directions. The tetragonal distortion of the cubic lattices of γ and γ' phases was interpreted as the result of internal strain [36]. Furthermore, a fast evolution of the lattice parameters in the 200 direction is visible at the beginning of the ageing. This quick change is associated to the evolution of the lattice parameter mismatch, whose origin is believed to be induced by the rearrangement of interfacial dislocations into a more periodic pattern. The mechanisms involved in the lattice parameter mismatch relaxation are discussed in detail in Chapter 5.

III.4 Investigation of the dislocation structure evolution during strain induced rafting

The dislocation structure before and after strain induced rafting was investigated by transmission electron microscopy. Thin samples were cut perpendicular to the [001] axis in the samples in which 0.6% of plastic strain was introduced at 850°C. At this temperature, plastic deformation is homogeneous (see section I.2.4). Two thin foils were prepared according to the method described in section II.1.2. Sample 1 was cut prior to the high temperature annealing during which rafting occurs and sample 2 after the high temperature annealing (15 hours-1100°C). We therefore observed the dislocation structure resulting from plastic deformation and the dislocation structure after rafting. This allowed the identification of the dislocation reactions occurring during strain induced rafting.

Figure 3.31 shows the dislocation structure observed in sample 1, after plastic deformation is introduced. The microstructure is constituted by cuboidal γ' particles. We can see that the 001 γ/γ' interface is covered by two types of dislocation lines, which were created during the deformation process. The same sample area was observed under different diffraction conditions in order to identify the Burgers vectors $\vec{b}$ and the line direction u of the observed dislocations (see section II.1.2). The same procedure was applied for the sample that was observed after the high temperature annealing (after rafting). The dislocation structure after rafting is shown in Figure 3.32. Schematic views are shown in Figure 3.33 for clarity.

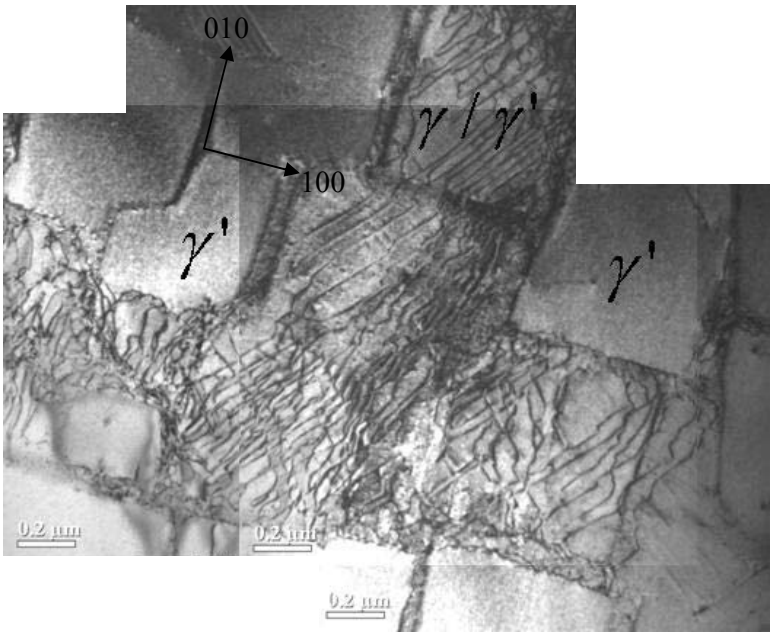

Figure 3.31: Dislocation structure observed in a MC-NG sample deformed at 850°C at 0.6% of plastic strain (sample 1): $\vec{g} = 0\bar{2}0$

During plastic deformation at 850°C, the plastic deformation is homogeneous in the material and confined in the matrix. As mentioned in Chapter 1, the shearing of a γ' particle does not occur. Furthermore, the presence of a negative lattice parameter mismatch should promote plastic deformation in horizontal channels. In other words, the horizontal γ channels contain more dislocations than the vertical channels, in terms of density. A detailed discussion of this phenomenon is conducted in Chapter 4. The interface observed in Figure 3.31 corresponds to the interface between horizontal matrix channels and precipitates. The dislocations generated during plastic

deformation result from the activation of at least two {111} glide planes. This is typical of a fcc lattice. Figure 3.32 shows that after high temperature annealing, during which rafting occurs; a third type of dislocation appears. The calculation of the Schmid factor for this type of dislocation (type c) gives zero. This means that this type of dislocation can not have appeared during the introduction of plastic deformation in the specimen. It has therefore appeared through a reaction between the two types of dislocations that were created during plastic deformation. This reaction can be written as follows

$$\frac{a}{2}\langle 10\bar{1}\rangle + \frac{a}{2}\langle 011\rangle \rightarrow \frac{a}{2}\langle 110\rangle \quad (3.2)$$

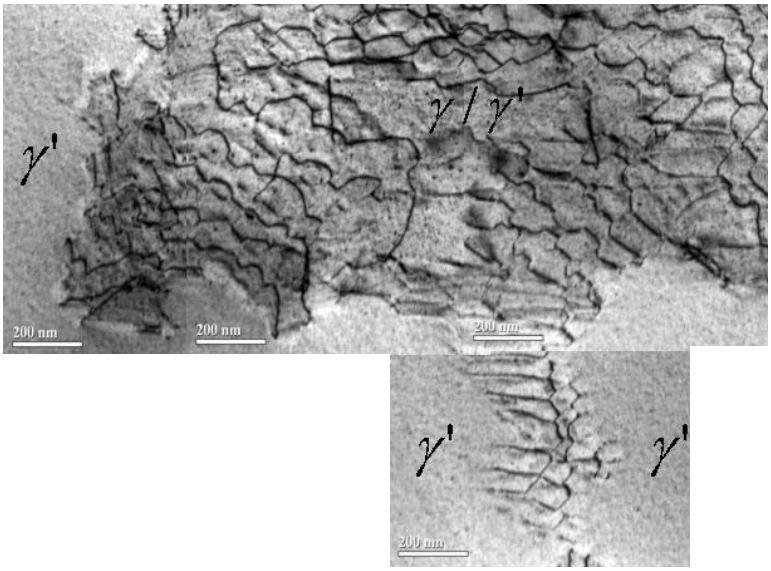

Figure 3.32: Dislocation structure observed in a MC-NG sample deformed at 850°C at 0.6% of plastic strain and annealed for 20 hours at 1100°C (sample 2): $\vec{g} = 111$

As rafting proceeds, interface dislocations combine to form a new type of dislocations and finally adopt a network structure. This network structure is similar to that observed during the early stages of a high temperature low stress creep test [1]. As the matrix plastic strain formerly introduced in the material increases, the dislocation network that forms during rafting becomes denser. This is confirmed by the differences in the $\delta_{\min}$ values observed between samples 1 (0.2% strain - annealing at 1100°C) and 3 (0.6% strain – annealing at 1100°C) in the previous section.

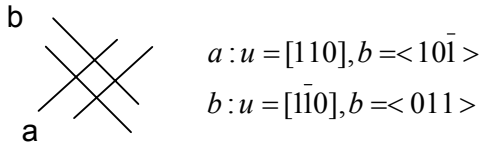

a)

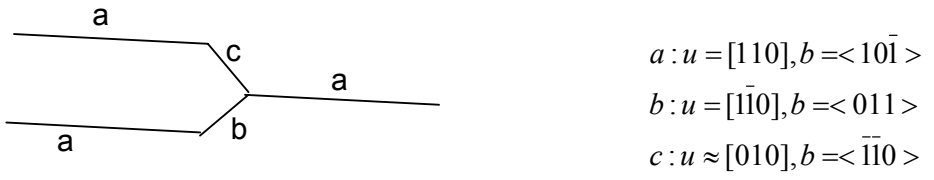

b)

Figure 3.33: Schematic representation of the dislocation structure observed in sample 1: a) before annealing and b) after annealing

III.5 SEM observations of the rafted microstructure

SEM observations were performed on samples 1 (0.2% plastic strain – 15 hours annealing at 1100°C) and 2 (0.6% plastic strain – 15 hours annealing at 1050°C) to directly compare the microstructure after rafting. The microstructures for samples 1 and 2 after high temperature annealing are shown in Figure 3.34 and 3.35 respectively. Sample 1 shows a rather irregular lamellar structure, when compared to that obtained in the AM1 alloy shown in Figure 3.36 [8]. Moreover, the γ' rafts look shorter in MC-NG than in AM1. In the case of sample 2, the γ' particles have a parallelepiped shape, indicating that particle coalescence took place. Moreover, the width of the vertical γ channels is very small compare to that of the horizontal channels. Nevertheless, the formation of the lamellar structure is not complete, most probably due to a short annealing time.

The analysis of the particle size distribution shows that the γ' particles essentially have the same geometry in both samples. The γ' mean area was determined to be 0.311μm^2 in sample 1 and 0.331μm^2 in sample 2. To see more clearly the influences of plastic strain, annealing temperature and time, a MC-NG

sample was deformed at 850°C until the amount of plastic strain reached 0.2%. This sample was then subsequently annealed at 1100°C for a very long time (around 90 hours). The SEM observation of this sample is shown in Figure 3.37. The lamellar structure looks similar to that observed in sample 1. The analysis of the particle size distribution gives a γ' mean area around 0.584 μm^2. The annealing time seems to play a very important role in the resulting size of γ' precipitates in strain induced rafting. This result could indicate that the rafting was not complete at the end of the SANS experiments shown in section III.2.1, although the signal evolution was extremely slow at the end of the in-situ ageing. From these observations, no conclusion can be drawn on the influence of the amount of plastic strain, annealing temperature and time. In all cases, the γ channel width is bigger when the γ' particles have a raft shape than when they are cuboidal. This point is clearly visible when comparing Figure 3.9a with Figures 3.34 and 3.35.

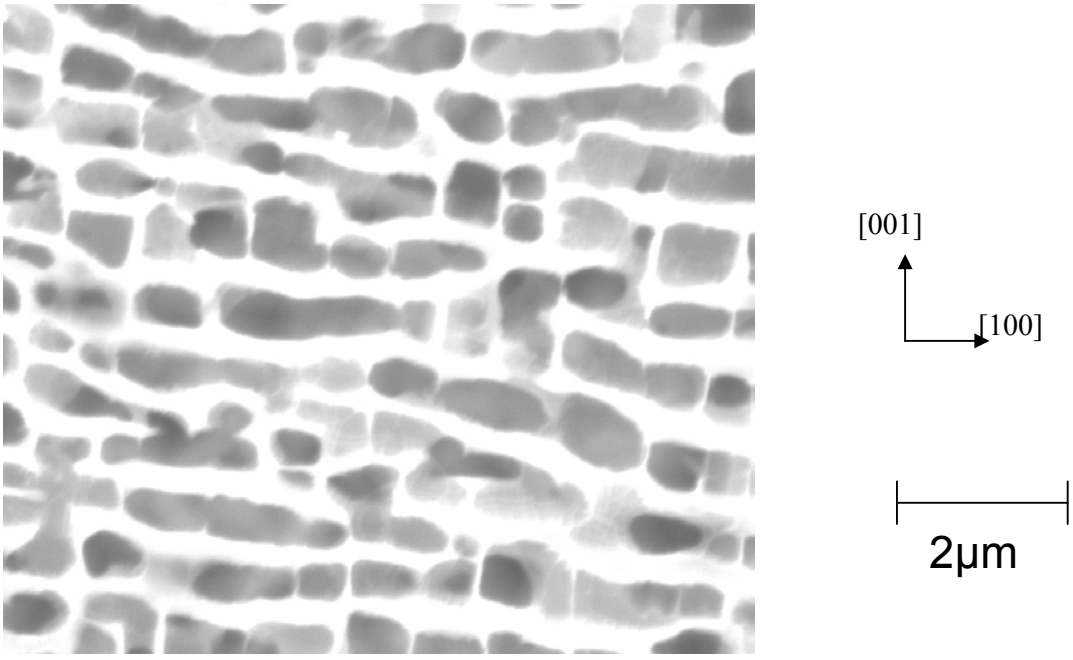

Figure 3.34: Microstructure of MC-NG after introduction of 0.2% plastic strain at 850°C and subsequent annealing at 1100°C for 20 hours (sample 1) (white: γ, black: γ').

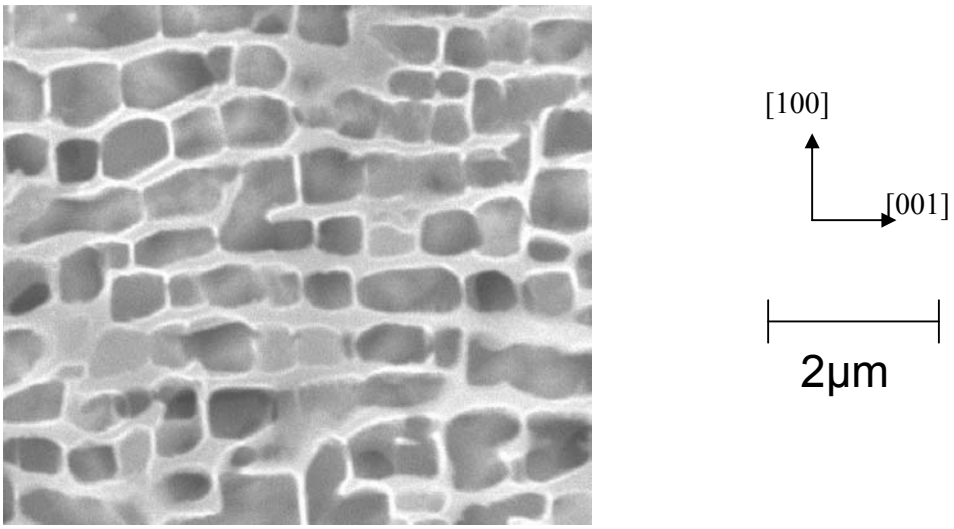

Figure 3.35: Microstructure of MC-NG after introduction of 0.6% plastic strain at 850°C and subsequent annealing at 1050°C for 15 hours (sample 2). (black: γ', white: γ)

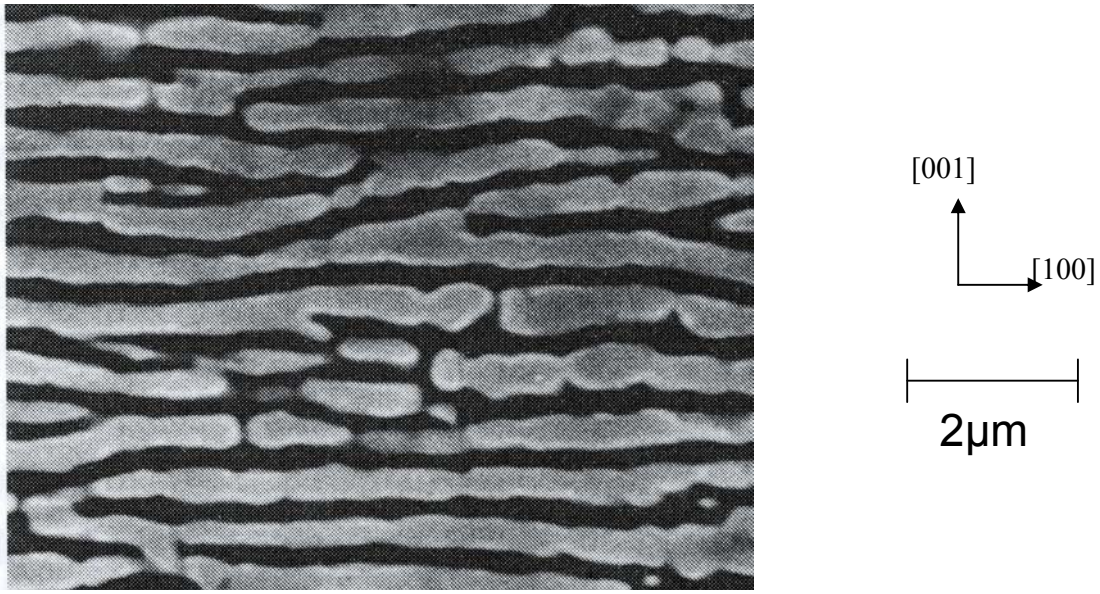

Figure 3.36: Microstructure of AM1 after introduction of 0.2% plastic strain and subsequent annealing at 1050°C for 10 hours (white: γ', black: γ) as from [8]

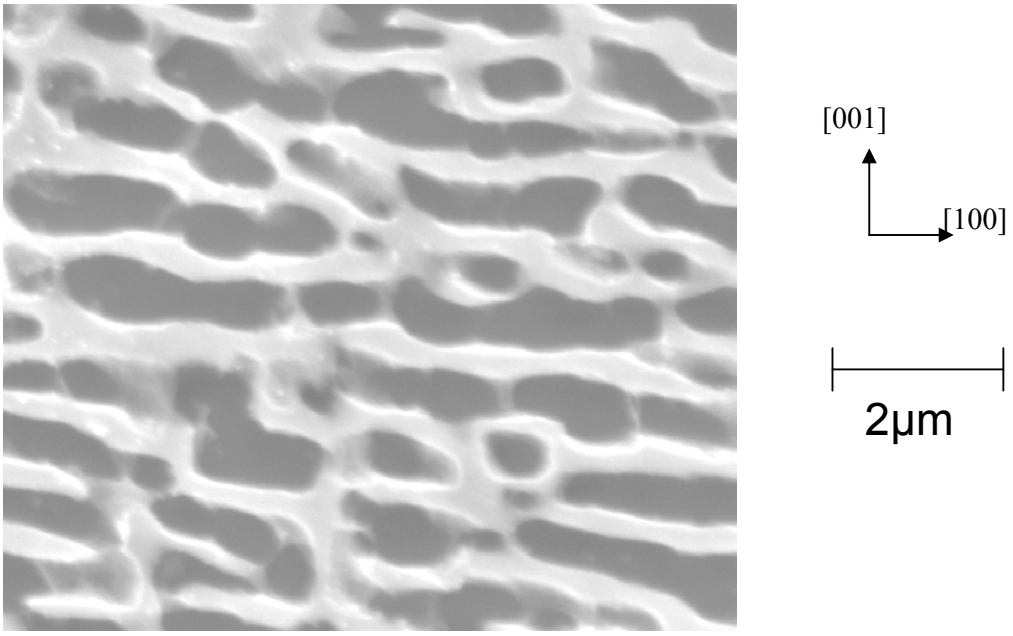

Figure 3.37: Microstructure of MC-NG after introduction of 0.2% plastic strain at 850°C and subsequent annealing at 1100°C for 90 hours. (white: γ, black: γ')

Figure 3.38 shows the rafted microstructure observed after a creep test performed at 1100°C with a 150MPa tensile load applied along the [001] axis in a MC-NG specimen. The creep test was interrupted after 20 hours. In such conditions, rafting of γ' particles has occurred perpendicular to the stress axis. The analysis of the particle size distribution gives a mean area around 10.9µm^2. The final particle size and the γ channel width are therefore much bigger when rafting occurs during a creep test. The possible origins for such a difference will be discussed in more details in Chapter 5. We can anticipate here that the continuous increase in the amount of plastic strain which occurs during rafting plays an essential role. Moreover, the temperature at which plastic deformation is introduced in the case of a creep test (1100°C) is very different from that used in strain induced rafting (850°C). The mechanisms involved in the development of the plastic flow in the material might differ.

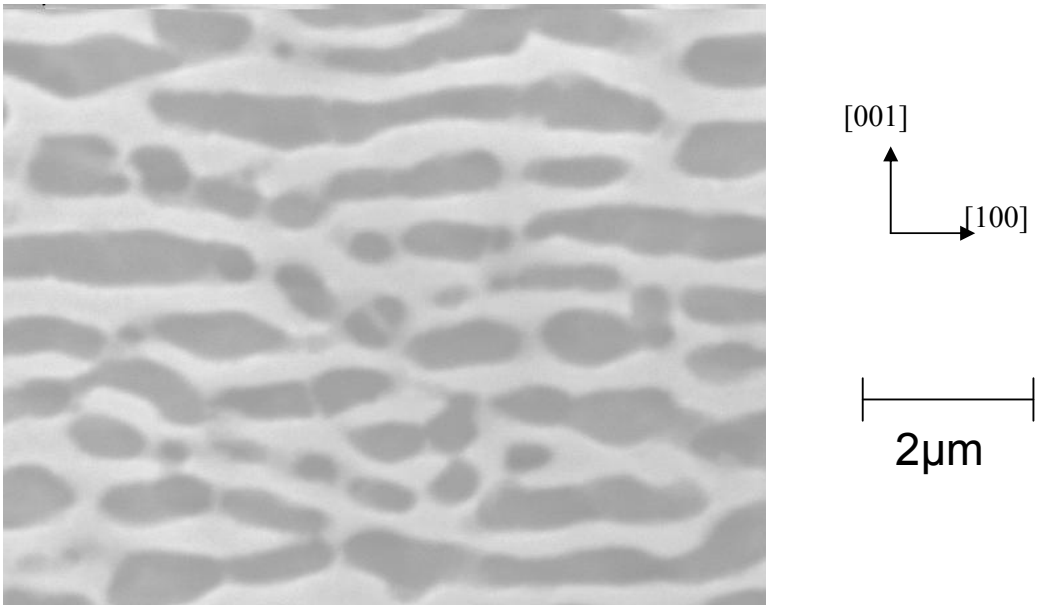

Figure 3.38: Microstructure of MC-NG after 20 hours of creep at 1100°C-150MPa (black: γ', white: γ)

Figure 3.39 shows the microstructure of a sample that was deformed at 850°C until the amount of plastic strain reaches 0.6%, and then annealed during 24 hours at 1050°C. This figure is to be compared with Figure 3.35, for which the annealing time is 15 hours. In the case of a long annealing time (24 hours), the microstructure is lamellar and rafting seems to be complete; while a short annealing time (15hours) leads to a microstructure constituted with big parallelepiped particles. This phenomenon can be related to the evolution of the FWHM of the 200 reflection of the γ' phase during high temperature annealing. The latter can be decomposed into two domains, as shown in Figure 3.21a) and 3.23a). In each domain the FWHM remains constants. The transition between these two domains (t_{trans3}) consists in a drop of the 200 γ' FWHM, which can be associated with a coherency loss of the γ' phase with the γ matrix. As mentioned before, this point is not visible in samples 3 and 4 (0.6% plastic strain – 15hours annealing at 1100°C), as the experiment was interrupted for a long time due to instrument issues. A possible explanation for this phenomenon can be that two adjacent cuboidal particles coalesce along the [100] axis to form a larger particle, as it clearly appears from the SEM observations that the particle shape is rather cuboidal before the FWHM drop, and that the microstructure becomes lamellar after this drop. The presence of the drop in γ' FWHM would be associated with the coalescence of at least two adjacent cuboidal particles.

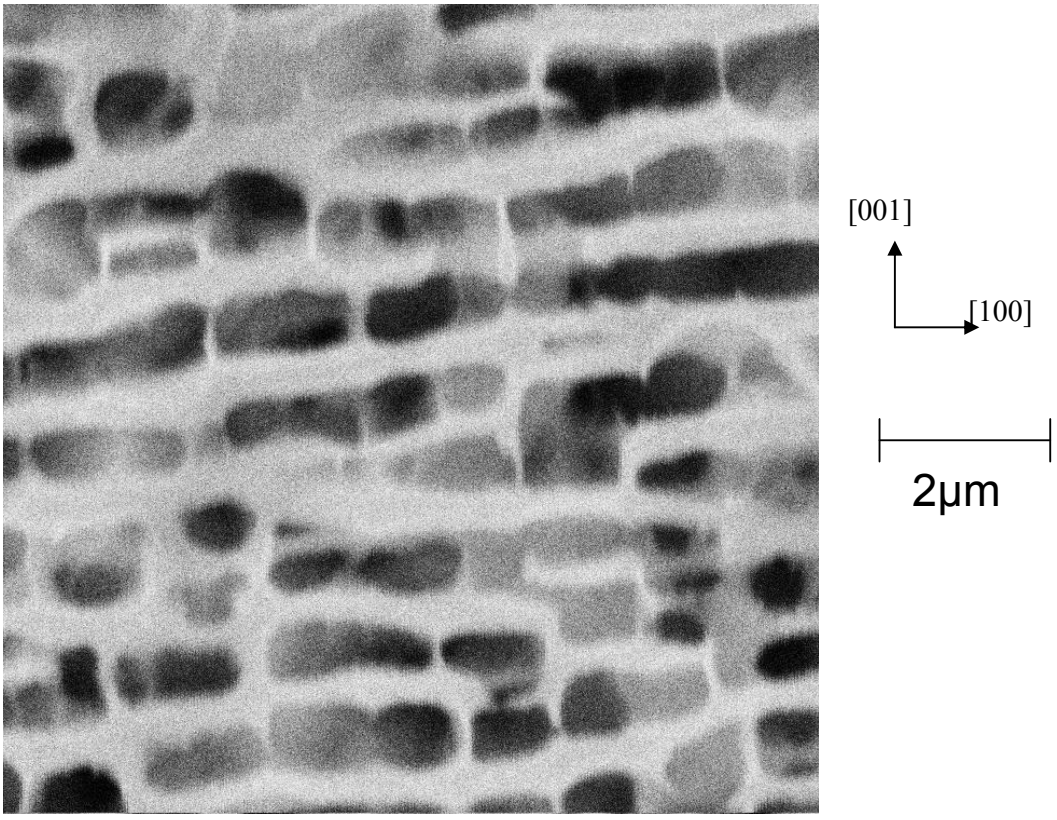

Figure 3.39: Microstructure of MC-NG after introduction of 0.6% plastic strain at 850°C and subsequent annealing at 1050°C for 24 hours (sample 2). (black: γ', white: γ)

III.5 Conclusion

From a microstructure point of view, the SEM observations as well as the SANS investigations have shown that, after homogenisation heat treatment, the γ' particle size is smaller in the third generation MC-NG superalloy than in the first generation AM1 alloy. Moreover, the shape of the γ' particles is not identical in both alloys. The edges of the cuboidal particles are sharper in the MC-NG than in the AM1. Another striking feature is the homogeneity of plastic deformation. As was discussed in Chapter 1, plastic deformation in MC-NG is heterogeneous at room temperature whereas it is uniform in the AM1. The short range order that exists in the MC-NG γ matrix is partially responsible for this discrepancy. However, as this short range order disappears at high temperature (around 850°C), plastic deformation can be uniformly introduced in MC-NG samples. During further annealing at high temperature (above

1050°C), a lamellar microstructure is formed. In the MC-NG alloy, the γ' rafts are shorter and show a less regular arrangement than in the AM1 alloy.

From a kinetics point of view, we have observed two different rafting behaviours at the two investigated temperatures (1050°C and 1100°C). In terms of microstructure evolution, strain induced rafting at 1050°C is a slow and continuous process, while the morphology change is complete after several hours of annealing at 1100°C. As expected, the evolution of the apparent lattice parameter mismatch is anisotropic. The apparent mismatch perpendicular to the elongation axis decreases, while that parallel to the deformation axis increases. Moreover, we have seen that the relaxation of $\delta_{\perp}$ can adopt different behaviours depending on the annealing temperature. At 1050°C, the misfit relaxation is continuous, while it can be decomposed into two regimes at 1100°C. It must be emphasised that interface dislocation density remains constant as rafting proceeds. However, the directional coarsening process is accompanied by the formation of an interface dislocation network, similar to that observed after a creep test. In all cases, it was shown that plastic strain induces rafting and enhances the associated diffusion processes. Many parameters, such as γ' volume fraction, plastic strain and width of the γ channels may influence the rafting behaviour. The influence of each parameter is discussed in details in Chapter 5.

CHAPTER 4 Elasticity Analysis

In this chapter, the strain induced rafting phenomenon is analysed using the Eshelby inclusion theory. Anisotropic elasticity combined with the mean field approach has been used. The principles of the inclusion theory and mean field approach are briefly reviewed and a formulation of the elastic energy is obtained. This model is then applied to single crystal nickel based superalloys, and more particularly to the strain induced rafting phenomenon of γ' particles, stressing the emphasis on the role of precipitation misfit and plastic strains in this particle morphology evolution. The mechanisms involved in the early stages of plastic deformation are discussed. Finally, a correlation with the high temperature creep behaviour of nickel superalloys is proposed.

IV.1 Inclusion theory and mean field approach

IV.1.1 Single inclusion problem

In the case of a uniform body, the stress tensor $\boldsymbol{\sigma}$ can be evaluated using Hooke's law:

$$\sigma_{ij} = C_{ijkl}\varepsilon_{kl} \qquad (4.1)$$

where $\mathbf{C}$ is the stiffness tensor and $\boldsymbol{\varepsilon}$ the elastic strain tensor. This expression holds when the stiffness and strain tensors are uniform through the whole body. In many cases, such as composite materials or precipitate hardened materials, the presence of misfitting and/or inhomogeneous inclusions does not allow the direct use of Hooke's law. The inclusion theory developed by Eshelby [85] in the case of uniform and isotropic elasticity proposes an alternative approach to solve the problem. We consider a uniform body (D) that contains a misfitting inclusion (Ω), as schematically shown in Figure 4.1. The stress free transformation strain or eigenstrain in the inclusion (Ω) is designated as $\boldsymbol{\varepsilon}^*$ and is supposed to be uniform inside the particle. This eigenstrain, or intrinsic strain, corresponds, for instance, to the precipitation

misfit strain (lattice parameter mismatch) or dilatation strain when matrix and inclusion do not have the same thermal expansion coefficients. The presence of this eigenstrain induces a homogeneous stress field inside the inclusion. The stress inside an ellipsoidal inclusion is then calculated to be

$$\sigma_{ij} = C_{ijkl}(\gamma_{kl} - \varepsilon^*_{kl}) \quad (4.2)$$

where $\boldsymbol{\gamma}$ is the total strain tensor that depends on the shape of the inclusion. In the frame of the inclusion theory and in the case of a homogeneous ellipsoidal inclusion, the total strain $\boldsymbol{\gamma}$ is expressed as:

$$\gamma_{ij} = S_{ijkl}\varepsilon^*_{kl} \quad (4.3)$$

where $\mathbf{S}$ is the Eshelby tensor, that depends on the shape of the inclusion. The definition of the Eshelby tensor is given in Mura's book, p.135 [86].

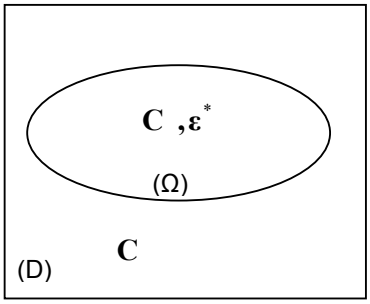

Figure 4.1: Schematic view of a uniform body containing an ellipsoidal inclusion

The inclusion theory was then extended later to the case of inhomogeneous inclusion of anisotropic elasticity. In this case, we consider a body (D) that contains an inhomogeneous inclusion (Ω). We designate $\mathbf{C}$ and $\mathbf{C}^*$ as the elastic constants of the matrix (M=D-Ω) and of the inhomogeneous inclusion (Ω) respectively ($C \neq C^*$). As shown in Figure 4.2, the inhomogeneous inclusion of eigenstrain $\boldsymbol{\varepsilon}^*$ can be equivalently replaced by a homogenous inclusion of equivalent eigenstrain $\boldsymbol{\varepsilon}^{**}$. The equivalent eigenstrain is calculated through the equivalency condition that claims that the stress inside the inclusion is equal in both cases, and that total strain in both cases account for the elastic inhomogeneity effect, *i.e.*

$$\boldsymbol{\sigma} = \mathbf{C}^*(\mathbf{S}\boldsymbol{\varepsilon}^{**} - \boldsymbol{\varepsilon}^*) = \mathbf{C}(\mathbf{S}\boldsymbol{\varepsilon}^{**} - \boldsymbol{\varepsilon}^{**}) \quad (4.4)$$

We thus obtain the following expression

$$\boldsymbol{\varepsilon}^{**} = \left\{(\mathbf{C}^* - \mathbf{C})\mathbf{S} + \mathbf{C}\right\}^{-1}\mathbf{C}^*\boldsymbol{\varepsilon}^* \quad (4.5)$$

By inserting the expression of the equivalent eigenstrain (equation 4.5) into equation (4.4), the actual stress inside a particle is evaluated. The elastic energy assigned to a unit volume of particle is then calculated as the half product of stress and eigenstrain (the product implies summation over repeated indices).

$$W = -\frac{1}{2}\sigma_{ij}\varepsilon_{ij}^{*} \quad (4.6)$$

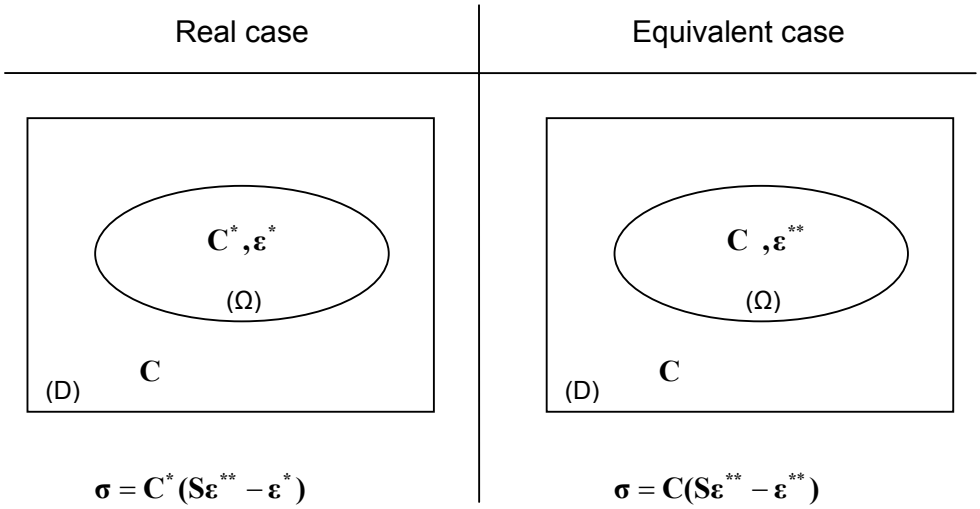

Figure 4.2: Eshelby's equivalency condition for an inhomogeneous ellipsoidal inclusion

IV.1.2 Mean field approach

As nickel superalloys contain a high volume fraction of misfitting particles, the interactions term between particles in terms of stress can not be neglected. The mean field approach is used to account for these interactions. We consider a body (D) having a large volume fraction f of ellipsoidal inclusions (Ω). The average stress field in the particles is designated as $\langle\boldsymbol{\sigma}\rangle_{\Omega}$. The interactions between the particles result in a homogeneous average stress field $\langle\boldsymbol{\sigma}\rangle_{M}$ in the matrix (M=D-Ω). The stress balance condition imposes

$$f\langle\boldsymbol{\sigma}\rangle_{\Omega} + (1-f)\langle\boldsymbol{\sigma}\rangle_{M} = 0 \quad (4.7)$$

The stress induced by the addition of another (inhomogeneous) ellipsoidal single inclusion of (equivalent) eigenstrain $\boldsymbol{\varepsilon}^{**}$ is $\boldsymbol{\sigma}^{\infty}$ and is calculated to be

$$\boldsymbol{\sigma}^{\infty} = \mathbf{C}(\mathbf{S}\boldsymbol{\varepsilon}^{**} - \boldsymbol{\varepsilon}^{**}) \qquad (4.8)$$

$$\boldsymbol{\varepsilon}_{\mathbf{int}} = \mathbf{C}^{-1}\langle\boldsymbol{\sigma}\rangle_{\gamma} = -f(\mathbf{S}-\mathbf{I})\boldsymbol{\varepsilon}^{**}$$

In these conditions the average stress inside the particles $\langle\boldsymbol{\sigma}\rangle_{\Omega}$ is not modified and is the sum of the average stress due to particle interactions $\langle\boldsymbol{\sigma}\rangle_{M}$ and of the stress induced by the addition of the new particle σ^{∞}. We then obtain the following equation [87]

$$\boldsymbol{\sigma}^{\infty} + \langle\boldsymbol{\sigma}\rangle_{\mathbf{M}} = \langle\boldsymbol{\sigma}\rangle_{\boldsymbol{\Omega}} \qquad (4.9)$$

Combining equations (4.7) and (4.9), the following expressions for the average stress fields in the inclusions and matrix are obtained

$$\langle\boldsymbol{\sigma}\rangle_{\mathbf{M}} = -f\boldsymbol{\sigma}^{\infty} \qquad (4.10)$$

$$\langle\boldsymbol{\sigma}\rangle_{\boldsymbol{\Omega}} = (1-f)\boldsymbol{\sigma}^{\infty} \qquad (4.11)$$

If the inclusion theory is combined with the mean field approach, the strain associated to the stress field induced by the interactions between the particles $\boldsymbol{\varepsilon}_{\mathbf{int}} = \mathbf{C}^{-1}\langle\boldsymbol{\sigma}\rangle_{M}$ must be inserted in the equivalency condition (equation4.4). In such conditions, the equivalency condition for Eshelby's equivalent inclusion taking into account the interactions between particles is written as [88]

$$\langle\boldsymbol{\sigma}\rangle_{\boldsymbol{\Omega}} = \mathbf{C}^{*}(\mathbf{S}\boldsymbol{\varepsilon}^{**} - f(\mathbf{S}-\mathbf{I})\boldsymbol{\varepsilon}^{**} - \boldsymbol{\varepsilon}^{*}) = \mathbf{C}(\mathbf{S}\boldsymbol{\varepsilon}^{**} - f(\mathbf{S}-\mathbf{I})\boldsymbol{\varepsilon}^{**} - \boldsymbol{\varepsilon}^{**}) \quad (4.12)$$

from which is derived

$$\boldsymbol{\varepsilon}^{**} = \left\{(1-f)(\mathbf{C}^{*}-\mathbf{C})(\mathbf{S}-\mathbf{I}) + \mathbf{C}^{*}\right\}^{-1}\mathbf{C}^{*}\boldsymbol{\varepsilon}^{*}$$

The above equation is solved to obtain $\boldsymbol{\varepsilon}^{**}$ as a linear function of $\boldsymbol{\varepsilon}^{*}$. The average stress in a particle is then calculated by inserting back $\boldsymbol{\varepsilon}^{**}$ in equation (4.12). In the limit of $f \to 0$, the above equation reduces to the single inclusion problem described in Figure 4.2 and equation (4.5). The elastic energy assigned to a unit volume of particle is

$$W = -\frac{1}{2}\langle\sigma_{ij}\rangle_{\Omega}\varepsilon_{ij}^{*} \qquad (4.13)$$

IV.2 Determination of the stress free lattice parameter mismatch

The lattice parameter a_0^* and a^* of γ and γ' phases respectively have been measured by a diffraction experiment (see Chapter 3). These measured lattice parameters are constrained by the stress field induced by the differences in the unconstrained lattice parameters a_0 and a and by the differences in elastic constants $\mathbf{C}$ and $\mathbf{C}^*$ of pure γ and γ' phases. In order to determine the unconstrained lattice mismatch between γ and γ' phases, an inclusion theory of anisotropic elasticity combined with a mean field approach is used. This lattice mismatch is defined as:

$$\varepsilon_{ij}^T = \frac{a - a_0}{a_0}\delta_{ij} = \varepsilon_0 \delta_{ij} \qquad (4.14)$$

where δ_{ij} is the Kronecker delta.

We consider a single crystal constituted by the γ matrix in which an arrangement of cuboidal γ' particles is embedded, with a volume fraction f. The cuboidal shape of a particle is equivalently approximated as a sphere [89]. The stiffness tensors $\mathbf{C}$ and $\mathbf{C}^*$ of the γ and γ' phases respectively, have the cubic symmetry and are anisotropic ($C_{11} - C_{12} \neq 2C_{44}$). $\mathbf{C}$ is assumed to be that of pure nickel: $C_{11}(=C_{1111}) = 246.4GPa$, $C_{12}(=C_{1122}) = 152.5GPa$, $C_{44}(=C_{2323}) = 122GPa$. $\mathbf{C}^*$ is assumed to be proportional to $\mathbf{C}$ ($\mathbf{C}^* = 1.15\mathbf{C}$) for simplicity. The Eshelby tensor associated to the spherical shape of a particle is noted $\mathbf{S}$ and its values for pure nickel are

$$S_{1111} = 0.445\,,\ S_{1122} = 0.091\,,\ S_{1212} = 0.347. \qquad (4.15)$$

These are obtained by numerical integration [86]. The other non-zero components of the tensor are obtained by suitable permutation. Similar to the isotropic case, the tensors with an odd number of the same index vanish.

In this case, the actual eigenstrain given to each particle is

$$\boldsymbol{\varepsilon}^* = \boldsymbol{\varepsilon}^{\mathbf{T}} \qquad (4.16)$$

The equivalent eigenstrain $\boldsymbol{\varepsilon}^{**}$ that takes into account the inhomogeneity effect ($C^* \neq C$) is obtained using (4.12). As $\boldsymbol{\varepsilon}^{**}$ is isotropic, we can write $\varepsilon_{ij}^{**} = \varepsilon^{**}\delta_{ij}$

The total strain in a particle can then be expressed as

$$\langle \boldsymbol{\gamma} \rangle_p = \mathbf{S}\boldsymbol{\varepsilon}^{**} - f(\mathbf{S}-\mathbf{I})\boldsymbol{\varepsilon}^{**} \qquad (4.17)$$

The first term corresponds to the total strain of a single particle and the second is the mean field from other particles. This deformation tensor is also isotropic. We can write

$$\langle \gamma_{ij} \rangle_p = \gamma_p \delta_{ij}$$

$$\text{where } \gamma_p = S_{11ii}\varepsilon^{**} - f(S_{11ii}-1)\varepsilon^{**} = (S_{11}+2S_{12})(1-f)\varepsilon^{**} + f\varepsilon^{**} \qquad (4.18)$$

The total strain in matrix corresponds to the mean field resulting from the interactions between the particles. We can therefore write

$$\langle \boldsymbol{\gamma} \rangle_M = -f(\mathbf{S}-\mathbf{I})\boldsymbol{\varepsilon}^{**} \quad (4.19)$$

Similar to the case of the particles, we can write

$$\langle \gamma_{ij} \rangle_M = \gamma_M \delta_{ij}$$

$$\text{where } \gamma_M = -f(S_{11ii}-1)\varepsilon^{**} = f(1-S_{11}-2S_{12})\varepsilon^{**} \quad (4.20)$$

From equations (4.18) and (4.20), we can calculate the constrained lattice parameters to be

$$\text{In the } \gamma\text{' precipitates } a^* = (1+\gamma_p)a_0 \qquad (4.21)$$

$$\text{In the } \gamma \text{ matrix } a_0^* = (1+\gamma_M)a_0 \qquad (4.22)$$

Now we consider the ratio $X^* = a^*/a_0^*$ that was determined by diffraction to be $X = 0.99855$. We can write it under the following form

$$X^* = \frac{a^*}{a_0}\left(\frac{a_0^*}{a_0}\right)^{-1} \qquad (4.23)$$

By inserting (4.21) and (4.22) in equation (4.23), we get the following equation

$$\varepsilon^{**} = \frac{1 - X^*}{fX^*(1 - S_{11} - 2S_{12}) - (1 - f)(S_{11} + 2S_{12}) - f} \qquad (4.24)$$

The natural lattice misfit can then be determined using (4.24) and the following equation is derived from (4.12)

$$\boldsymbol{\varepsilon}^T = (\mathbf{C}^*)^{-1}\left\{(\mathbf{C}^* - \mathbf{C})\left[\mathbf{S} - f(\mathbf{S} - \mathbf{I})\right] + \mathbf{C}\right\}\boldsymbol{\varepsilon}^{**} \quad (4.25)$$

The stress free lattice parameter mismatch was found to be equal to $\varepsilon_0 = -0.23\%$ in the MC-NG superalloy using (4.25). This value is far from that determined in Chapter 3 ($\varepsilon_0 = -0.06\%$). However, the numerical values used for the matrix elastic constants are those of pure nickel, and the precipitate phase was assumed to be 15% harder than the matrix, what is far below the reality.

IV.3 Elasticity analysis of the strain induced rafting phenomenon

Several theories have been proposed to explain rafting or a shape change of the γ' particles occurring under an external applied stress, [90-92]. However, the rafting of γ' particles can also occur under no external stress, if an alloy is prestrained and subsequently annealed [7, 8]. This means that rafting is primarily caused by the residual stress brought about by matrix plastic deformation, which should have a similar effect to that induced by the early stages of creep. The residual stress and its associated elastic energy can relax during further annealing at high temperature by a change in the morphology of the γ' particles. The following analysis proposes that this relaxation of the residual stress is the origin of rafting. Several authors have already noticed a role of plastic strain in rafting [7, 8, 67, 72]. In the following, the rafting phenomenon is discussed from this point of view, using the inclusion theory of anisotropic elasticity.

IV.3.1 Main hypotheses

We consider a single crystal having γ' particles with a volume fraction f, surrounded by the γ matrix. The stress free precipitation misfit strain between γ and γ' phases was determined above and is given by (4.14). Next, we consider the role of plastic deformation in the matrix. We suppose that the matrix is uniaxially deformed plastically by ε_P along the elongation axis [001], as the γ' phase is harder than the γ matrix. This deformation is supposed to be uniform, homogeneous and symmetric: i.e. the lateral directions undergo the plastic strain of $-\varepsilon_P/2$. A tensile deformation results in a positive ε_p, whereas ε_p is negative in the case of a compression deformation. We can then define a plastic deformation induced misfit strain given to the γ' particles as

$$\boldsymbol{\varepsilon}^{\mathbf{P}} = \begin{pmatrix} \varepsilon_P/2 & 0 & 0 \\ 0 & \varepsilon_P/2 & 0 \\ 0 & 0 & -\varepsilon_P \end{pmatrix}. \quad (4.26)$$

The total misfit strain (eigenstrain) $\boldsymbol{\varepsilon}^*$ is then given by

$$\boldsymbol{\varepsilon}^* = \boldsymbol{\varepsilon}^{\mathbf{T}} + \boldsymbol{\varepsilon}^{\mathbf{P}}. \quad (4.27)$$

The γ' particles are cuboidal before the morphology change (rafting) and are approximated as spheres [89]. As shown later, the disk shape of the particles is good enough to see the tendency of the shape change. Thus, the Eshelby tensors ***S*** for spheres and disks normal to [001] and normal to [100] or [010] are used in the main analysis. By symmetry, the cases of disk shaped particles normal to [100] and [010] are equivalent. For disks with the flat surface normal to [001], these are

$$S_{1111} = 1,\ S_{3311} = S_{3322} = C_{12}/C_{11},\ \ S_{3131} = S_{3232} = 0.5, \text{ others } S_{ijkl} = 0. \quad (4.28)$$

The Eshelby tensors for disks normal to [100] and [010] are obtained by proper permutations. The equivalent eigenstrain for inhomogeneous inclusions is calculated using (4.12) and then inserted back to evaluate the average stress inside a particle. The elastic energy W is then calculated, essentially using (4.13). In this way, we can

directly compare the elastic energy evolution with matrix plastic strain for different shapes of particles.

IV.3.2 Results

In Fig. 4.3, W is plotted against matrix plastic strain when the precipitation misfit is $\varepsilon_0 = -0.2\%$ and $f = 0.7$. When the plastic strain is positive (tensile case), the disk shaped particles normal to [001] show the lowest elastic energy. The difference in the elastic energy between the considered morphologies becomes larger as the plastic strain increases. This means that a tensile plastic strain tends to induce rafting. When the plastic strain is negative, the disks normal to [100] or [010] have the lowest energy. These results are in agreement with experimental observations made after tensile or compressive prestrain [7, 93]. Figure 4.3 is limited to small plastic strains. When ε_P becomes less than approximately -1.2%, the spherical shape has the smallest elastic energy.

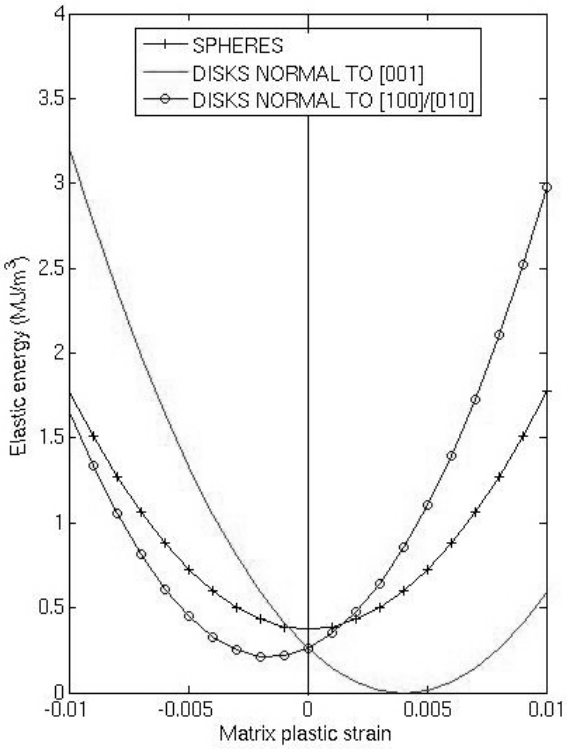

Figure 4.3: Elastic energy per unit volume of a particle as a function of matrix plastic strain.

A single inclusion problem is even sufficient to see the effect of particle shape, as long as a qualitative discussion is conducted. This point is shown in Figure 4.4, which represents the single inclusion solution. This is to be compared with Figure 4.3. The difference lies only in the fact that the case of $f = 0.7$ (Fig.4.3) has a lower energy approximately by the factor of 4 as a result of the interaction between the particles. This difference becomes an important factor, when the role of an interfacial energy is quantitatively examined, or when internal stresses are evaluated.

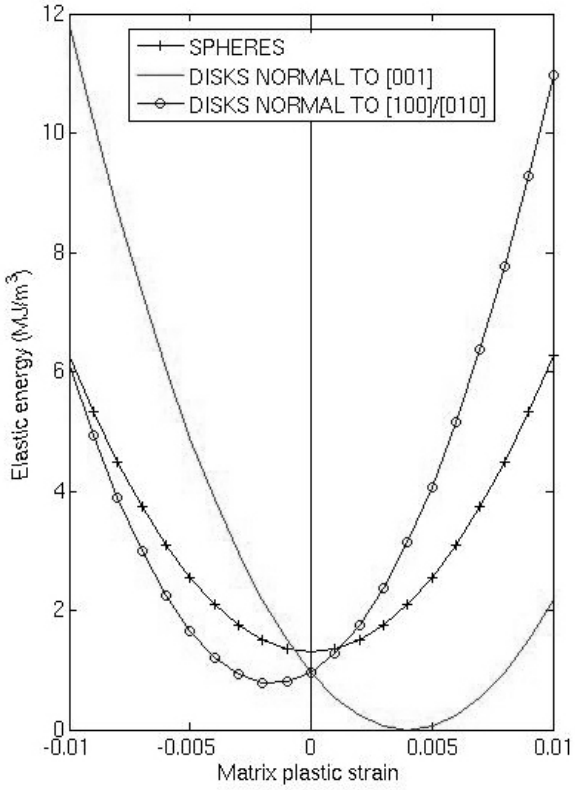

Figure 4.4: Energy assigned to a unit volume of a particle as a function of matrix plastic strain when the interactions between particles is ignored

Since the precipitation misfit strain and the plastic strain contribute separately but linearly to stress, the elastic energy change with plastic strain in the case of positive precipitation strain should be of mirror symmetry with respect to the case of negative precipitation strain. This point is in fact confirmed in Fig. 4.5. Thus, we can see that the disk shaped particle normal to [001] is energetically favoured in the case of compressive plastic strain, while the disks normal to [100] or [010] are favoured for tensile plastic strain, when the precipitation misfit strain is positive. Similar to Figure

4.3, when ε_P is larger than approximately 1.2%, the spherical particle has the smallest elastic energy.

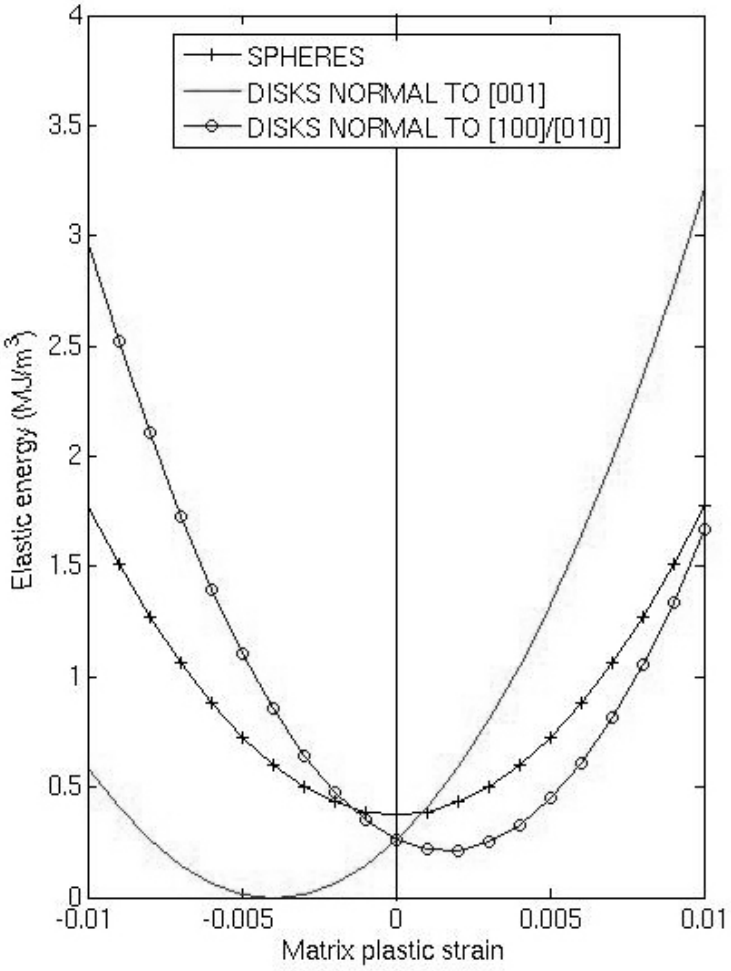

Figure 4.5: Elastic energy per unit volume of a particle as a function of matrix plastic strain. Sphere and disks normal and parallel to [001] are investigated. The precipitation misfit strain is $\varepsilon_0 = 0.2\%$ and the volume fractions of the particles is $f = 0.7$.

We have also examined the elastic energy associated with a needle shaped particle, using the method developed by Mura [86]. A formulation for the Eshelby tensor can be obtained analytically. This is shown in Appendix B. It has been found that such a particle does not reduce the energy as much as a disk, as shown in Figure 4.6.

In order to discuss the change of the particle shape occurring under diffusion processes, we have also examined ellipsoidal inclusions, described by

$$\frac{x_1^2 + x_2^2}{a^2} + \frac{x_3^2}{c^2} \le 1, \qquad (4.29)$$

where x_1, x_2, x_3-axes are parallel to [100], [010] and [001] respectively. The Eshelby tensor was calculated numerically using the method given in Mura's book section 17 [86]. The aspect ratio $r = c/a$ was varied to simulate the shape change of the inclusion. The extreme cases of very small or large *r* are confirmed to coincide with the cases of a flat inclusion normal to [001] (disk) and a needle particle, respectively.

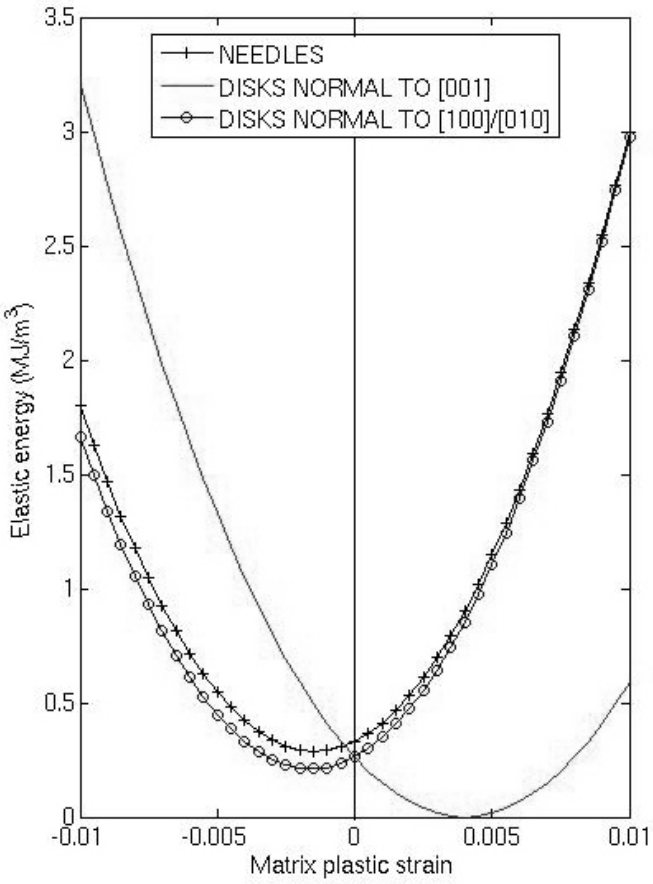

Figure 4.6: Elastic energy per unit volume of a particle as a function of matrix plastic strain.

Figures 4.7 and 4.8 show the elastic energy plotted against the spheroid aspect ratio when the magnitude of plastic strain is $\pm 0.5\%$, and the precipitation misfit strain is $\pm 0.2\%$ respectively. As the aspect ratio changes to either very large or very small, corresponding to needles or disks normal to [001] respectively, the elastic energy

decreases for compressive or tensile matrix plastic strain, depending on the sign of the misfit strain. If the misfit strain is negative, as shown in Figure 4.7, small aspect ratios lead to lower energy in tension. Conversely, if the misfit strain is positive, small aspect ratios lead to lower energy in compression, as shown in Figure 4.8. In this way, the effect of the precipitation misfit strain on the shape of the particle after plastic strain is introduced is clearly visible. If the energy of the γ/γ' interface is known, this figure can be used to determine the realistic shape of the γ' particles. The elastic energy continuously decreases as the shape becomes either extremely flat or long. This shape change induces an increase in the interfacial energy. The total energy thus becomes minimum when a γ' particle adopts a certain value of the aspect ratio, the value depending on the particle size.

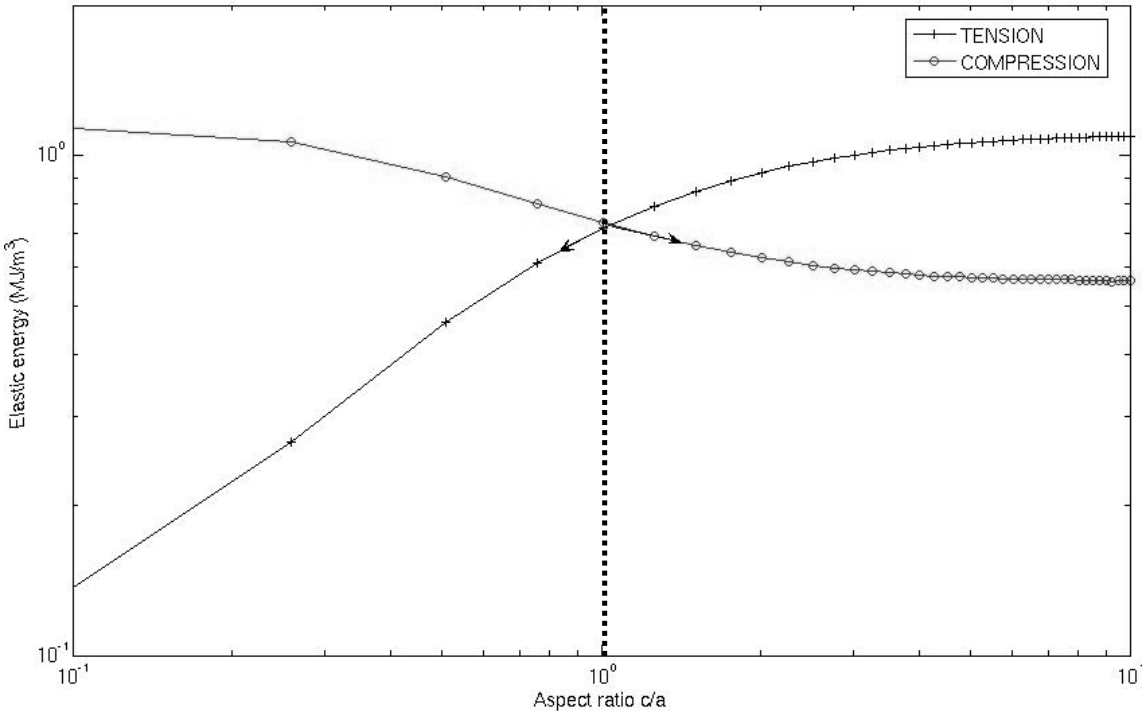

Figure 4.7: Total elastic energy per unit volume of particle as a function of the spheroid aspect ratio. The matrix plastic strain is $\varepsilon_p = \pm 0.5\%$ and the precipitation misfit strain is $\varepsilon_0 = -0.2\%$

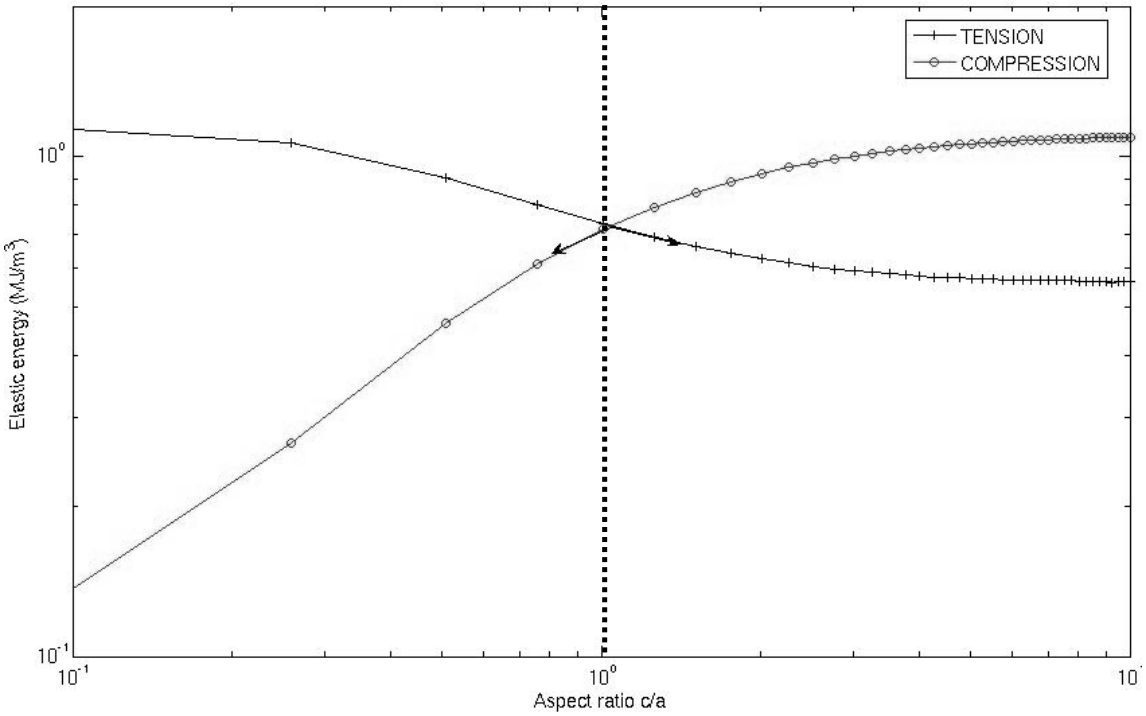

Figure 4.8: Total elastic energy per unit volume of particle as a function of the spheroid aspect ratio. The matrix plastic strain is $\varepsilon_p = \pm 0.5\%$ and the precipitation misfit strain is $\varepsilon_0 = 0.2\%$.

In the above calculations, we have rather limited the magnitude of the plastic strain. This is because plastic deformation in the γ' particles by shearing starts when the macroscopic creep strain is usually a few percent. Beyond this critical creep strain, the discussion in the context of the present study becomes impractical. Also, when the magnitude of precipitation strain is large, we will see the effect of plastic strain on the shape of the γ' particles only when the magnitude of plastic strain becomes as large as or larger than that of the precipitation strain. This case is omitted for the same reason as given above.

Moreover, the role of precipitation misfit strain in the rafting phenomenon was also examined. When precipitation misfit strain is zero, *i.e.* γ and γ' phases have the same lattice parameter when considered separately, the spherical particle shape shows the lowest elastic energy, whatever the amount of plastic strain introduced in the matrix. This point is shown in Figure 4.9. In other words, in the absence of precipitation misfit

strain, the γ' particles keep their initial shape during the high temperature annealing, even if the γ matrix was previously deformed. This means that precipitation misfit strain is required to induce the rafting phenomenon.

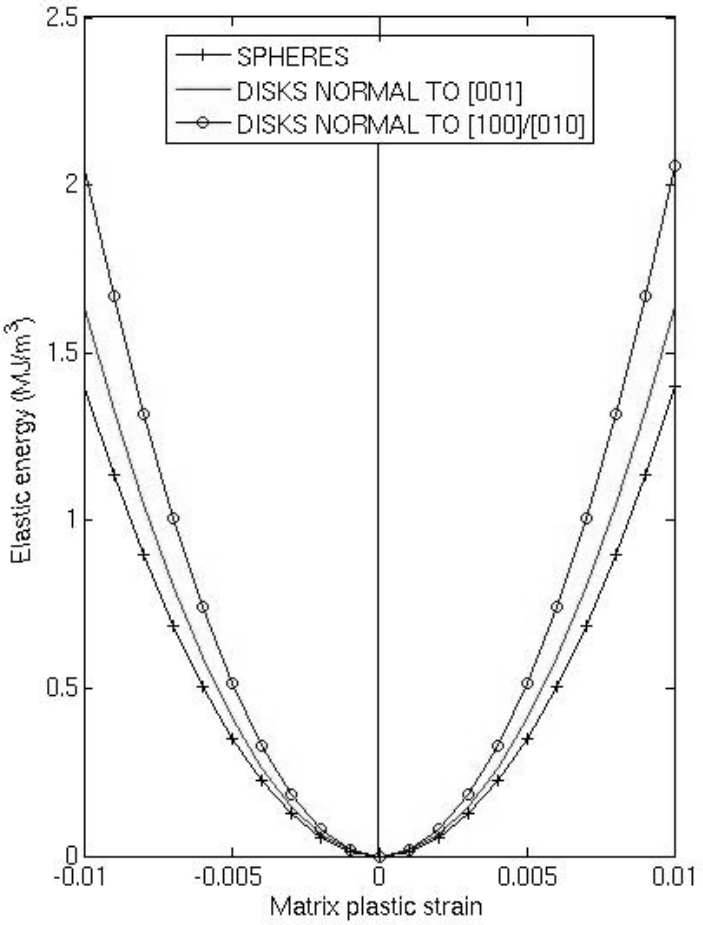

Figure 4.9: Elastic energy assigned to a unit volume of particle as a function of matrix plastic strain when precipitation misfit strain is zero

IV.4 Lattice parameter evolution during strain induced rafting

Using the same method, the lattice parameter evolution of γ and γ' phases during strain induced rafting is evaluated in order to determine the evolution of the lattice parameter mismatch between γ and γ' phases This prediction is then compared with experimental data. In practice, this is done as follows. The γ' particles are given the eigenstrain defined in (4.27) where the precipitation misfit strain is that determined in section IV.2. The particles have an ellipsoidal shape described by equation (4.29). In

these calculations, the plastic deformation corresponds to the tensile case and the matrix plastic strain is $\varepsilon_P = 0.6\%$. In such conditions (negative precipitation misfit strain and positive matrix plastic strain), the rafting phenomenon corresponds to a decrease in the aspect ratio r of the particles (formation of discs perpendicular to the elongation axis ($r < 1$) from spherical particles ($r = 1$)). The total deformation in a particle and in the matrix are given by equations (4.17) and (4.19) respectively, where ε^{**} is the equivalent eigenstrain determined using (4.12) for an inhomogeneous inclusion of eigenstrain ε^{*}. Since the plastic strain is introduced, the lattice parameters of the embedded γ' particles and matrix have a tetragonal symmetry. For example, the γ' particles have $a^* = b^* \neq c^*$. These are given by

$$a^* = b^* = (1 + \langle \gamma_{11} \rangle_p) a_0 = (1 + S_{ii11}\varepsilon_{11}^{**} - f(S_{ii11} - 1)\varepsilon_{11}^{**}) a_0 \quad (4.30)$$

$$c^* = (1 + \langle \gamma_{33} \rangle_p) a_0 = (1 + S_{ii33}\varepsilon_{33}^{**} - f(S_{ii33} - 1)\varepsilon_{33}^{**}) a_0 \quad (4.31)$$

Equivalently, we get for the matrix

$$a_0^* = b_0^* = (1 + \langle \gamma_{11} \rangle_M) a_0 = (1 - f(S_{ii11} - 1)\varepsilon_{11}^{**}) a_0 \quad (4.32)$$

$$c_0^* = (1 + \langle \gamma_{33} \rangle_M) a_0 = (1 - f(S_{ii33} - 1)\varepsilon_{33}^{**}) a_0 \quad (4.33)$$

We can then calculate the lattice parameter changes associated to a decrease in aspect ratio. Figure 4.10 shows the evolution of the lattice parameter perpendicular to the tensile axis [001]. A decrease of the γ lattice parameter a_0^* is observed, while the γ' phase shows an increase in lattice parameter. The tendencies deduced from these results are in agreement with the experimental results shown in Figure 3.28 to 3.30 in the case of the 200 reflection. Equivalently, the evolution of the lattice parameters parallel to the tensile axis c^* and c_0^* of γ' and γ phases respectively show the same trends as the experimental results in the case of the 002 reflection (parallel to the elongation axis), as shown in Figure 4.11. In such calculations, the kinetic aspects of dislocation motion in the material are ignored. This approach is valid as long as qualitative discussion is conducted.

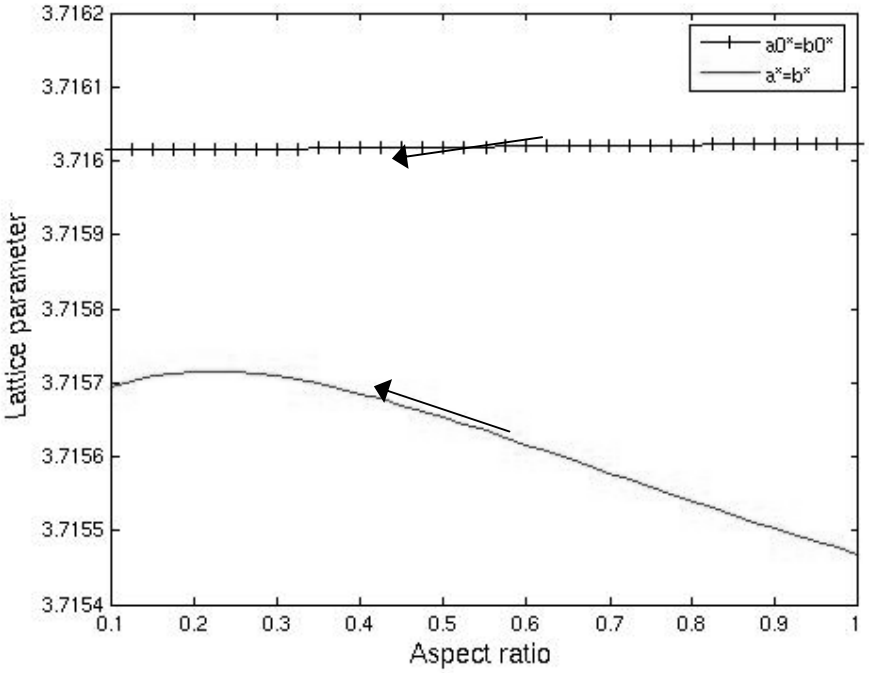

Figure 4.10: Lattice parameter evolution in γ and γ' phases perpendicularly to the elongation axis [001]. $a_0 = 3.715\,\text{Å}^0$

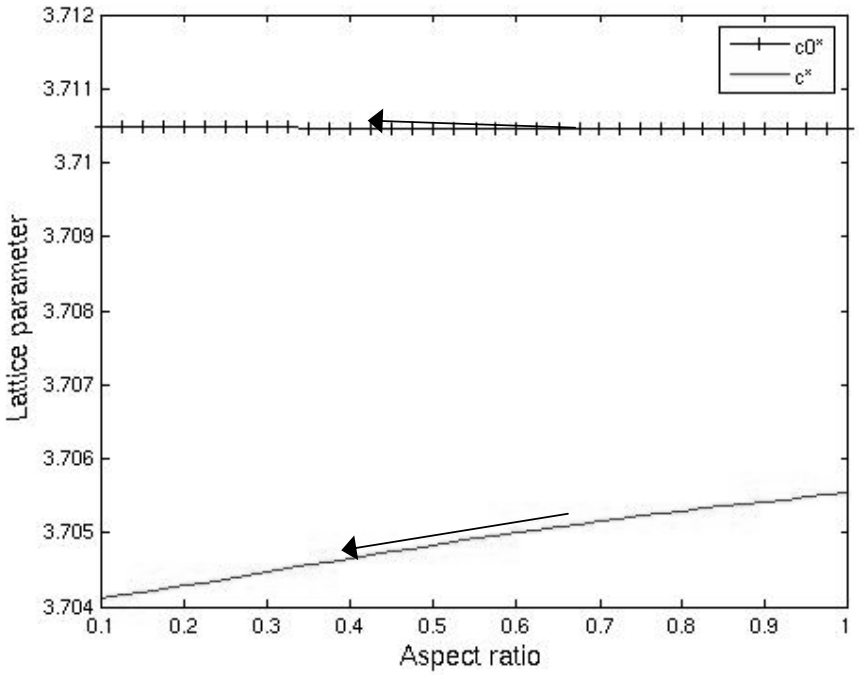

Figure 4.11: Lattice parameter evolution in γ and γ' phases parallel to the elongation axis [001]. $a_0 = 3.715\,\text{Å}^0$

Moreover, the lattice mismatch parallel and perpendicular to the tensile axis can be evaluated for a given particle aspect ratio using

$$\delta_{//} = \frac{c^* - c_0^*}{c_0^*}, \delta_{\perp} = \frac{a^* - a_0^*}{a_0^*} \qquad (4.34)$$

The tendencies for the lattice parameter mismatch evolution are shown in Figure 4.12. They are consistent with the experimental results described in Chapter 3. As pointed out previously, the model presented above is valid as long as qualitative aspects are considered. In these calculations, plastic deformation is assumed to be uniform in the matrix. In reality, the presence of a stress field induced by a negative lattice parameter mismatch induces a preferred development of the plastic flow in the horizontal matrix channels when a tensile stress is applied. The dislocation density is therefore larger in horizontal matrix channels than in the vertical ones.

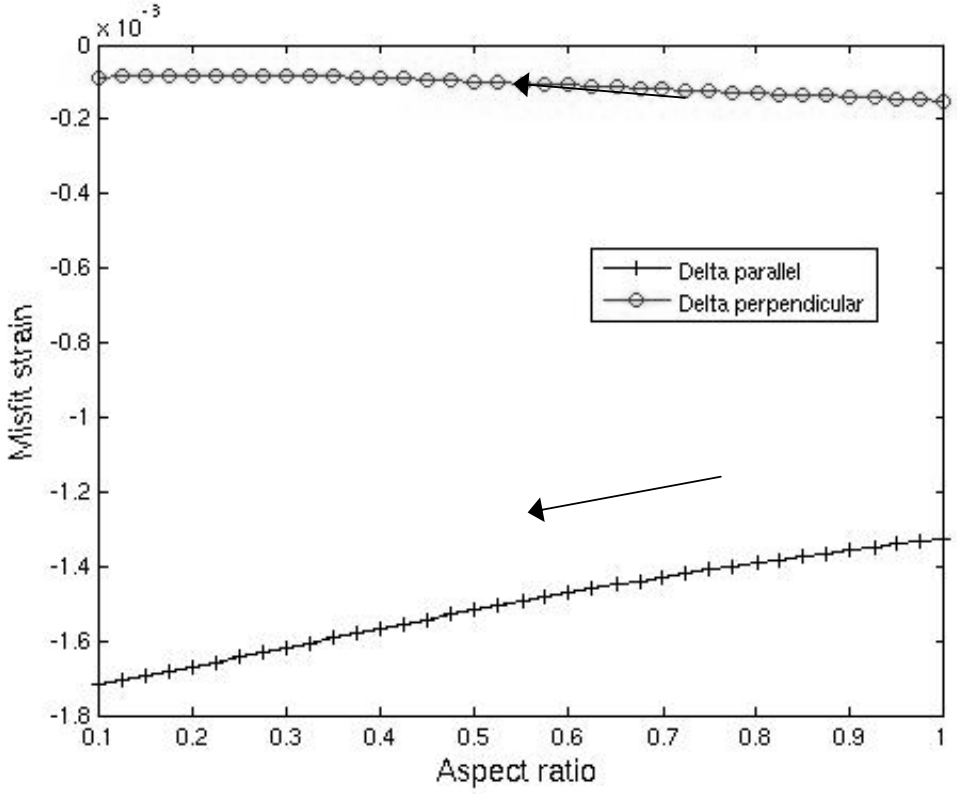

Figure 4.12: Evolution of the lattice mismatch parallel and perpendicular to the tensile axis during strain induced rafting

IV.5 Discussion of the deformation mode

In the elasticity analysis of the rafting phenomenon developed in section IV.3, a uniform plastic strain confined in the γ matrix was assumed. However, it was pointed out in section I.2.5 that the presence of a coherency stress field induced by a negative precipitation misfit strain tends to promote dislocation glide in horizontal matrix channels with respect to the tensile axis. The glide of dislocations is enhanced in the vertical matrix channels when the plastic deformation results from a compressive load. Horizontal channels, hereafter called P_3 , are the matrix subdomains normal to [001] and vertical channels P_1 and P_2 those normal to [100] and [010] respectively, when the largest component of plastic strain is along [001]. They are shown in Figure 4.13.

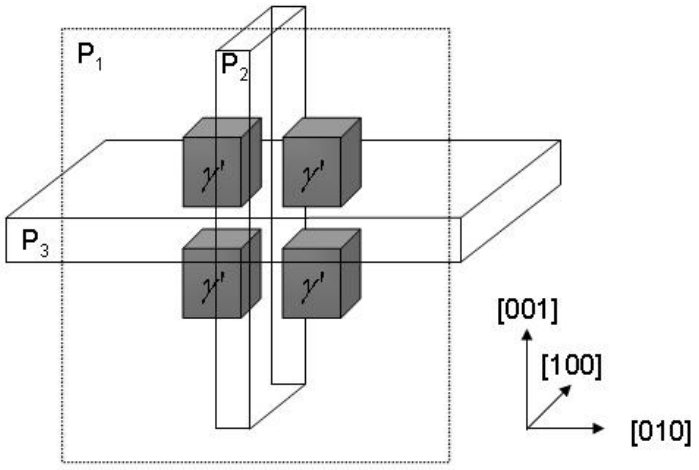

Figure 4.13: Definition of the matrix channels used in this investigation

In this section we will discuss the validity of the hypothesis of uniform deformation that was assumed in section IV.3. Only the case of a cuboidal particle shape is considered. In order to conduct the analysis in a perspective way, we approximate the γ' phase and the γ matrix to have the same elastic constants. The analysis described in section IV.3 has shown that this assumption gives nearly the same results as that of an elastically harder γ' phase and predicts rafting in a

successful manner. For clarity, the case of homogeneous inclusions is shown in Figure 4.14. The calculations developed below show that the hypothesis of uniform matrix deformation is valid for all practical purposes.

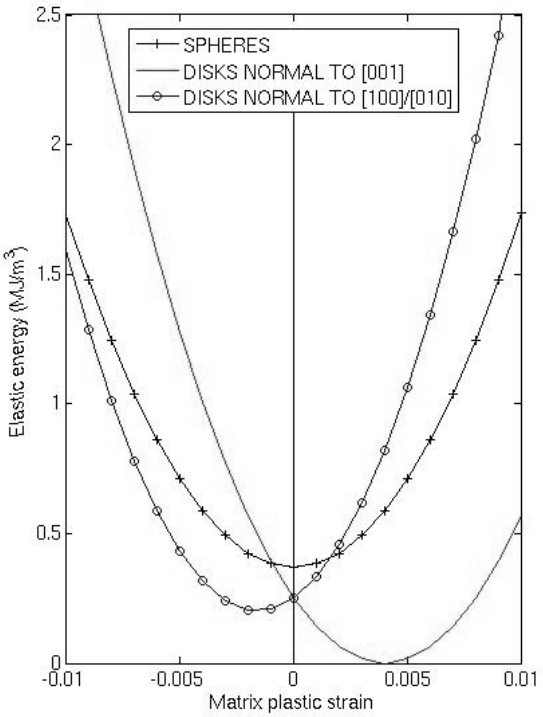

Figure 4.14: Elastic energy per unit volume of particle as a function of matrix plastic strain. The inhomogeneity effect was ignored. The precipitation misfit strain was $\varepsilon_0 = -0.2\%$ and the volume fraction of the particles is $f = 0.7$

Similar to the previous analysis, the precipitation misfit strain (eigenstrain) has the form of

$$\varepsilon_{ij}^{T} = \varepsilon_0 \delta_{ij} \qquad (4.14)$$

In the frame of anisotropic ellipsoidal inclusion theory, and approximating the cuboidal particle shape with a spherical shape, the stress inside a single particle is evaluated using (4.2) and is expressed as

$$\sigma_{ij}^{I} = (C_{11} + 2C_{12})(S_{1111} + 2S_{1122} - 1)\varepsilon_0 \delta_{ij} \qquad (4.35)$$

where $\mathbf{C}$ and $\mathbf{S}$ are the elastic stiffness and the Eshelby tensor of a spherical particle respectively. The numerical values of the components of these two tensors are given in section IV.2. When there are many similar shaped particles V having the

same eigenstrain $\boldsymbol{\varepsilon}^{\mathbf{T}}$ with a volume fraction f, the average stress inside the particles is calculated using the mean field method [87] to be

$$\left\langle \sigma_{ij} \right\rangle_V = (1-f)\sigma_{ij}^I \qquad (4.36)$$

And in the matrix M

$$\left\langle \sigma_{ij} \right\rangle_M = -f\sigma_{ij}^I \qquad (4.37)$$

Using equation (4.5), the elastic energy caused by the above particles is calculated as

$$E_0 = \frac{3}{2} f(1-f)(C_{11}+2C_{12})(1-S_{1111}-2S_{1122})\varepsilon_0^2 \qquad (4.38)$$

Next we consider three different deformation modes: uniform deformation, horizontal channels deformation and vertical channels deformation. The elastic energy E_P associated to the introduction of plastic strain into matrix subdomains is evaluated for each case. The interaction energy E_I, associated to the interaction between the plastic strain and the precipitation misfit strain, must be taken into account. In a body D containing precipitation misfit strain (case 1) and plastic strain (case 2), it is expressed as

$$E_I = -\int_D \sigma_{ij}(1)\varepsilon_{ij}^*(2)dV \qquad (4.39)$$

Here, $\sigma_{ij}(1)$ is the stress in case 1 (precipitation misfit strain) given by equation (5.2) and $\varepsilon_{ij}(2)$ is the eigenstrain in case 2 (plastic strain). The role of cases 1 and 2 can be interchanged. The introduction of plastic strain into the material leads to an elastic energy increase, which corresponds to sum of the elastic energy E_P, induced by the plastic strain itself, and the elastic energy E_I due to interaction between plastic strain and precipitation misfit strain. In the following, the terms E_P and E_I are evaluated for different deformation modes. The deformation mode leading to the lowest elastic energy increase $\Delta E = E_P + E_I$ is the energetically favourable deformation mode.

IV.5.1 Role of a uniform plastic deformation in the matrix

The plastic deformation is assumed to be induced by uniaxial loading along [001] and to be uniform. It is written under the form of (4.26). Similar to what was done in section IV.3, the stress caused by this plastic strain is calculated by giving the negative eigenstrain of ε_{ij}^{P} to the particles. In these conditions, the average stress inside the particles is calculated to be

$$\left\langle \sigma_{11}(uniform) \right\rangle_V = \left\langle \sigma_{22}(uniform) \right\rangle_V = (1-f)(C_{11}-C_{12})(S_{1111}-S_{1122}-1)\varepsilon_p/2 \qquad (4.40)$$

$$\left\langle \sigma_{33}(uniform) \right\rangle_V = -(1-f)(C_{11}-C_{12})(S_{1111}-S_{1122}-1)\varepsilon_p$$

The self elastic energy is then calculated as

$$E_P(uniform) = \frac{3}{4} f(1-f)(C_{11}-C_{12})(1+S_{1122}-S_{1111})\varepsilon_p^2 \qquad (4.41)$$

In this particular case, since $\left\langle \sigma_{ii}(uniform) \right\rangle_V = 0$, there is no interaction between the stress due to plastic strain and precipitation misfit. The interaction energy is therefore zero. The elastic energy increase associated to uniform plastic strain is therefore calculated to be

$$\Delta E(uniform) = E_P(uniform) \qquad (4.42)$$

IV.5.2 Role of plastic deformation in the γ horizontal channels

In certain conditions of plastic strain and precipitation misfit (see section I.2.5), plastic deformation may be confined in the horizontal channels of the γ matrix. These channels, called P_3 and having a volume fraction $F_3 = 1 - f^{1/3}$, are approximated as flat inclusions normal to the elongation axis having the eigenstrain given by (4.26). Using (4.2) and the expression of the Eshelby tensor of a disk, the stress in a single horizontal channel is

$$\sigma_{11}^{I}(P_3)=\sigma_{22}^{I}(P_3)=-\frac{(C_{11}+2C_{12})(C_{11}-C_{12})}{2C_{11}}\varepsilon_p,\sigma_{33}^{I}(P_3)=0 \qquad (4.43)$$

Using the mean field method [87], the average stresses inside the plastic horizontal channels is calculated to be

$$\begin{aligned}&\left\langle\sigma_{11}(horizontal)\right\rangle_{P_3}=\left\langle\sigma_{22}(horizontal)\right\rangle_{P_3}=-(1-F_3)\frac{(C_{11}+2C_{12})(C_{11}-C_{12})}{2C_{11}}\varepsilon_p,\\&\left\langle\sigma_{33}(horizontal)\right\rangle_{P_3}=0\end{aligned} \qquad (4.44)$$

And outside the plastic horizontal channels,

$$\begin{aligned}&\left\langle\sigma_{11}(horizontal)\right\rangle_{M}=\left\langle\sigma_{22}(horizontal)\right\rangle_{M}=F_3\frac{(C_{11}+2C_{12})(C_{11}-C_{12})}{2C_{11}}\varepsilon_p,\\&\left\langle\sigma_{33}(horizontal)\right\rangle_{M}=0\end{aligned} \qquad (4.45)$$

Using the above result, the elastic energy increase associated to horizontal γ channels plastic deformation is given by the sum of

$$E_P(horizontal)=\frac{1-F_3}{F_3}\frac{(C_{11}+2C_{12})(C_{11}-C_{12})}{4C_{11}}\overline{\varepsilon_p}^{2} \qquad (4.46)$$

$$E_I(horizontal)=f\frac{(C_{11}+2C_{12})(C_{11}-C_{12})}{C_{11}}\overline{\varepsilon_p}\varepsilon_0 \qquad (4.47)$$

$\overline{\varepsilon_P}$ is the macroscopic plastic strain and is evaluated as

$$\overline{\varepsilon_P}=F_3\varepsilon_P \qquad (4.48)$$

When the magnitude of the plastic strain is small, the interaction energy in (4.47) is dominant over the elastic energy produced by the plastic strain itself in (4.46). This means that the plastic deformation in the horizontal channels must be examined in the beginning of the deformation. A negative interaction energy, leading

to a lower elastic energy increase ΔE, is obtained when the following condition is satisfied

$$\overline{\varepsilon_P}\varepsilon_0 < 0 \qquad (4.49)$$

This condition is consistent with the enhanced glide of dislocations in horizontal matrix channels when precipitation misfit strain is negative and when plastic strain results from a tensile load (see section I.2.5). Therefore, the role of plastic deformation in horizontal matrix channels is not considered when the condition given by (4.49) is not satisfied. In such conditions, the interaction elastic energy becomes positive. On the other hand, when the magnitude of plastic strain is large, the assumption of uniform deformation can be justified, as shown later.

IV.5.3 Role of plastic deformation in vertical matrix channels

In the case of vertical matrix channels, two types of channels must be distinguished. The P_1 channels are those normal to (100) and P_2 those normal to (010), as shown in Figure 4.13. Their respective volume fraction is equal to F_3. From symmetry consideration and volume constancy; we can assume the plastic strain to be

$$\varepsilon_{11}^P(1) = -(\frac{1}{2} - \alpha)\varepsilon_P, \varepsilon_{22}^P(1) = -(\frac{1}{2} + \alpha)\varepsilon_P, \varepsilon_{33}^P(1) = \varepsilon_P \text{ in } P_1 \text{ channels} \qquad (4.50)$$

$$\varepsilon_{11}^P(2) = -(\frac{1}{2} + \alpha)\varepsilon_P, \varepsilon_{22}^P(2) = -(\frac{1}{2} - \alpha)\varepsilon_P, \varepsilon_{33}^P(2) = \varepsilon_P \text{ in } P_2 \text{ channels} \qquad (4.51)$$

The parameter α, describes the repartition of plastic deformation along the lateral directions. If $\alpha = -1/2$, the whole plastic deformation is transferred along the direction labelled by the index 1, *i.e.* [100] in our case. Similarly, if $\alpha = 1/2$, the whole plastic deformation is transferred along the direction labelled by the index 2 ([010]). It depends on ε_P and must obey the condition

$$-\frac{1}{2} \le \alpha \le \frac{1}{2} \qquad (4.52)$$

When plastic deformation occurs only in the P_1 channels, the resulting stress inside the channel $\sigma_{ij}^{I}(1)$ is calculated using the same method employed above (see previous section). In such conditions, this stress is given by

$$\begin{aligned} &\sigma_{11}^{I}(1) = 0, \sigma_{22}^{I}(1) = \frac{C_{11} - C_{12}}{C_{11}} \left\{ (C_{11} + C_{12})(\frac{1}{2} + \alpha) - C_{12} \right\} \varepsilon_P \\ &\sigma_{33}^{I}(1) = -\frac{C_{11} - C_{12}}{C_{11}} \left\{ -C_{12}(\frac{1}{2} + \alpha) - (C_{11} + C_{12}) \right\} \varepsilon_P \end{aligned} \qquad (4.53)$$

The stresses in a single P_2 channel, $\sigma_{ij}^{I}(2)$ are similarly written. From the expressions of the above stress fields, and using the mean field method [87], the elastic energies due solely to plastic deformation (E_P) and due to the interaction between plastic strain and precipitation misfit (E_I), are calculated using (4.5) and (4.39). They are respectively expressed as

$$\begin{aligned} E_P(vertical) = &\frac{C_{11} - C_{12}}{C_{11}} \frac{\overline{\varepsilon_P}^2}{4F_3} [(C_{11} + C_{12})(\frac{1}{2} + \alpha)^2 - 2C_{12}(\frac{1}{2} + \alpha) \\ &+ (C_{11} + C_{12}) - F_3 \left\{ (C_{11} - C_{12})(\frac{1}{2} + \alpha) + 2C_{11} + C_{12} \right\} \end{aligned} \qquad (4.54)$$

$$E_I(vertical) = f \frac{(C_{11} + 2C_{12})(C_{11} - C_{12})}{C_{11}} (\alpha - \frac{1}{2}) \overline{\varepsilon_P} \varepsilon_0 \qquad (4.55)$$

Since the condition (4.52) is imposed, the interaction energy given by the above equation becomes negative when the following condition is satisfied

$$\overline{\varepsilon_P} \varepsilon_0 \ge 0 \qquad (4.56)$$

Plastic deformation in vertical matrix channels is therefore examined in the above range. This is due to the effect of internal stress caused by precipitation misfit

strain, as pointed out in section I.2.5. In order to determine the α parameter as a function of plastic strain, the elastic energy increase $\Delta E = E_P + E_I$ due to the introduction of plastic strain, must be minimized with respect to α. The calculation of the root of $\frac{\partial \Delta E}{\partial \alpha}$ gives the following expression

$$\frac{1}{2} + \alpha = \frac{1}{2(C_{11} + C_{12})} \left\{ 2C_{12} + F_3(C_{11} - C_{12}) - 4fF_3(C_{11} + 2C_{12}) \frac{\varepsilon_0}{\overline{\varepsilon_P}} \right\} \quad (4.57)$$

The condition (4.52) is satisfied when

$$\frac{\overline{\varepsilon_P}}{\varepsilon_0} > l_1$$
$$l_1 = 4fF_3 \frac{C_{11} + 2C_{12}}{2C_{12} + F_3(C_{11} - C_{12})} \quad (4.58)$$

However, when $\overline{\varepsilon_P} / \varepsilon_0$ is less than l_1, the α value given by (4.58) does not satisfy the condition given by (4.52). Thus, when $0 \le \overline{\varepsilon_P} / \varepsilon_0 \le l_1$ it is natural to adopt

$$\frac{1}{2} + \alpha = 0 \quad (4.59)$$

For clarity, the dependence of α on $\overline{\varepsilon_P} / \varepsilon_0$ is shown in Figure 4.15.

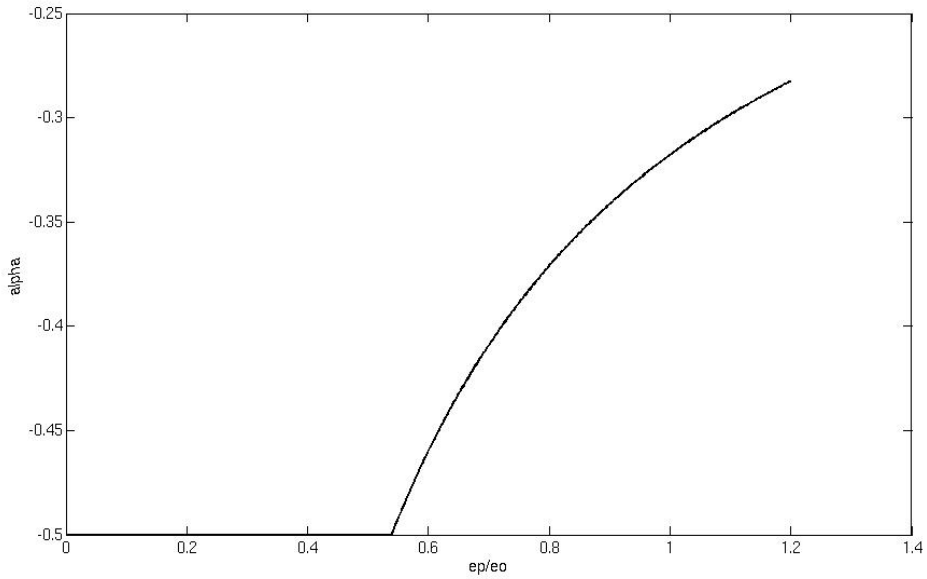

Figure 4.15: Dependence of α on $\overline{\varepsilon_P} / \varepsilon_0$

IV.5.4 Deformation mode

The comparison between the three deformation modes examined is shown in Figure 4.16. The precipitation misfit strain is negative and equal to $\varepsilon_0 = -0.2\%$. In the range of (4.49), *i.e.* for a tensile deformation, uniform and horizontal matrix channels deformation modes have been considered. The vertical channel deformation mode has not been considered, as it leads to a largest elastic energy increase in this range.

Similarly, in the range of (4.56), *i.e.* for a compressive deformation, the interaction energy between the plastic deformation introduced in horizontal channels and the precipitation misfit strain becomes positive, thus leading to a largest increase in total elastic energy than uniform plastic deformation. For this reason, the horizontal channel deformation mode was omitted in this range.

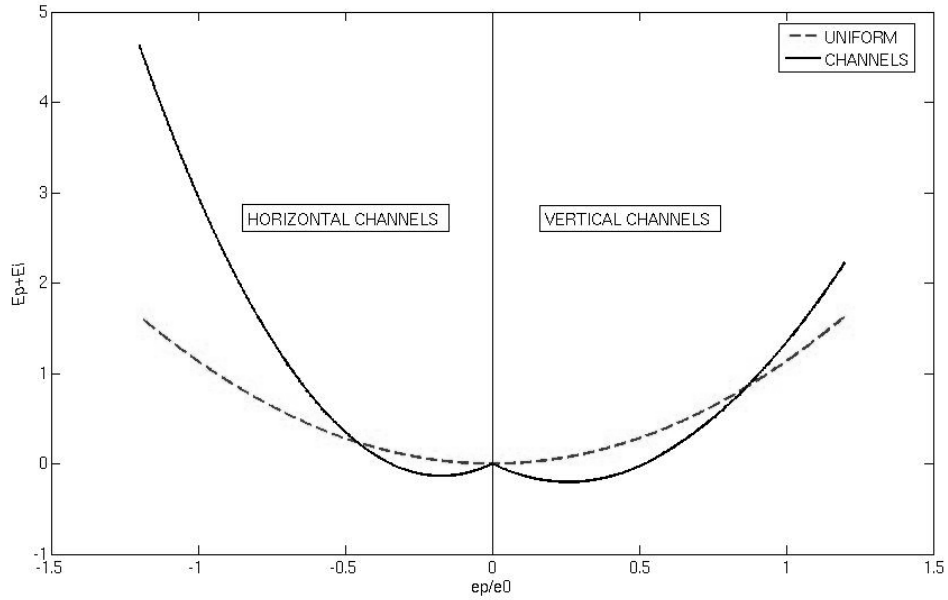

Figure 4.16: Elastic energy increase associated to the introduction of plastic strain in some matrix subdomains as a function of $\overline{\varepsilon_P} / \varepsilon_0$.

In the early stages of a tensile test, the deformation mode showing the lowest elastic energy increase is the confinement of plastic strain in the horizontal matrix channels. This means that plastic strain first initiates in the horizontal matrix channels under the effect of the coherency stress field. Beyond a certain amount of plastic

strain $\overline{\varepsilon_{P1}}$, plastic deformation becomes uniform in the γ matrix. The value of $\overline{\varepsilon_{P1}}$ is calculated by equating the elastic energy increase associated to horizontal channels deformation with that of uniform plastic deformation. The transition from horizontal channels deformation to uniform deformation occurs when

$$\overline{\varepsilon_P} = \overline{\varepsilon_{P1}} = \frac{4fF_3(1-f)C_{11}}{3f(C_{11}+2C_{12})F_3 - 4(1-F_3)(1-f)C_{11}}\varepsilon_0 \approx -\frac{\varepsilon_0}{2} \qquad (4.60)$$

The case of a compressive test is similar to that of a tensile test, but the amount of plastic strain where the transition between channels deformation and uniform deformation occurs, is higher. In other words, at the early stages of a compression test, the plastic deformation initiates in the vertical channels until it becomes uniform beyond the limit $\overline{\varepsilon_{P2}} \approx 0.85\varepsilon_0$. Conversely, when precipitation misfit strain is positive, the role of horizontal and vertical channels plastic deformation is reversed.

IV.5.5 Discussion

It results from the above calculations that the assumption of uniform plastic strain considered in the elasticity analysis of strain induced rafting is justified for all practical purposes. Moreover, this point is justified by the experimental values of the lattice parameter mismatch between γ and γ' phases shown in section III.3. Indeed, at the beginning of the high temperature annealing, the experimental values of the lattice parameter mismatch parallel and perpendicular to the elongation axis, respectively -0.15% and -0.23% in the sample deformed at $\overline{\varepsilon_P} = +0.2\%$, differ from the value of the lattice parameter mismatch in a non deformed sample at the same temperature, which is around -0.12%. The dislocations created during plastic deformation must have therefore propagated into horizontal and vertical channels.

IV.6 Correlation with high temperature creep

In order to specifically discuss the case of creep, the elastic energy is plotted against creep strain for a CMSX-4 alloy, as shown in Fig. 4.17. Here, only the role of plastic strain is considered. In practice, this is done as follows: the case where the matrix plastically deforms by $\boldsymbol{\varepsilon}^{\mathrm{p}}$ is equivalent to the case that the whole specimen plastically deforms by $\boldsymbol{\varepsilon}^{\mathrm{p}}$ and the additional eigenstrain of $\boldsymbol{\varepsilon}^{*} = -\boldsymbol{\varepsilon}^{\mathrm{P}}$ is given to the inclusions. Using (4.12), the equivalent eigenstrain $\boldsymbol{\varepsilon}^{**}$ for this $\boldsymbol{\varepsilon}^{*}$ is calculated. Then the macroscopic creep strain is written as

$$< \boldsymbol{\gamma} >= \boldsymbol{\varepsilon}^{\mathrm{P}} + f\boldsymbol{\varepsilon}^{**}. \qquad (4.61)$$

Since $\boldsymbol{\varepsilon}^{**}$ is a linear combination of $\boldsymbol{\varepsilon}^{*}(= -\boldsymbol{\varepsilon}^{\mathrm{P}})$, the matrix creep strain $\boldsymbol{\varepsilon}^{\mathrm{P}}$ is obtained for a given $\langle \boldsymbol{\gamma} \rangle$. In the calculation f is set to 0.6 to account for partial dissolution of the precipitate phase and elastic constants are taken from [94]. This alloy has the precipitation misfit strain of about -0.18% at the working temperature (1150ºC) [95]. Inserting these values in the calculations, the plot of Figure 4.17 can be obtained. This figure is similar to Figure 4.3, and shows that as creep proceeds, disk shaped particles normal to [001] become increasingly favourable energetically. It has been shown that this alloy shows rafting after primary creep [96].

This model can also rationalise the origin of the high strength of a γ-γ' alloy and the reason for the break-down of retarded creep in the alloy (transition form secondary to tertiary creep). First, it must be noticed that γ' precipitates endure high stress, making Ni superalloys excellent high creep strength materials. This is simply because γ' particles do not contain dislocations. If they do, anti-phase boundaries exist in the particles, increasing the energy. This implies that, when γ' particles are formed by a precipitation process, they avoid pre-existing lattice dislocations. When the stress produced by the matrix plastic deformation becomes large enough, almost equal to the theoretical strength of the γ' phase, the γ' particles can undergo plastic deformation. This is the start of shearing of the γ' particles. The stress state for this process is estimated below.

The data reported by Reed et al [96] show that the plastic deformation of rafted γ' particles occurs when the macroscopic creep strain is about 1.1%. The

corresponding plastic strain in the matrix can be calculated to be approximately 2.0% from eq. (4.61). Using eq. (4.12), the stress due to plastic strain which has occurred in the matrix is calculated to be $\sigma_{11} = \sigma_{22} = -0.46\,GPa$, $\sigma_{33} = 0$. In the calculation, f =0.6, corresponding to the γ' volume fraction at the temperature of the creep test and the crystallographic aspect of slip is ignored. From these, the shear stress of the maximum magnitude of ($\sigma_{33} - \sigma_{11}$)/2 = 0.23 GPa is calculated. This is not so far below the theoretical strength of a perfect crystal, which is about 1/100 of the shear modulus (=95 GPa). Henceforth, we can reasonably speculate that γ' particles start to yield by the accumulation of internal stress due to matrix plastic strain.

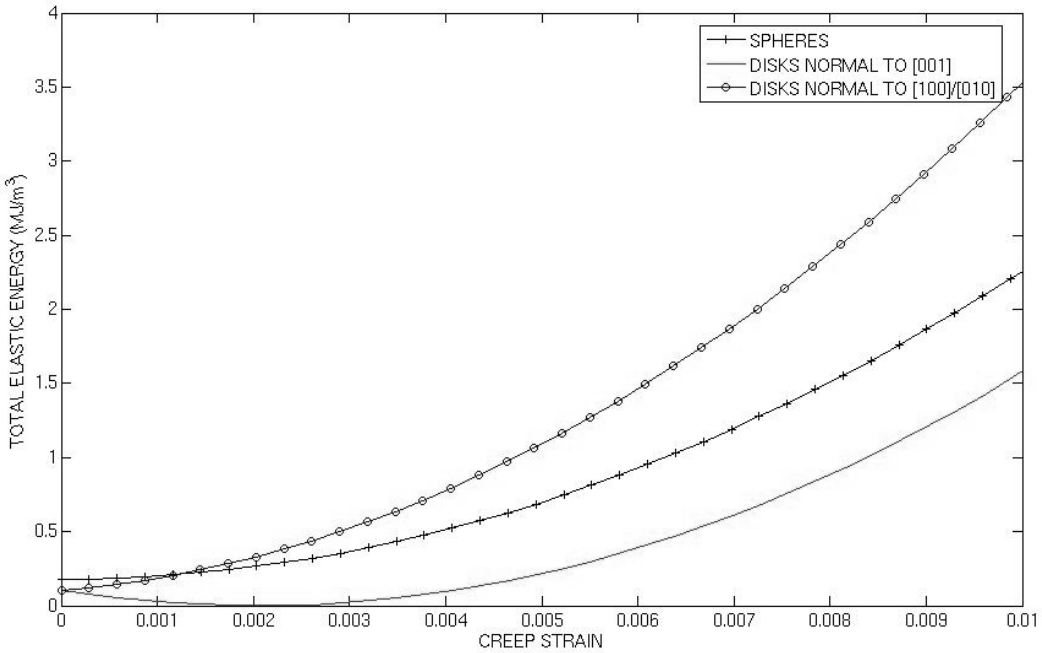

Figure 4.17: Elastic energy as a function of macroscopic creep strain for sphere and disks normal and parallel to [001] for the CMSX-4 commercial alloy.

IV.7 Conclusion

The use of the inclusion theory of anisotropic elasticity combined with a mean field approach has been used to determine the stress free lattice parameter mismatch in nickel superalloys. Moreover, in order to understand rafting that occurs in a predeformed nickel superalloy during a high temperature annealing, the plastic strain has been introduced into the γ matrix and the elastic energy change has been

calculated when the shape of γ' precipitates changes during annealing. The stress state and the associated elastic energy caused by a change in the shape of the γ' precipitates were evaluated. The energetic analysis shows that rafting occurs, depending on the sign and magnitude of both precipitation misfit and plastic strains. The presence of precipitation misfit strain is required to induce the rafting phenomenon. Moreover, it was found that matrix plastic strain discriminates the rafting geometry. The raft shapes and directions, as well as lattice parameters misfit evolution predicted by this analysis agree with the experimental observations reported in Chapter 3 and in the literature. In addition, the use of the inclusion theory combined with the mean field method has allowed the investigation of the deformation modes in presence of a coherency stress field. It is found that the assumption of uniform matrix plastic deformation is justified for all practical purposes. Moreover, the onset of shearing of the γ' particles, inducing an accelerated creep deformation, is shown to be due to the high level of internal stresses.

CHAPTER 5 General discussion

In this section, the main results and analysis shown in previous sections will be discussed. After a discussion of the microstructure aspects, the influence of both plastic strain and temperature on strain induced rafting are considered.

V.1 Microstructure of the MC-NG alloy

V.1.1 Microstructure after homogenisation heat treatment

After the homogenisation heat treatment, the microstructure of MC-NG consists in a regular arrangement of cuboidal γ' particles, whose volume fraction is close to 70% at room temperature. The SANS investigations, coupled with SEM observations, have shown that the shape of the γ' particles looks more cubic in the MC-NG than in the AM1. As discussed in section I.1.3, the cubic shape of the γ' particles results from the dominance of elastic energy over surface energy during precipitation of the γ' phase. At this stage, the elastic anisotropy of both γ and γ' phases make the particles adopt a cubic shape. This result could indicate that the elastic anisotropy is higher in MC-NG than in AM1.

On the other hand, the experimental investigations have shown that the particles size is smaller in MC-NG than in AM1. F. Diologent [6] has shown that, in equivalent heat treatment conditions, the average γ' particles size is around 480nm in the AM1 while it is around 210nm in the MC-NG. A possible contribution that explains this difference lies in the fact that the MC-NG alloy contains heavy refractory elements (Re and Ru). The presence of these heavy elements may slow down the diffusion processes involved in nucleation and particle growth. Indeed, the particles first nucleate under the form of small spherical particles, *i.e.* the particle shape which minimizes the surface energy. When the particles grow, the surface energy increases. However, beyond a critical particle size, the elastic energy prevails over

surface energy and the particles adopt a cuboidal shape, which minimizes elastic energy. The processes of nucleation and particle growth therefore occur under the concurrence of surface energy and elastic energy [32]. The differences in chemical composition between AM1 and MC-NG modify both elastic and surface energy, and therefore the particles size at which the energy balance is reached. A smaller precipitate size can be the result of a smaller elastic energy and/or a bigger surface energy. Moreover, as the particles shape in MC-NG is more cubic than in other alloys such as AM1, we can think that the elastic anisotropy is stronger in MC-NG. This change in interfacial energy could be due to the presence of Re and Ru in the γ matrix. Moreover, the SANS investigations, as well as SEM observations, have shown that the spatial arrangement of the γ' particles in the γ matrix was much less regular in MC-NG than in AM1. The alloy composition seems to play an important role on the microstructure after homogenisation heat treatment in terms of particles shape and spatial arrangement.

V.1.2 Microstructure of the MC-NG after strain induced rafting

SEM observations have shown that the raft microstructure was more irregular in MC-NG than in the AM1 superalloy. This is confirmed by the broad SANS correlation peak reported in section III.1.1. The irregularity in the shape and arrangement of γ/γ' lamellae results from the irregular arrangement of the cuboidal γ' particles before the high temperature annealing during which rafting occurs. Moreover, as rafting involves diffusion processes, we can reasonably speculate that the presence of heavy elements in the γ matrix would retard the morphology change of the particles. Nevertheless, as mentioned in section III.2.1, the kinetics of strain induced rafting are very similar in MC-NG and in AM1, indicating that plastic strain and matrix dislocations and/or vacancies play an important role in the diffusion processes. Indeed, dislocations lying at the γ/γ' interface may provide fast diffusion paths for γ' forming elements towards vertical γ channels. This point is supported by the fact that the γ/γ' lamellar structure is much more regular and the γ' rafts are bigger when the rafting occurs during a high temperature creep test. During such a creep test, the density of matrix dislocations keeps increasing (see Figures 3.37 and .3.38). Moreover, the heavy elements which diffuse slowly may not be involved in the

diffusion processes involved in rafting. Atomic probe spectroscopy performed on a specimen after rafting could confirm this hypothesis, the heavy elements being incorporated in the precipitate phase.

On the other hand, the size of the γ' rafts was found to be much smaller in MC-NG than in AM1 after strain induced rafting in similar experimental conditions. This point can be related to a higher γ/γ' surface energy in MC-NG than in AM1. If we assume an infinite lamellar microstructure, the unconstrained misfit strain can be written as [82]

$$\delta = \frac{1-\nu}{1+\nu}\delta_{//} + \frac{2\nu}{1+\nu}\delta_{\perp} \quad (5.1)$$

Where $\nu \approx 0.43$ is the Poisson's ratio. If we consider the experimental values $\delta_{\min}$ and $\delta_{\max}$ determined in section III.3 (Table 3.2) and the value of the unconstrained misfit determined in section IV.2, the above equation is not satisfied. This result is consistent with the fact that the γ/γ' lamellar structure is not infinite in the case of the MC-NG superalloy. The fact that the γ' rafts are smaller in MC-NG than in AM1 also indicates that the γ/γ' interface energy is higher in the former than in the latter. The alloy composition plays in that respect a preponderant role.

V.2 Mechanisms involved in strain induced rafting

In this section, the mechanisms involved in rafting of γ' particles in single crystal nickel based superalloys are discussed. The development of plastic flow, which discriminates the type of rafting, is discussed in terms of microstructure aspects and alloy composition. The influence of these two parameters on the diffusion mechanisms involved in the particles morphology change, and the associated kinetics, is also examined.

V.2.1 Plastic deformation in the MC-NG alloy

The elasticity analysis conducted in section IV.3 has shown that plastic strain is a determinant parameter to predict the particle morphology change. The development of plastic flow in the superalloys is therefore of particular importance. This discussion is restricted to a rather small amount of plastic strain. We assume here that only the γ matrix plastically deforms. The analysis of the deformation mode described in section IV.5 has shown that the development of plastic flow is uniform when the magnitude of plastic strain exceeds half of the misfit value (in the case of a tensile stress with a negative lattice parameter mismatch). However, this analysis does not account for the microstructure aspects of plastic deformation. As mentioned in section I.2.4, the γ channel width (and therefore the particle size) as well as the presence of an atomic short range order (SRO) in the matrix, strongly influence the development of plastic flow.

First, the Orowan stress, *i.e* the stress required to bow a dislocation line in the matrix channel, is a microstructure dependent parameter (see equation 1.6). The smaller the channel width, the higher the Orowan stress. In the case of the MC-NG superalloy, the relatively smaller particle size results in a reduced γ channel width. When compared to alloys from previous generation such as the AM1, the development of plastic flow is therefore more difficult in this new generation alloy. It must be pointed out that the smaller particle size is directly related to the alloy composition (see section V.1).

Moreover, the presence of an atomic SRO at room temperature in the MC-NG γ matrix induces a heterogeneous development of plastic flow. In such conditions, the dislocation density is high in some matrix channels, inducing a strong stress concentration. This is mainly due to a favoured planar slip mechanism with respect to the cross slip mechanism. In a certain temperature domain (above 850°C), the SRO tends to disappear, and the plastic deformation becomes uniform in the matrix channels through the whole specimen, through the activation of several {111} slip systems, as shown by the TEM observations. Uniform plastic strain is required for strain induced rafting of γ' particles to occur.

As mentioned in section IV.3, the plastic deformation brings anisotropy in the material, which discriminates the type of rafting. However, the presence of precipitation misfit strain is required for rafting to occur. As shown in Figure 4.9, in the absence of precipitation misfit strain, the spherical shape of the γ' particles makes the elastic energy lower, whatever the amount of matrix plastic strain. The investigations conducted in [97] have shown that a threshold creep strain ε_{th} is necessary to induce rafting during a subsequent high temperature annealing without any applied stress. According to their analysis based on the amount of matrix dislocation necessary to relieve the misfit stress field, the value of the threshold strain is related to the stress free misfit value δ and to the γ' volume fraction $f_{\gamma'}$, according to

$$\varepsilon_{th} = 2\delta(1 - f_{\gamma'}^{1/3}) \approx 0.22\delta \qquad (5.2)$$

In this way, the threshold creep strain was found to be underestimated by a factor of two with respect to the experimental results. However, these authors did not consider the role of uniform plastic deformation as they assumed the vertical matrix channels to be dislocation free. When compared to the analysis of deformation modes conducted in section IV.5, such an assumption is valid. The outcome of this analysis is that the threshold creep strain necessary to induce rafting is strongly correlated to the dislocation mobility in the matrix, as it is related to the stress free lattice parameter mismatch and to the γ' volume fraction and therefore the γ channel width. There is in that respect a direct influence of the gliding of dislocations or the generation of vacancies.

V.2.2 Mechanisms involved in the particle morphology change

The experimental results have shown that strain induced rafting is a diffusion controlled process. The role of the high temperature annealing is to activate the diffusion processes involved in rafting. A mechanism for 001 strain induced rafting (type N) would be the interdiffusion of γ' forming elements from the 001 interfaces to the vertical γ channels, with a cross flux of γ-forming elements in the opposite direction. During the first stages of the high temperature annealing, the gradient of the internal strain energy, created by plastic deformation, provides a driving force for

the diffusional mass transport between horizontal and vertical channels. Cuboidal γ' particles coarsen and adopt an elongated shape. The width of the vertical γ channels decreases. After sufficient annealing time, two adjacent particles combine to form a larger particle. Rafting is then complete.

The SANS investigation of the kinetics of strain induced rafting have shown that the alloy composition does not strongly influence the kinetics of the particle morphology change. This point clearly appears when the kinetics of strain induced rafting in AM1 and MC-NG are compared [8]. The matrix dislocations introduced by uniform plastic deformation may provide fast diffusion paths on every particle interfaces. This point is supported by the analysis conducted in section IV.5, which has shown that plastic deformation is uniform in the considered samples. Moreover, Matan et al. [97] support the idea that creep generated matrix dislocations provide fast diffusion paths for rafting to occur at a reasonable speed. However, the resulting microstructure is strongly different in the MC-NG when compared to that of the AM1. As mentioned before, the addition of Re and Ru in the alloy composition may increase the surface energy. In such conditions, the microstructure corresponding to the balance between surface energy and elastic energy corresponds to a smaller precipitate size.

V.2.3 Dislocation mechanisms associated to rafting

The experimental results have shown that the rafting process is accompanied by an anisotropic relaxation of the misfit stresses (see section III.3). According to Véron et al. [9], this anisotropic relaxation occurs via the generated dislocations and is the driving force for rafting, although no dislocation mechanism was proposed. In the conditions of negative lattice parameter mismatch and tensile applied stress, these authors did not consider a uniform plastic deformation but a plastic deformation confined in the horizontal matrix channels, where the dislocations relax the misfit stress field. They assumed the vertical matrix channels to be dislocation free. As mentioned in section I.4, they interpreted rafting as the disappearance of the high energy (dislocation free) interfaces. This point is not supported by the analysis of the

deformation mechanisms presented in the section IV.5, which has shown that there is no reason why some interfaces would be dislocation free when the magnitude of plastic strain exceeds roughly half of the misfit value. In such conditions, the dislocation density in the horizontal matrix channels is larger than that of vertical matrix channels. The conclusions reached by Véron et al. are valid, as long as qualitative aspects are considered.

Even when a particle shape change occurs, dislocations can never be annihilated from the interfaces, except when two neighbouring γ' particles combine to form a larger particle. This applies particularly when the volume fraction of particles is large. In this case, the dislocations on interface A of a particle annihilate those on interface B of another particle, as they have opposite Burgers vectors. This point is schematically shown in Figure 5.1. Moreover, it must be pointed out that the transmission electron microscopy observations of the dislocation structure in a lamellar γ/γ' microstructure did not reveal the presence of any dislocations inside the γ' particles, thus confirming the fact that the dislocations initially present on the vertical interfaces have disappeared during rafting.

On the other hand, the mechanisms involved in strain induced rafting strongly depend on the annealing temperature. The experimental results have shown that strain induced rafting is a continuous process at 1050°C, whereas two distinct processes can be distinguished at 1100°C. At high temperature, the magnitude of the lattice parameter mismatch increases, thus increasing the effect of the coherency stress field. Moreover, the γ' volume fraction decreases, leading to a larger γ channel width. The increase in channel width induces a decrease of the Orowan stress. We can therefore reasonably speculate that dislocations mobility is enhanced in the γ matrix under the effect of an increased misfit and a reduced Orowan stress. The influence of both phenomena is strongly correlated with temperature.

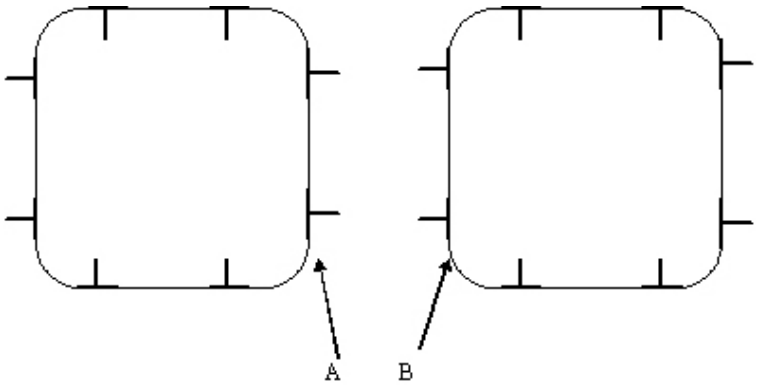

Figure 5.1: Schematic view of dislocations on the interfaces of two particles after straining in tension. When the particles change their shape and combine, leading to rafting, the dislocations on interfaces A and B annihilate each other.

When the annealing temperature is high (above 1100°C), the relaxation of the lattice parameter mismatch is decomposed into two regimes. The first would correspond to the migration of matrix dislocations towards the γ/γ' interfaces, where they relax the coherency stress field perpendicularly to the elongation axis, and enhance it parallel to the elongation axis. During the second regime, the interface dislocations rearrange and combine until they finally adopt the form of a network on the 001 interfaces, similar to that observed after a high temperature creep test. The formation of this network structure reduces the elastic energy. Moreover, the network structure makes the movement of dislocations, involving climb, more difficult. However, the dislocation density in the network is lower after strain induced rafting, than after creep. This is simply because the amount of plastic strain introduced for strain induced rafting is lower than that observed in a sample during the secondary creep stage. A possible reason why only one regime is observed in the lattice parameter mismatch evolution during strain induced rafting at 1050°C could be the reduced mobility of matrix dislocations compared to that at 1100°C. In these conditions, matrix dislocations progressively migrate towards the γ/γ' interface. As there are less interface dislocations in the early stages of the annealing due to a reduced mobility, and as temperature is lower, the diffusion processes associated to the particle morphology change are slowed down.

V.3 The origin for the improved creep properties in the MC-NG alloy

The improved creep properties in MC-NG can be associated to the presence of an incubation period at the beginning of a creep test. Moreover, the primary creep stage, during which rafting of γ' particles occurs can be expected to be longer in MC-NG than in alloys from previous generation such as AM1, because of the presence of heavy refractory elements, which slow down diffusion processes. However, the experimental results described in the present work have shown that there was no major difference in the kinetics of rafting between MC-NG and AM1, as matrix dislocations provide fast diffusion paths. Therefore, a longer rafting kinetics can not explain the improved creep properties of the MC-NG alloy compared to the AM1, although it must be pointed out that the ripening of the rafted microstructure may be slower in the MC-NG than in the AM1, as shorter γ' rafts were observed in MC-NG.

Nevertheless, it was shown that the evolution of γ' volume fraction and lattice parameter mismatch were very different in the two alloys [6]. As discussed above, those two parameters modify the mobility of dislocations in the matrix, as they influence the Orowan stress and the coherency stress field respectively. In the early stages of a creep test, the presence of an incubation period, during which matrix dislocations are created, can be attributed to a harder matrix in MC-NG than in AM1. These dislocations then migrate towards the γ/γ' interfaces where they anisotropically relax the coherency stress field, and promote rafting. A dislocation network is then formed at the horizontal γ/γ' interfaces, which becomes denser as creep proceeds. This is the secondary creep stage. As the dislocation mobility at a given temperature is reduced in MC-NG when compared to the AM1, the kinetics for each dislocation mechanism involved in creep are slowed down. The appearance of the tertiary creep stage is attributed to the shear of the γ' lamellae, when the interfacial stress field induced by the presence of interface dislocations exceed the γ' theoretical shear strength. Using the model described in section IV.5, it can be shown that a hard γ matrix reduce the effective shear stress acting at the interface for a given amount of plastic strain. This point is shown in Figure 5.2, which shows the calculated effective shear stress as a function of the ratio $\mathbf{C}^*/\mathbf{C}$ for a given amount of matrix plastic strain $\varepsilon_P = 2\%$. The elastic constant $\mathbf{C}^*$ of the γ' phase can be considered as equal in AM1

and MC-NG, as there is no major difference in the precipitate phase composition [6]. A harder γ matrix, *i.e* an increased $\mathbf{C}$, corresponds to a decrease in the ratio $\mathbf{C}^*/\mathbf{C}$. As the MC-NG matrix is harder than that of the AM1, the effective shear stress for a given amount of creep strain is smaller in MC-NG than in AM1. This remark can partially explain why, in similar creep conditions, the tertiary creep stage starts at a higher creep strain in MC-NG than in AM1. The hardening of the matrix therefore results in a longer high temperature creep lifetime.

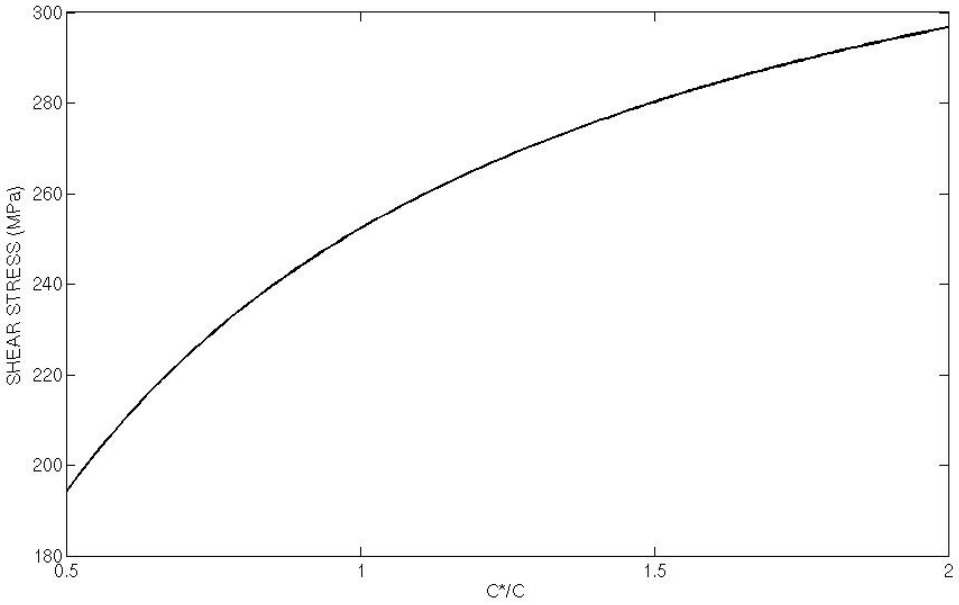

Figure 5.2: Effective shear stress as a function of the ratio $\mathbf{C}^*/\mathbf{C}$. The precipitation misfit strain is $\varepsilon_0 = -0.2\%$ and the volume fraction of the particles is $f = 0.7$

Conclusion

The use of the small angle neutron scattering technique has allowed the investigation of the bulk microstructure of the MC-NG superalloy. It was found that the arrangement of the particles was much less regular than in first generation alloys. Moreover, the direct microstructure observation by scanning electron microscopy has enabled the determination of the particle size distribution. The mean particle size is smaller in MC-NG than in AM1. The heavy addition elements (Re and Ru) were found to modify both elastic and surface energies, what has a consequence on the final γ' precipitates size after rafting, the equilibrium between elastic energy and surface energy being attained at a smaller particle size. Moreover, the *in-situ* investigation of the microstructure evolution during strain induced rafting has shown that the alloy composition does not substantially influence the kinetics of rafting. A possible explanation would be that matrix dislocations and/or vacancies generated during plastic deformation provide fast diffusion paths for the cross diffusion mechanism involved in rafting.

On the other hand, *in-situ* investigations using high resolution diffraction of high energy synchrotron radiation have shown that, during rafting, an anisotropic relaxation of the apparent misfit stresses occurs. In this case, the total misfit stress field results from the combined precipitation misfit strain and matrix plastic strain. Transmission electron microscopy observations have shown that a dislocation network structure forms on the 001 γ/γ' interfaces during rafting. The formation of this network structure reduces elastic energy. The significant parameters that determine the mechanisms involved in rafting are those which influence the dislocation mobility, *i.e.* the γ channel width and the precipitation misfit strain. These parameters are strongly temperature dependent.

The different experimental results obtained during this work have enabled the establishment of a model based on the inclusion theory of anisotropic elasticity combined with a mean field approach. This model describes in a coherent manner the rafting of γ' particles in single crystal nickel based superalloys. It was found that

precipitation misfit strain is required for rafting to occur. However, the anisotropy brought about by matrix plastic deformation was found to discriminate the morphology change of the γ' particles. Besides, the influence of the coherency stress field on the development of plastic flow in matrix channels has been quantified. It is found that the approximation of a uniform matrix plastic deformation is justified for all practical purposes.

In terms of mechanical properties, the hardening of the matrix was found to improve the creep behaviour of a superalloy. The presences of an incubation period at the early stages of a creep test, combined with a reduced effective shear stress, are the consequences of a harder γ matrix. Moreover, the dislocation mobility, which is strongly dependent on temperature and matrix elastic constant, is found to be a determinant parameter to describe the mechanical properties and the mechanisms involved in rafting. Further investigations are required in order to fully characterise the correlation between dislocation mobility, mechanisms involved in rafting and mechanical properties.

Appendix A: Evaluation of the contrast in terms of neutron scattering length density

The alloy content in addition element given in Table 1.1 is expressed in wt%. For convenience, this composition is converted in at%. This is done as follows :

We consider one fcc lattice, which contains 4 atoms. Assuming the lattice parameter to be $a = 3.6$ Å, the molar volume is expressed as

$$V_m = a^3 \cdot \frac{N_A}{4} \quad \text{(A1)}$$

where N_A is the Avogadro constant. The molar density for the alloy is calculated to be

$$d_m = d \cdot V_m \quad \text{(A2)}$$

where d is the density expressed in g.cm^{-3}. This value is also given in Table 1.1. From this, the alloy content in the addition element *i* expressed in at% can be calculated from the values expressed in wt%, as

$$x_i(at\%) = \frac{x_i(wt\%) \cdot d_m}{M_i} \quad \text{(A3)}$$

where M_i is the molar mass of the addition element *i*.

In order to determine the atomic composition of the matrix and precipitate phases consituting the superalloy, the partitioning coefficients $k_i = x_i^{\gamma} / x_i^{\gamma'}$ given in Table 1.2. Considering the following two equations

$$\begin{aligned} k_i &= x_i^{\gamma} / x_i^{\gamma'} \\ x_i &= x_i^{\gamma} + x_i^{\gamma'} \end{aligned} \quad \text{(A4)}$$

Solving the above two equations, the atomic composition in each phase is given by

$$\begin{aligned} x_i^{\gamma} &= \frac{k_i}{1+k_i} x_i \\ x_i^{\gamma'} &= \frac{1}{1+k_i} x_i \end{aligned} \quad \text{(A5)}$$

The scattering length density in each phase is then calculated using equation (2.3)

$$\rho^{\gamma} = n_c \sum_{i=1}^{N} \frac{x_i^{\gamma} b_i}{V_c} \qquad \text{(A6)}$$

$$\rho^{\gamma'} = n_c \sum_{i=1}^{N} \frac{x_i^{\gamma'} b_i}{V_c} \qquad \text{(A7)}$$

where $V_c = a^3$ is the unit cell volume, $n_c = 4$ the number of fundamentals units (atoms or molecules) in the unit cell, b_i .the coherent neutron scattering length of the atom i (tabulated).

Considering the composition of the matrix and precipitate phases given in the MC-NG at 1050°C, this leads to

$\rho^{\gamma'} = 3.293E-5$ Å^{-2} for the precipitates phase

$\rho^{\gamma} = 3.349E-5$ Å^{-2} for the matrix

From these values, the contrast in terms of scattering length densities in a MC-NG sample elevated at a temperature of 1050°C between γ and γ' phases is evaluated to be $\Delta\rho = 5.54E-7$ Å^{-2}.

Appendix B

We consider a needle-like inclusion along [001] defined as

$$\frac{x_1^2 + x_2^2}{a^2} + \frac{x_3^2}{c^2} \le 1\,,\ \frac{c}{a} \to \infty\,. \qquad \text{(B1)}$$

where x_3 is parallel to the [001] crystallographic direction. In this particular case, Mura has shown that the Eshelby tensor is calculated as (see [81] p 141)

$$S_{ijmn} = \frac{1}{2\pi}\int_0^{2\pi} C_{pqmn}\,\frac{\xi_q\xi_i N_{pj}(\xi) + \xi_q\xi_j N_{pi}(\xi)}{2D(\xi)}\,d\phi \qquad \text{(B2)}$$

Here C_{pqmn} is the elastic stiffness of the matrix and

$$\xi_1 = \cos\phi\,,\ \xi_2 = \sin\phi\,,\ \xi_3 = 0\,. \qquad \text{(B3)}$$

N_{kp} and D are respectively the cofactor and the determinant of the matrix defined by

$$K_{ik} = C_{ijkl}\xi_j\xi_l \qquad \text{(B4)}$$

In this special case, (B2) is integrated with an elementary method. We thus obtain

$$S_{1111} = S_{2222} = \frac{1}{2}\left(J + \frac{2(1-J)(C_{11} - C_{12} - C_{44})}{(C_{11} - C_{12} - 2C_{44})}\right) \qquad \text{(B5)}$$

$$S_{1122} = S_{2211} = \frac{JC_{12}}{2C_{11}} - \frac{(1-J)C_{44}}{C_{11} - C_{12} - 2C_{44}} \qquad \text{(B6)}$$

$$S_{1133} = S_{2233} = \frac{C_{12}}{C_{11} + C_{12}}\left(1 - \frac{J(C_{11} - C_{12})}{2C_{11}}\right) \qquad \text{(B7)}$$

$$S_{1212} = \frac{1}{2}\left(J - \frac{2(1-J)C_{44}}{C_{11} - C_{12} - 2C_{44}}\right) \qquad \text{(B8)}$$

$$S_{1313} = S_{2323} = \frac{J}{4} \qquad \text{(B9)}$$

where $C_{11} = C_{1111}$, $C_{12} = C_{1122}$, $C_{44} = C_{2323}$. Other $S_{ijkl} = 0.$

$$J = \left\{ 1 + \frac{(C_{11} - C_{12} - 2C_{44})(C_{11} + C_{12})}{4C_{11}C_{44}} \right\}^{-1/2}. \quad \text{(B10)}$$

The numerical values for pure Ni are

$S_{1111} = S_{2222} = 0.6287$, $S_{1122} = S_{2211} = 0.1024$, $S_{1133} = S_{2233} = 0.2795.$

References

[1] A. Fredholm, « Monocristaux d'alliage base nickel, relation entre composition, microstructure et comportement en fluage à haute température », thèse de l'Ecole Nationale des Mines de Paris (1987)

[2] S.M. Copley, B.H. Kear, Trans. Met. Soc., AIME 239, p. 984 (1967)

[3] M. Durand-Charre, « The microstructure of superalloys », ISBN 90-5699-097-7, Gordon and Breach Science Publishers (1997)

[4] T. Murakamo, T. Kobayashi, Y. Koizumi, H. Harada, Acta Materialia 52 p.3737-3744 (2004)

[5] P. Caron, Proceedings of Superalloys 2000, The Minerals, Metals & Materials Society, p.737-746 (2000)

[6] F. Diologent, "Comportement en fluage et en traction de superalliages monocristallins à base de nickel", thèse de l'Université Paris XI Orsay (2002)

[7] M. Véron, Y. Bréchet, F. Louchet, Scripta Metallurgica, Vol. 34, p.1883 (1996).

[8] M. Véron and P. Bastie, Acta. Materialia., Vol. 45, No 8, p. 3277-3282 (1997).

[9] M. Véron, F. Louchet, , Acta Materialia, Vol.44, No.9, p. 3633-2641 (1996)

[10] T. Strangman, G. Hoppin, C. Phipps, K. Harris, R. Schwer, Proceedings of Superalloys 1980, TMS, Warendale, PA, USA, p. 215-224 (1980)

[11] L. S. Lin, A. Giamei, R. Doiron, 38th EMSA Meeting, p. 330-331 (1980)

[12] M. Pessah-Simonetti, « Effets des instabilités structurales sur les propriétés mécaniques du superalliage monocristallin MC2 », thèse de doctorat, Université d'Orsay, Paris XI (1994)

[13] M. Pessah, P. Caron, T. Khan, Proceedings of Superalloys 1992, TMS, Warendale, PA, USA, p. 567-576 (1992)

[14] C. Rae, R. C. Reed, Acta Materialia, 49, p. 4113-4125 (2001)

[15] F. Pettinari, "Mécanismes élémentaires de la déformation de phases γ d'une nouvelle génération de superalliages base nickel. Rôle du Rhénium et du Ruthénium », thèse de doctorat Université Paul Sabatier de Toulouse (1999)

[16] A. Buchon, « Composition des phases, microstructure et distribution spatiale très fine à l'échelle des solutés dans quelques superalliages à base de nickel », thèse de doctorat, Université de Rouen (1991)

[17] S. Duval, S. Chambreland, P. Caron, D. Blavette, Acta Metallurgica et Materialia, 42, p. 185-194 (1994)

[18] D. Blavette, P. Caron, T. Khan, Proceedings of Superalloys 1988, TMS, Warendale, PA, USA, p. 305-314 (1988)

[19] N. Wanderka, U. Glatzel, Materials Science and Engineering, A203, p. 69-74 (1995)

[20] P. Warren, A. Cerezo, G. Smith, Materials Science and Engineering, A250, p. 88-92 (1998)

[21] P. Caron, T. Ohta, Y. G. Nagakawa, T. Khan, Superalloys 1988, (ed.) Duhl et al., Met. Soc. AIME, Warrendale (USA), 215-224 (1988)

[22] T. Khan, P. Caron, Materials Science and Technology, 2, p. 486-492 (1986)

[23] E Hornboegen, H Warlimont, Metallkunde, “Aufbau und Eigenschaften von Metallen und Liegerungen” (Berlin: Springer), p.134-144 (1991)

[24] J. W. Cahn, Acta Metallurgica, 7, p.18 (1959)

[25] G. Bruno, H. C. Pinto, Materials Science and Technology, 19, p.1-6 (2003)

[26] I.M. Lifshitz, V. V. Slyozov, Journal of Physics and Chemistry of Solids, 19, p.35-50 (1961)

[27] C. Wagner, Z. Elektrochem., 65, p. 581-591 (1961)

[28] A. G. Kachaturyan, “Theory of structural transformation in solids”, New York, Wiley (1983)

[29] A. G. Kachaturyan, S. V. Semenovskaya, J. W. Morris Jr, Acta Metallurgica, 36, p. 1563-1571 (1988)

[30] J. Colin, J. Grilhé, N. Junqua, Acta Materialia, 46, p. 1249-1255 (1998)

[31] Y. Yamabe-Mitarai, H. Harada, Philosophical Magazine Letters, 82, p. 109-118 (2002)

[32] N. Ratel, G. Bruno, B. Demé, Journal of Physics: Condensed Matter, 17, p. 7061-7075 (2005)

[33] G. Bruno, H. C. Pinto, W. Reimers, Journal of Applied Physics, A74, p. 940-942 (2002)

[34] C.H.Su, P.W. Voorhees, Acta Materialia, Vol. 44, No. 5, 2001-2016 (1996)

[35] T. Grosdidier, « Etude de la transformation de phase γ->γ’ de superalliages monocristallins à base de nickel. Influence de sollicitations mécaniques et

d'hétérogénéités chimiques », thèse de doctorat, Institut National polytechnique de Lorraine (1992)

[36] A. Royer, P. Bastie, M. Véron, Acta Materialia, 46 p.5357-5358 (1998)

[37] B. Décamps, M. Condat, P. Caron, T. Khan, Scripta Metallurgica, 18, p.1171-1174 (1984)

[38] W. Milligan, S. Antolovich, Metallurgical Transactions, 18A, p. 85-95 (1987)

[39] G. Scheunemann-Ferker, H. Gabrish, M. Feller-Kniepmeier, Philosophical Magazine A, 65, p.1353-1368 (1992)

[40] L. Kubin, B. Lisiecki, P. Caron, Philosophical Magazine A, 71, p.991-1009 (1995)

[41] C. Yuan, J. Guo, H. Yang, S. Wang, Scripta Materialia, 39, p. 991-997 (1998)

[42] B. Kear, G. Leverant, J. Oblak, Metallurgical Transactions, 62, p. 639-650 (1969)

[43] G. Leverant, B. Kear, Metallurgical Transactions, 1, p. 491-498 (1970)

[44] B. Kear, J. Oblak, A. Giamei, Metallurgical Transactions, 1, p. 2477-2486 (1970)

[45] B. Décamps, A. Morton, M. Condat, Philosophical Magazine A, 64, p. 641-648 (1991)

[46] M. Condat, B. Décamps, Scripta Materialia, 21, p. 607-612 (1987)

[47] B. Décamps, S. Raujol, A. Coujou, F. Pettinari-Sturmel, N. Clément, D. Locq, P. Caron, Philosophical Magazine, 84, p. 91-107 (2004)

[48] P. Veyssiere, G. Saada, « Dislocations in solids », 10, p.316 Elsevier Sciences (1996)

[49] B. Kear, H. Wilsdorf, Transactions of Metallurgical Society AIME, 224, p. 2397-2407 (1962)

[50] F. Pettinari, M. Jouiad, P. Caron, H. Calderon, A. Coujou, N. Clément, La revue de Métallurgie-CIT / Science et Génie des Matériaux, p. 1037-1045 (2000)

[51] R. Glas, M. Jouiad, P. Caron, N. Clément, H. O. K. Kirchner, Acta Materialia, 44 (12), p. 4917-4926 (1996)

[52] M. Jouiad, F. Pettinari, N. Clément, A. Coujou, Philosophical Magazine A, 79, p. 2591-2602 (1999)

[53] M. Benyoucef, B. Décamps, A. Coujou, N. Clément, Philosophical Magazine A, 71, p. 907-923 (1995)

[54] F. Pettinari-Sturmel, J. Douin, G. Saada, P. Caron, A. Coujou, N. Clément, Materials Science and Engineering, A325, p. 511-519 (2002)

[55] M. S. A. Karutaratne, R.C. Reed, Acta Materialia, Vol. 51, No. 10, 2905-2919 (2003)

[56] R. Schnek, Philosophical Magazine A, 81, p. 383-398 (2001)

[57] U. Glatzel, M. Feller-Kniepmeier, Scripta Metallurgica, 23, p. 1839-1844 (1989)

[58] J. Ganghoffer, A. Hazotte, S. Denis, A. Simon, Scripta Metallurgica, 25, p. 2491-2496 (2001)

[59] L.Müller, U. Glatzel, M. Feller-Kniepmeier, Acta Metallurgica et Materialia, 40, p. 1321-1327 (1992)

[60] T. M. Pollock, A. Argon, Acta Metallurgica et Materialia, 42, p. 1859-1874 (1994)

[61] T. M. Pollock, A. Argon, Acta Metallurgica et Materialia, Vol. 40, No.1, p. 1-30 (1992)

[62] J. X. Zhang, J.C. Wang, H. Harada, Y. Koizumi, Acta Materialia, 53, p. 4623-4633 (2005)

[63] H. Murakami, T. Yamagata, H. Harada, M. Yamakazi, Materials Science and Engineering, A223, p. 54-58 (1997)

[64] J. K. Tien, S. M. Copley, Metallurgical transactions, 2A, p. 543-553 (1971)

[65] J. C. Chang, S. M. Allen, Journal of Material Research, 6, p. 1843-1855 (1991)

[66] S. Socrate, D. M. Parks, Acta Metallurgica et Materialia, Vol. 41, No 7, p. 2185-2209 (1993)

[67] F. Louchet, M. Véron, Y. Bréchet, A. Hazotte, J-Y. Buffière, P. Bastie, A. Royer, La Revue de Métallurgie-CIT / Science et Génie des Matériaux, p. 1481-1490 (1998)

[68] W. Chen, J-P. Immarigeon, Scripta Materialia, 39, p. 167-174 (1998)

[69] R. McKay, L. Ebert, Scripta Metallurgica, 17, p. 1217-1222 (1983)

[70] A. Epishin, T. Link, U. Brückner, P. D. Portella, Acta Materialia, 49, p. 4017-4023 (2001)

[71] P. Caron, Actes de conférence, Colloque Plasticité 2006 (2006)

[72] J-Y. Buffière, M. Ignat, Acta Metallurgica et Materialia, Vol. 43, No. 5, p. 1791-1797 (1995)

[73] A. Guinier, G. Fournet, “Small Angle scattering of X-rays”, New York, Wiley (1955)

[74] J. P. Cotton, F. Nallet, “Diffusion de neutrons aux petits angles”, Journal de Physique IV Proceedings, ISSN 1155-4339 (1998)

[75] http://www.nist.ncr.gov/resources/simulator.html

[76] R. E. Gosh, « A computing guide for small angle neutron scattering experiments », ILL (1981)

[77] http://www.ill.fr/YellowBook/D11/

[78] U. Keiderling, Appl. Phys. A74 [Suppl.], S1455-S1457 (2002)

[79] K. D. Liss, A. Royer, T. Tschentscher, P. Suortti, A. Williams, Journal of Synchrotron Radiation, 5, pp.82 (1998)

[80] A. Müller, T. Gnäupel-Herol, W. Reimers: Phys. stat. sol. (a), Vol. 156 p.375, (1996)

[81] L. Müller, T. Link, M. Feller-Kniepmeier: Scripta met. mat., Vol. 26 , p.1297 (1992)

[82] A. Jacques, P. Bastie, Philosophical Magazine, Vol. 83, No.26, pp. 3005-3027 (2003)

[83] D. Bellet, P. Bastie, J. Lajzerowicz, J.F. Legrand, R. Bonnet, Journal de Physique I, 2, p.205-220 (1992)

[84] D. Bellet, ‘Etude des textures des superalliages monocristallins par diffraction et diffusion des rayonnements : X, γ et neutrons’, Thèse de doctorat, Université Joseph Fourier (1990)

[85] J.D. Eshelby, Proceedings of Royal Society, 241A, p.376-396 (1957)

[86] T. Mura, “Micromechanics of defects in solids”, Martinus Nijhoff (1987)

[87] T. Mori, K. Tanaka, Acta Metallurgica, 21, p.571-575 (1973)

[88] K. Wakashima, H. Tsukamoto, Materials Science and Engineering, A146, p. 291-319 (1991)

[89] W. C. Johnson, M. B. Berkenpas, D. E. Laughlin, Acta Metallurgica, 36, p. 3149-3162 (1988)

[90] A. Pineau, Acta Metallurgica, 24, p. 559-564 (1976)

[91] D.Y. Li, L. Q. Chen, Scripta Materialia, 37, p. 1271-1277 (1997)

[92] F. R. N. Nabarro, C. M. Cress, P. Kotschy, Acta Materialia, 44, p. 3189-3198 (1996)
[93] S. Socrates, D. M. Parks, Acta Metallurgica et Materialia, 41, p. 2185-2209 (1993)

[94] D. Sieborger, H. Knabe, U. Glatzel, Materials Science and Engineering, A298, p26-33 (2001)

[95] G. Bruno, B. Schönfeld, G. Kostorz, Zeitschrift fur Metallkunde., Vol. 94 No. 1, p.12-18 (2003).

[96] R.C.Reed, N. Matan, D.C. Cox, M.A.Rist, C.M.F Rae, Acta Materialia, Vol. 47**,** p.3367-3381 (1999)

[97] N. Matan, D.C. Cox, C.M.F. Rae, R.C. Reed, Acta Materialia, Vol. 47, No.7, p. 2031-2045 (1999)

Résumé :

Les superalliages à base de nickel sont utilisés dans l'industrie aéronautique pour leur bonne tenue mécanique à haute température (1100°C). Les particules durcissantes de phase γ' présentent une évolution morphologique de cuboïdes a radeaux au cours d'un test de fluage. Nous présentons ici les résultats d'investigation par diffusion de neutrons aux petits angles, diffraction à haute résolution de rayonnement synchrotron et microscopie électronique. Ils permettent d'établir le lien entre le développement de la plasticité et l'évolution microstructurale des superalliages. Les précipités γ' initialement inclus dans la matrice γ sous forme d'un arrangement périodique de particules de forme cuboïdale adoptent alors la forme d'une structure lamellaire γ/γ'. L'utilisation de la diffusion de neutrons aux petits angles au cours d'un recuit *in situ* permet de caractériser la cinétique de mise en radeaux des précipités γ'. Par ailleurs, l'analyse *in situ* de l'évolution des contraintes internes au cours de la transformation microstructurale permet de caractériser les micromécanismes mis en jeu. Des observations en microscopie électronique en transmission des structures de dislocations avant et après la mise en radeaux confirment ces résultats. De plus, un modèle basé sur la théorie des inclusions en élasticité anisotrope est présenté, permettant de corréler l'ensemble des résultats expérimentaux au comportement en fluage de ces matériaux. Il a été trouvé que la cinétique de mise en radeaux des précipités γ' est indépendante de la composition de l'alliage, les dislocations et/ou les lacunes introduites lors de la déformation plastique servant de court-circuit de diffusion.

Mots clés : Superalliages, Diffusion de neutrons aux petits angles, Diffraction, Microscopie électronique, désaccord paramétrique, théorie des inclusions

Abstract:

Single crystal nickel based superalloys find their application in aerospace engineering since they exhibit a very good mechanical behaviour at high temperature (1100°C). These peculiar properties are strongly correlated with a morphology change from cuboids to rafts of the hardening γ' precipitate phase. This microstructure evolution, also called rafting was first revealed during a creep test. In this work, we show the results of small angle neutron scattering, high resolution diffraction of synchrotron X-radiation and electron microscopy investigations. This allows the establishment of a correlation between the development of plastic flow and microstructure evolution of these superalloys. The use of small angle neutron scattering during an *in-situ* high temperature annealing of a deformed sample allows the characterisation of the kinetics of strain induced rafting of the γ' particles. Moreover, the *in-situ* analysis of the evolution of internal stresses during rafting has enabled the identification of the micromechanisms involved. Electron microscopy observations of the resulting microstructure and dislocation structure confirm these results. In addition, a model based on the inclusion theory of anisotropic elasticity combined with a mean field approach is developed. A correlation between the experimental results and creep behaviour is thus obtained. Results show that the kinetics of rafting of the γ' particles does not depend on the alloy composition, and that a pipe diffusion mechanism is involved.

Keywords : superalloys, small angle neutron scattering, Diffraction, Electron microscopy, lattice mismatch, Inclusion theory